Behavior of Three Metallic Alloys Under Combined Axial-Shear Stress at 650 °C

Jason F. Colaiuta
Pennsylvania State University, University Park, Pennsylvania

October 2001

Since its founding, NASA has been dedicated to the advancement of aeronautics and space science. The NASA Scientific and Technical Information (STI) Program Office plays a key part in helping NASA maintain this important role.

The NASA STI Program Office is operated by Langley Research Center, the Lead Center for NASA's scientific and technical information. The NASA STI Program Office provides access to the NASA STI Database, the largest collection of aeronautical and space science STI in the world. The Program Office is also NASA's institutional mechanism for disseminating the results of its research and development activities. These results are published by NASA in the NASA STI Report Series, which includes the following report types:

- TECHNICAL PUBLICATION. Reports of completed research or a major significant phase of research that present the results of NASA programs and include extensive data or theoretical analysis. Includes compilations of significant scientific and technical data and information deemed to be of continuing reference value. NASA's counterpart of peer-reviewed formal professional papers but has less stringent limitations on manuscript length and extent of graphic presentations.

- TECHNICAL MEMORANDUM. Scientific and technical findings that are preliminary or of specialized interest, e.g., quick release reports, working papers, and bibliographies that contain minimal annotation. Does not contain extensive analysis.

- CONTRACTOR REPORT. Scientific and technical findings by NASA-sponsored contractors and grantees.

- CONFERENCE PUBLICATION. Collected papers from scientific and technical conferences, symposia, seminars, or other meetings sponsored or cosponsored by NASA.

- SPECIAL PUBLICATION. Scientific, technical, or historical information from NASA programs, projects, and missions, often concerned with subjects having substantial public interest.

- TECHNICAL TRANSLATION. English-language translations of foreign scientific and technical material pertinent to NASA's mission.

Specialized services that complement the STI Program Office's diverse offerings include creating custom thesauri, building customized data bases, organizing and publishing research results . . . even providing videos.

For more information about the NASA STI Program Office, see the following:

- Access the NASA STI Program Home Page at *http://www.sti.nasa.gov*

- E-mail your question via the Internet to help@sti.nasa.gov

- Fax your question to the NASA Access Help Desk at 301–621–0134

- Telephone the NASA Access Help Desk at 301–621–0390

- Write to:
  NASA Access Help Desk
  NASA Center for AeroSpace Information
  7121 Standard Drive
  Hanover, MD 21076

Behavior of Three Metallic Alloys Under Combined Axial-Shear Stress at 650 °C

Jason F. Colaiuta
Pennsylvania State University, University Park, Pennsylvania

National Aeronautics and
Space Administration

Glenn Research Center

October 2001

Acknowledgments

First and foremost, I want to thank my thesis advisor, Dr. Cliff Lissenden for all of his assistance and guidance throughout the course of this project. Also, I want to thank Dr. Bradley Lerch of NASA Glenn Research Center for his guidance throughout the experimental portion of this project. I also want to express my gratitude for the financial support of the NASA Glenn Research Center provided under Cooperative Agreement NCC3–597. Furthermore, I must acknowledge everyone that I worked with at NASA GRC for the technical support they provided. In addition, I would like to thank the members of my thesis reading committee, Dr. Charles Bakis and Dr. Francesco Costanzo for reviewing my thesis.

Table of Contents

List of Tables

List of Figures

Chapter 1

Introduction

1.1 General Introduction and Objectives

Structural components used in aero-propulsion applications are often subjected to complex multiaxial stress states while at high temperatures. Under such demanding conditions materials can incur permanent deformations and changes in material state. When faced with such a difficult situation the engine designer would be greatly aided by a viscoplastic multiaxial deformation model that could accurately describe the material response over a wide range of conditions. Viscoplastic models such as the GVIPS developed by Arnold et al.[15] or Bodner-Partom [18] models can perform this task. Unfortunately, these models have yet to be validated under complex service conditions. This is due to the fact that experiments used for validation must subject the material to multiaxial stress states as well as elevated temperature. In short, the testing is very complex, expensive, and time consuming.

The work presented here is an extensive study of the evolution of yield surfaces after axial-torsional prestraining. It consisted of two phases, the experimental research conducted at NASA Glenn Research Center (NASA-GRC), and data analysis conducted at Penn State University. The goals of the study were: (1) build a library of yield surface data for Inconel 718, Haynes 188, and 316 stainless steel, (2) mathematically fit the yield

surface data with a model incorporating yield surface distortion effects, and (3) use the

model parameters to construct evolution equations describing the yield surfaces.

1.2 Plasticity Theory

Classical plasticity is a mathematical theory that describes permanent time-independent deformation of materials, such as metals at room temperature. Such mathematical theories are phenomenological in nature and are based on experimental observations. Classical plasticity theories have three distinct parts, a yield criterion, a plastic flow rule, and a hardening rule. The current section will discuss these three topics as well as loading criteria and will then introduce viscoplasticity.

1.2.1 Yield Functions

Yield functions are used to separate elastic stress states from those where plastic deformation occurs. For an isotropic metal under isothermal conditions the general form of the yield function can be written as,

$$f = F(\sigma_{ij}) - k = 0 \qquad\qquad (1.1)$$

where $F(\sigma_{ij})$ is a function of the current stress state and k is a constant based on the initial tensile yield strength of the material. Yielding initiates when $f=0$ and the surface defined by this condition is know as the yield surface. All stress states inside of the yield surface are elastic and stress states outside of the yield surface are not permitted unless a viscoplastic model is being used. As a result, the yield surface must evolve as plastic deformation occurs in order to insure that the stress state remains on the yield surface.

The two most popular yielding criteria are associated with Tresca [1] and von Mises [2] criteria. Both of these theories are for isotropic materials and are deviatoric in nature.

The Tresca, or maximum shear stress criterion is based on the assumption that a material will yield if the maximum shear stress exceeds the critical shear strength, τ_Y. The critical shear strength is defined as $\tau_Y = \sigma_Y/2$ where σ_Y is the tensile yield strength. In terms of the principal stresses the Tresca yield condition takes on the following form,

$$f = \max\left(|\sigma_I - \sigma_{II}|, |\sigma_{II} - \sigma_{III}|, |\sigma_{III} - \sigma_I|\right) - \sigma_y \qquad (1.2)$$

where σ_I, σ_{II}, σ_{III} represent the principal normal stresses and σ_y the tensile yield strength. Equation 1.2 assumes a fully three-dimensional stress state, however the work in this study involves only stress states in the axial-shear stress plane. Consequently, there are only two non-zero stress terms: axial stress, σ_{11}, and shear stress, σ_{12}. Therefore, the Tresca yield function reduces to,

$$\sigma_{11}^2 + 4\sigma_{12}^2 = \sigma_Y^2 \qquad (1.3)$$

The Tresca yield criterion is very easy to apply, however it often provides a conservative estimate of the yield stress.

The von Mises yield criterion often agrees better with experimental results than the Tresca criterion. This criterion is also known as the distortion energy criterion because it predicts yielding to occur when the maximum distortion energy exceeds the energy required to cause yielding under pure tension. The von Mises theory can be expressed as,

$$f = \sqrt{3J_2} - \sigma_Y = 0 \qquad (1.4)$$

where J_2 is the second invariant of deviatoric stress given by,

$$J_2 = \frac{1}{2} s_{ij} s_{ij} \qquad \text{(1.5)}$$

and deviatoic stress, s_{ij}, is defined as,

$$s_{ij} = \sigma_{ij} - \frac{1}{3} \sigma_{kk} \delta_{ij} \qquad \text{(1.6)}$$

where δ_{ij} is a second order identity tensor. When expressed in the axial-shear stress plane the von Mises yield criterion becomes

$$\sigma_{11}^2 + 3\sigma_{12}^2 = \sigma_Y^2. \qquad \text{(1.7)}$$

Figure 1.1 shows the relative size of yield surfaces predicted by the Tresca and von Mises yield criteria. Also note from Esq. 1.7 that if the shear stresses are multiplied by $\sqrt{3}$ the von Mises ellipse becomes a circle. This characteristic will be used extensively in later analysis.

1.2.2 Loading Criteria

In order to discuss plastic flow it is first necessary to present a formal definition of loading. There are three different types of loading that can occur in a work hardening material when the stress state is located on the current yield surface. If an infinitesimal stress increment is added to the stress state directed outside of the yield surface then the loading condition becomes,

$$f = 0 \ \text{ and } \ \frac{\partial f}{\partial \sigma_{ij}} d\sigma_{ij} > 0. \qquad \text{(1.8)}$$

However, a stress state located outside of the yield surface is not permitted therefore the yield surface must evolve to accommodate the new stress state.

The second loading condition is one where the stress increment is directed such that it moves the current stress state inside of the yield surface. This is called unloading and is given by,

$$f = 0 \ \text{and} \ \frac{\partial f}{\partial \sigma_{ij}} d\sigma_{ij} < 0. \tag{1.9}$$

The final loading type is called neutral loading, which occurs when the infinitesimal stress increment is directed tangent to the yield surface. This type of loading causes no evolution of the yield surface and can be represented by

$$f = 0 \ \text{and} \ \frac{\partial f}{\partial \sigma_{ij}} d\sigma_{ij} = 0. \tag{1.10}$$

1.2.3 Flow Laws

As already stated, when a material reaches a stress state where $f=0$ it ceases to behave in a linear elastic manner and incurs permanent deformations. Because of this permanent deformation the material is said to undergo plastic flow. This plastic flow changes the material state, which drives the evolution of the yield surface. Since plastic strain is path-dependent, it must be computed in an incremental form, $d\varepsilon_{ij}$.

It is often convenient to define the flow law in terms of a plastic potential function such as the one presented by von Mises [3],

$$d\varepsilon_{ij}^{p} = d\lambda \frac{\partial \Omega}{\partial \sigma_{ij}} \tag{1.11}$$

where Ω is a plastic potential function that is a scalar function of stress, $d\lambda$ is a nonnegative scalar that is zero unless the stress state is on the yield surface and the loading criteria is satisfied. It can be shown that $\frac{\partial \Omega}{\partial \sigma_{ij}}$ is normal to the plastic potential

function, Ω, therefore the plastic strain increment is always normal to the plastic potential function. Consequently, Equation 1.11 is known as the normality flow rule.

If the potential function in Equation 1.11 is a yield function then the flow law becomes an associated flow law. If the von Mises yield criterion is used (Equation 1.4) then Equation 1.11 is known as the Prandtl-Reuss flow law (Prandtl [4] and Reuss [5]), given by,

$$d\varepsilon_{ij}^{p} = d\lambda s_{ij}. \qquad (1.12)$$

1.2.4 Hardening Laws

Hardening occurs when the conditions in Equation (1.8) are met. Since the stress increment tries to push the stress state to fall outside of the yield surface the surface must evolve. This evolution is called hardening. There are three types of hardening that are relevant to this study. They are isotropic, kinematic, and distortional hardening. Isotropic hardening occurs when the yield surface increases in size without a change in shape or translation of the center point. This type of hardening implies an overall increase in the yield strength of the material. In contrast, kinematic hardening is a change in the location of the center of the yield surface without a change in size or shape. The Bauschinger effect results from kinematic hardening. Figure 1.2 shows changes in the yield surface due to isotropic and kinematic hardening effects. Distortional hardening is more difficult to represent mathematically than the other two types. It is a change in the overall shape of the yield surface. This often involves a change in the curvature of the yield surface, usually an increase in the front and a decrease in the back. An example of curvature change after an axial prestrain is shown in Figure 1.3. Another distortional

effect is known as a cross effect which is a change in the size of the yield surface normal to the direction of prestraining. Positive cross effects are shown in Figure 1.4.

A general yield function, such as the one in Equation 1.1 can be easily altered to incorporate isotropic hardening effects. This is accomplished by making k a function of a state variable q that accounts for the material loading history. As the total plastic strain imparted on the material increases, $k(q)$ increases, resulting in an overall increase of the material yield strength in all loading directions.

The yield function in Equation 1.1 can also be altered to represent kinematic hardening as follows,

$$f = F\left(\sigma_{ij} - \alpha_{ij}\right) - k \tag{1.13}$$

where α_{ij} is known as the back stress tensor. The back stress describes the translation of the yield surface with respect to the plastic deformation history of the material. Note that k is a constant.

It follows that these two hardening types can easily be incorporated into a single model to describe both isotropic and kinematic hardening as shown,

$$f = F(\sigma_{ij} - \alpha_{ij}) - k(q) \tag{1.14}$$

This mixed hardening model often better predicts yield surface evolution than either of the previous two, however, it still does not account for any change in the shape of the yield surface.

1.2.5 Distortional Hardening

Being a change in shape, distortional hardening is not easily described mathematically. The change in shape is greatly influenced by the direction of loading. In

order to discuss distortional hardening, a preloading direction must first be defined. The direction of the plastic loading is known as the preloading direction and dictates the nature of the distortional effects seen in the subsequent yield surface. Figure 1.3 shows yield surfaces with a tensile preloading direction.

An important point is that the prestrain and prestress directions are not always coincident. This is particularly true for nonproportional loadings. For example, let a specimen be loaded in tension into the plastic regime under strain control. If loading is then continued, under strain control, in the shear direction the stress will not follow the same path as the strain. Once shear straining is initiated the axial stress will begin to reduce due to plastic coupling effects. However, the axial strain does not change when shear strain is applied. This is illustrated in Figure 1.5, where figure (a) shows the strain path followed while figure (b) shows the response of the stress. The arrows show the direction of the change in stress at the given point.

There have been many approaches used to describe distortional hardening effects. One approach, by Ortiz and Popov [6], uses trigonometric functions. The yield function that they used is,

$$f = \left\| s_{ij} \right\| - \sigma_Y \left(1 + \rho_2 \cos 2\theta_2 + \rho_3 \cos 3\theta_3\right) \tag{1.15}$$

where $\|s_{ij}\|$ is the norm of the effective deviatoric stress defined as $\Sigma_{ij} = (s_{ij} - \alpha_{ij})$, σ_Y is the initial tensile yield strength, ρ_2 and ρ_3 are model parameters that describe cross effects and changes in curvature respectively, and θ_2 and θ_3 give the angle between the effective deviatoric stress tensor and the phenomenological internal variables β_2 and β_3. These internal variables are unit tensors that define the direction of the yield surface

characteristic being modeled by that term. For example, since the term with subscripts 3 represent distortion, β_3 would represent the direction in which the distortion occurs. This model has the ability to represent isotropic, kinematic, and distortional hardening, however the model parameters have little physical meaning.

Another model developed by Eisenberg and Yen [7] uses a second order tensor to describe distortion effects. The yield function for this model is,

$$f = \frac{1}{2}\left(s_{ij} - \alpha_{ij} + R_{ij}\right)\left(s_{ij} - \alpha_{ij} + R_{ij}\right) - k^2 \tag{1.16}$$

where R_{ij} is a tensor that describes distortion. The model was shown to accurately reproduce isotropic, kinematic, and distortional hardening effects. The parameter R_{ij} models both distortional and isotropic hardening of the yield surface. The rate equation for R_{ij} is,

$$\dot{R}_{ij} = -\dot{\lambda}u_{ij} \tag{1.17}$$

where u_{ij} is a unit tensor describing the direction of distortion and $\dot{\lambda}$ describes the magnitude of distortion. Isotropic hardening is handled by defining R_{ij} as proportional to the initial yield stress.

Zyczkowski and Kurtyka [8-10] constructed a model to describe yield surface distortion based on geometric arguments. The foundation of the model is based on the ability to describe a closed surface from two circles with different radii and center locations. The model is given by,

$$\sigma_j = Q_{ij}^{-1}\left\{ d_{(i)k}t_k + \left[\left(d_{(i)k}t_k\right)^2 - d_{(i)k}d_{(i)k} + R_{(i)}^2\right]^{1/2} \right\}t_i + \alpha_j \tag{1.18}$$

where Q_{ij} is a direction tensor, R_i is a vector containing the initial radii of the yield surface in the 5 independent dimensions, d_k measures the amount of distortion in each dimension, and t_k gives the direction of the distortion. It should first be noted that the subscripts i, j, and k, range from 1 to 5 due to the use of Ilyushin's 5-dimensional stress space. This model also does not follow the normal format of using a yield function, instead it directly calculates stresses at yielding. This means it does not follow with normal assumptions made in plasticity theory.

Rees [11] also developed a distortional model that uses up to rank six tensors to fully describe material hardening. One form of this model is given by,

$$f = C_{ij}\sigma_{ij} + C_{ijkl}\sigma_{ij}\sigma_{kl} + C_{ijklmn}\sigma_{ij}\sigma_{kl}\sigma_{mn} - k \qquad \textbf{(1.19)}$$

where C_{ij}, C_{ijkl}, and C_{ijklmn} are tensors whose parameters are characterized from experimental data. Consequently the model becomes very cumbersome to use.

A much more manageable tensor-based distortion model was developed by Voyiadjis et al. [12-13]. This model uses a rank four distortion tensor following Hill [14] and requires only four parameters for characterization. The model is defined as follows,

$$f = M_{ijkl}\left(s_{ij} - a_{ij}\right)\left(s_{kl} - a_{kl}\right) - k^2 \qquad \textbf{(1.20)}$$

where,

$$M_{ijkl} = \left(\frac{1}{4} + \frac{a}{2}\right)\left(\delta_{ik}\delta_{jl} + \delta_{il}\delta_{jk}\right) + \upsilon_{ij}\upsilon_{kl}\left[c \cdot H^{(1)} + d \cdot H^{(2)}\right]\upsilon_{rs}\left(s_{rs} - a_{rs}\right) \qquad \textbf{(1.21)}$$

where a_{ij} is the deviatoric back stress defined as,

$$a_{ij} = \alpha_{ij} - \frac{1}{3}\alpha_{kk}\delta_{ij} \qquad \textbf{(1.22)}$$

In the model, a is a parameter defining isotropic hardening, c and d define front and back distortion respectively. The tensor υ_{ij} is a unit tensor providing the preloading direction, where a unit tensor is given by $\|\upsilon_{ij}\| = 1$. Furthermore, $H^{(1)}$ and $H^{(2)}$ represent Heaviside functions which are defined as,

$$
\begin{aligned}
H^{(1)} &= H\left(\upsilon_{rs}\left(s_{rs} - \alpha_{rs}\right)\right) \\
H^{(2)} &= H\left(-\upsilon_{rs}\left(s_{rs} - \alpha_{rs}\right)\right)
\end{aligned}
\tag{1.23}
$$

where the Heaviside function is defined as,

$$
H(x) = \begin{cases} 1 & \text{if } x \geq 0 \\ 0 & \text{if } x < 0 \end{cases}.
\tag{1.24}
$$

This model has the capability to be linearized which makes it very useful to for this work. This feature allows the model parameters to be found using linear regression. This process will be discussed further in section 3.3.

1.3 Overview of Viscoplasticity

Time-dependent material response can occur in nearly all structural materials, but it is especially important at elevated temperatures. As a result, a model used to describe deformation in time-dependent material must be able to handle the effects of phenomena such as creep and stress relaxation. Models based on classical time-independent plasticity often have separate equations for time-independent and time-dependent strains. Making them seem like completely unrelated mechanisms. However, unified viscoplasticity models attempt to include all permanent deformations into a single inelastic strain term. The following sections briefly discuss the thermodynamic

framework that can be used to develop viscoplasticity models. Two viscoplasticity

models are then summarized.

1.3.1 Thermodynamic Basics for Unified Viscoplasticity

Elastic and inelastic deformations in materials can also be thought of as reversible

and irreversible processes. From this, the material response can be represented in a

thermodynamic framework. When constructing a viscoplasticity model from

thermodynamic arguments the basic principals must be obeyed.

- Conservation of Mass

$$\rho dV = \text{constant} \tag{1.25}$$

where ρ is density and dV is an infinitesimal volume element.

- Conservation of Linear Momentum

$$\int_R \rho b_i \, dV + \int_{\partial R} \sigma_{ij} n_j \, dS = \int_R \rho a_i \, dV \tag{1.26}$$

where b are body forces, a are accelerations, dS is an infinitesimal area, and n_j are

the components of a unit vector normal to the surface.

- Conservation of Angular Momentum

$$\int_R \rho e_{ijk} x_j b_k \, dV + \int_{\partial R} e_{ijk} x_j \sigma_{kl} n_l \, dS = \int_R \rho e_{ijk} x_j a_k \, dV \tag{1.27}$$

where x_j is a position vector and e_{ikl} is the permutation tensor.

- Conservation of Energy

$$\rho \dot{u} = \sigma_{ij} \dot{\varepsilon}_{ij} + \rho r - q_{i,i} \tag{1.28}$$

where $\dot{u}$ is the internal energy density, r is heat supplied, and $q_{i,i}$ heat flux.

- Clausius-Duhem Inequality

$$\rho \dot{s} - \rho \frac{r}{T} + \left(\frac{q_i}{T} \right)_{,i} \geq 0 \tag{1.29}$$

where $\dot{s}$ is the specific entropy and T is the absolute temperature.

1.3.2 State Law

In viscoplasticity the material state is more complex to define than in rate-independent plasticity. It is common to not only define the stress state (σ_{ij}), but also the absolute temperature (T) and an array of internal variables (ξ_α) to characterize the material state. Note, ξ_α can be a combination of vectors and tensors. The thermodynamic potential is given by the Gibbs free energy,

$$G = \sigma_{ij} \varepsilon_{ij} - H \tag{1.30}$$

where $H(\varepsilon_{ij}, T, \xi_\alpha)$ is the Helmholtz free energy given by,

$$H = u - Ts \tag{1.31}$$

where u is the specific internal energy and s is the specific entropy. The Gibbs free energy can be differentiated to give the following,

$$dG = \frac{\partial G}{\partial \sigma_{ij}} d\sigma_{ij} + \frac{\partial G}{\partial T} dT + \frac{\partial G}{\partial \xi_\alpha} \partial \xi_\alpha \tag{1.32}$$

such that,

$$\varepsilon_{ij} = -\frac{\partial G}{\partial \sigma_{ij}}, \qquad s = -\frac{\partial G}{\partial T}, \qquad p_\alpha = -\frac{\partial G}{\partial \xi_\alpha} \tag{1.33}$$

where p_α is a generalized force term. From this the total strain rate is given by,

$$\dot{\varepsilon}_{ij} = \frac{d}{dt} \left(-\frac{\partial G}{\partial \sigma_{ij}} \right) = -\frac{\partial^2 G}{\partial \sigma_{ij} \partial \sigma_{ikl}} \dot{\sigma}_{kl} - \frac{\partial^2 G}{\partial \sigma_{ij} \partial T} \dot{T} - \frac{\partial^2 G}{\partial \sigma_{ij} \partial \xi_\alpha} \dot{\xi}_\alpha \tag{1.34}$$

Under isothermal and linear elastic conditions the second and third terms go to zero.

1.3.3 Dissipation Potential

With the material state defined it is now possible to derive a flow law for viscoplasticity. In rate-independent plasticity the flow law was written in terms of a plastic potential function. Here a similar potential function is used, called the dissipation potential, $\Omega(\sigma_{ij}, T, \xi_\alpha)$. As a result the flow law can be written as,

$$\dot{\varepsilon}_{ij}^{in} = \frac{\partial\Omega}{\partial\sigma_{ij}}. \qquad (1.35)$$

It is clear from this definition that the dissipation potential evolves as inelastic strain is accumulated. The evolution equation can be expressed in terms of the internal state variable such that,

$$\dot{p}_\alpha = -\frac{\partial\Omega}{\partial\xi_\alpha} \qquad (1.36)$$

where $\dot{p}_\alpha$ is the first derivative of p_α with respect to time. When isothermal conditions are considered, Equation(1.29) can be given in terms of the Gibbs free energy,

$$\dot{p}_\alpha = -\frac{\partial^2 G}{\partial\xi_\alpha\partial\xi_\beta}\dot{\xi}_\beta. \qquad (1.37)$$

1.3.4 GVIPS Unified Viscoplasticity Model

The Generalized Viscoplasticity Model with Potential Structure (GVIPS), developed by Arnold et al. [15-17], provides a good example of a model derived from the method discussed in section 1.3.1-1.3.3. This model uses a yield criterion, one internal variable (back stress, α_{ij}), and an evolution law to account for nonlinear hardening.

For the GVIPS model the Gibbs free energy is given by,

$$G = G_E + G_I + G_A = -\frac{1}{2}C_{ijkl}\sigma_{ij}\sigma_{kl} - \sigma_{ij}\varepsilon_{ij}^{in} - B_0\left(g + B_1 g^{\,p}\right)\tag{1.39}$$

where ε_{ij}^{in} is the inelastic component of strain. The dissipation potential is,

$$\Omega = \frac{\mu f^{\,n+1}}{n+1} + \frac{R_\alpha B_0 g^{\,q+1}}{q+1}\,.\tag{1.40}$$

For the GVIPS model the internal state variable is the back stress, α_{ij}, which has the conjugate A_{ij}. The model is governed by three basic equations: the flow law,

$$\dot{\varepsilon}_{ij}^{in} = \dot{\lambda}\Sigma_{ij}\tag{1.41}$$

the evolution law,

$$\dot{A}_{ij} = \begin{cases} Q_{ijkl}C_{klpq}b_{pq} & \text{if } a_{ij}\Sigma_{ij} < 0 \\ b_{ij} & \text{if } a_{ij}\Sigma_{ij} \geq 0 \end{cases}\tag{1.42}$$

and the internal constitutive rate law,

$$\dot{a}_{ij} = L_{ijkl}\dot{A}_{kl}\tag{1.43}$$

where

$$\dot{\lambda} = \sqrt{\frac{\dot{\varepsilon}_{ij}^{in}\dot{\varepsilon}_{ij}^{in}}{2J_2}}\tag{1.44}$$

$$L_{ijkl} = Q_{ijkl}^{-1} = K_1\left(I_{ijkl} + K_2 a_{ij}a_{kl}\right)\tag{1.45}$$

$$b_{ij} = \dot{\varepsilon}_{ij}^{I} - K_3 a_{ij}\tag{1.46}$$

$$f = \left\langle \frac{\sqrt{3J_2}}{\kappa} - y \right\rangle\tag{1.47}$$

$$y = \left\langle 1 - \beta\sqrt{g} \right\rangle,\ g = \frac{3a_{ij}a_{ij}}{2\kappa_0^2}\tag{1.48}$$

$$J_2 = \frac{1}{2} \Sigma_{ij} \Sigma_{ij}, \quad \Sigma_{ij} = s_{ij} - a_{ij}. \tag{1.49}$$

In the above equations, f is the yield function, y defines the stress below which only

elastic strain exists, I_{ijkl} is the fourth order identity tensor, Σ_{ij} is the effective stress, J_2 is

the second invariant of deviatoric stress, and $\langle \ \rangle$ are the MacCauley brackets, defined as,

$$\langle x \rangle = \begin{cases} 0 & \text{if } x \leq 0 \\ x & \text{if } x > 0 \end{cases}. \tag{1.50}$$

The constants K_1, K_2, and K_3 contain the model parameters (B_0, B_1, R_α, κ_0, κ, β, n, p, q).

1.3.5 The Bodner Partom Model

The Bodner-Partom model (Bodner and Partom [18-19]) is presented as an

example of a viscoplasticity model that does not follow a thermodynamic framework.

Instead the model is based on dislocation dynamics and no formal yield function is used.

The Bodner-Partom model allows inelastic strains under any loading condition.

However, there are many loading conditions where the inelastic strain is insignificant

compared to the elastic term. A basic outline of the model is provided below, for more

information see Bodner and Partom [18].

The total strain rate is first broken down into an elastic and inelastic part,

$$\dot{\varepsilon}_{ij} = \dot{\varepsilon}_{ij}^e + \dot{\varepsilon}_{ij}^{in} \tag{1.51}$$

where $\dot{\varepsilon}_{ij}^e$ and $\dot{\varepsilon}_{ij}^{in}$ are the elastic and inelastic strain rates, respectively. The elastic strain

rate is given by the time derivative of Hooke's law and the inelastic strain rate is given by

the Prandtl-Reuss flow law (Equation 1.12). In this case the constant λ accounts for

isotropic hardening and is given by,

$$\lambda = \frac{D_0}{\sqrt{J_2} \, \exp\left[\left(\frac{Z^2}{3J_2}\right)^n \left(\frac{n+1}{2n}\right)\right]} \qquad (1.52)$$

where D_0, Z, and n are model parameters. Kinematic hardening is represented by using an effective internal variable,

$$Z_{eff} = Z_0 + q\int_0^t \dot{Z}(\tau)d\tau + (1-q)r_{ij}\int_0^t \dot{Z}(\tau)r_{ij}\,d\tau \qquad (1.53)$$

where

$$r_{ij} = \frac{\sigma_{ij}}{\sqrt{\sigma_{kl}\sigma_{kl}}} \qquad (1.54)$$

are the current stress direction cosines and the evolution equation is given by,

$$\dot{Z} = \frac{m(Z_1 - Z)\dot{W}_{in}}{Z_0} \qquad (1.55)$$

where $\dot{W}_{in} = \sigma_{ij}\dot{\varepsilon}_{ij}^{in}$ is the inelastic power. The parameters that must be determined are Z_0, Z_1, D_0, m, n, and q.

1.4 Yield Surface Experiments

There have been many experimental studies on the yield characteristics of metals. In this section, an attempt is made to review previous yield surface work that most closely pertains to the current study. Excellent review papers on yield surface experimental studies were written by Hecker [20] and Michno and Findley [21].

1.4.1 The Definition of Yielding

In most yield surface experimental studies the specimen of choice is the thin-walled tube. This type of specimen can easily be subjected to various ratios of axial and shear stress in order to map a yield surface in the axial-shear stress plane. In addition, the specimen can be subjected to internal pressure in order to define a three-dimensional yield surface.

When mapping yield loci there are two basic approaches. First, use a separate test specimen for each point on the surface, or use the same specimen to map an entire yield surface. The second approach is the most common because of the cost benefits and the elimination of specimen-to-specimen scatter. However, when using a single specimen to determine multiple yield points the state of the material must not change between each probe. This leads to a careful consideration of the definition of yielding.

There are many different definitions of yielding ranging from the standard 0.2% offset strain rule, which accumulates 2000 $\mu\varepsilon$ ($\mu\varepsilon = 10^{-6}$ m/m) of plastic deformation, to the proportional limit definition, where there is no plastic strain accumulated. The three most common definitions of yielding for yield surface evaluations are the proportional limit definition, the offset strain definition, and the back extrapolation definition. Each of these definitions can produce significantly different test results due to the sensitivity of yield to small amounts of plastic strain. Representations of these yielding criteria with respect to the stress-strain curve are shown in Figure 1.6.

The proportional limit criteria defines yield to occur at the point where plastic strain begins to accumulate. This method requires very precise measurements of strain in order to be sure that yielding is detected as the onset of non-linearity in the stress-strain curve. Phillips et al. [22 - 25] used a version of the proportional limit definition in

combination with a back extrapolation technique in order to define yielding with zero plastic strain. The method used involves first loading until two consecutive data points deviated to the same side of the linear elastic loading line. From here the last three points were fit with a line and yielding was defined as the intersection of this line and the linear elastic loading line.

The offset strain method is considerably easier to implement in experimental investigations. However, the magnitude of the offset strain is largely arbitrary, but different values can be required depending on material and loading rate. When used in multiaxial experiments the offset strain is given by an equivalent offset strain, such as,

$$\varepsilon_{eq}^{off} = \sqrt{\frac{2}{3}\varepsilon_{ij}^{off}\varepsilon_{ij}^{off}} = \sqrt{\left(\varepsilon_{11}^{off}\right)^2 + \frac{4}{3}\left(\varepsilon_{12}^{off}\right)^2}$$ (1.56)

where ε_{ij}^{off} is the offset strain tensor, and ε_{11}^{off} and ε_{12}^{off} are the axial and shear components respectively. Small offset strain values, on the order of 10 $\mu\varepsilon$, represent the initiation of yielding and are nearly the same as the proportional limit definition of yielding. However, larger offsets, such as the 0.2% offset criterion, give a macroscopic view of yielding and overall plastic flow. Because these large values cause considerable changes in material state the specimens cannot be used to determine multiple yield points in a locus. As a result, small offset strains are often used in yield surface experiments. Target offset values differ between experimental investigations. Some examples are, Helling et al. [26-28] used 5 $\mu\varepsilon$, Gil et al. [29-30] used 30 $\mu\varepsilon$, and Nouaihas and Cailletaud [31] used 100 $\mu\varepsilon$.

The back extrapolation method is probably least used of the methods described because it requires a material with near linear hardening characteristics. In addition, it is

often necessary to strain the test specimen well into the plastic region in order to fit a straight line. As a result, the test specimens can not be used for multiple yield point determinations. This technique was used by Taylor and Quinney [32] to determine the multiaxial yielding behavior of copper, aluminum, and mild steel.

The next question when developing a yield surface testing program is what control method should be used. The two most obvious choices are constant loading rate and constant strain rate. Studies performed by Phillips and Lu [25] and Wu and Yen [33] determined that there was no significant difference between stress-controlled and strain-controlled yield surfaces for pure aluminum specimens tested on a servohydraulic test machine.

Another consideration for yield surface studies is the effect of strain rate on yielding. Ellis et al. [34] performed a study on dependence of probing rate on the small offset yielding behavior of type 316 stainless steel at room temperature. It was found that for strain rates between 100 and 500 $\mu\varepsilon$/min there was no significant change in the yield surface. These results agree with classical rate-independent plasticity. However, plasticity is always rate-dependant to some degree and the rate dependence typically increases at elevated temperatures. This is especially true at high stresses. Therefore, the strain rate used during probing will play an increased role at elevated temperature.

1.4.2 The Yield Surface

Investigations of the initial yield surfaces of metals date back to before the aforementioned work of Taylor and Quinney [32]. Their research found that for copper and aluminum the von Mises yield criterion more accurately described initial yielding in

the axial-shear stress plane than the Tresca criterion. This conclusion has been confirmed by many other researches, such as, Phillips et al. [22], Liu [35], and Helling et al. [26].

The evolution of the yield surface, as a material is subjected to permanent deformation, is also of interest. What these subsequent yield surfaces look like depends on the definition of yielding used. If a large offset is used, such as the 2000 $\mu\varepsilon$ used by Hecker [36], the subsequent yield surface appears to be an isotropic expansion of the initial yield surface. However, if a small offset or proportional limit criterion is used the subsequent yield surface exhibits a combination of isotropic, kinematic, and distortional hardening. Experimental work done by Khan and Wang [37] provides a study of the effect of offset strains ranging from 200 to 2000 $\mu\varepsilon$ on yield surface shape.

In addition, yield surfaces can also exhibit substantial cross-effects. Positive cross-effects, an increase in the size of the yield surface normal to the prestrain direction, were found in studies performed by Phillips and Tang [23] and Wu and Yen [33]. In contrast, negative cross-effects (decrease in width normal to prestrain direction) were seen by Michno and Findley [21] in mild steels. A study by Williams and Svensson [38] showed that aluminum exhibited large cross-effects when subjected to torsion prestraining, but zero cross-effects after axial prestraining.

When analyzing subsequent yield surfaces it is quickly realized that isotropic hardening, kinematic hardening, and cross effects cannot fully explain experimental results. Subsequent yield surfaces also show considerable amounts of distortional hardening. This is characterized be a decrease in curvature of the yield surface in the direction opposite to the direction of prestraining. The yield surface also continues to exhibit symmetry about the axis of prestraining. These conclusions have been found by

many researches including Phillips et al. [22], Phillips and Moon [24], Helling et al. [26], and Wu and Yeh [33].
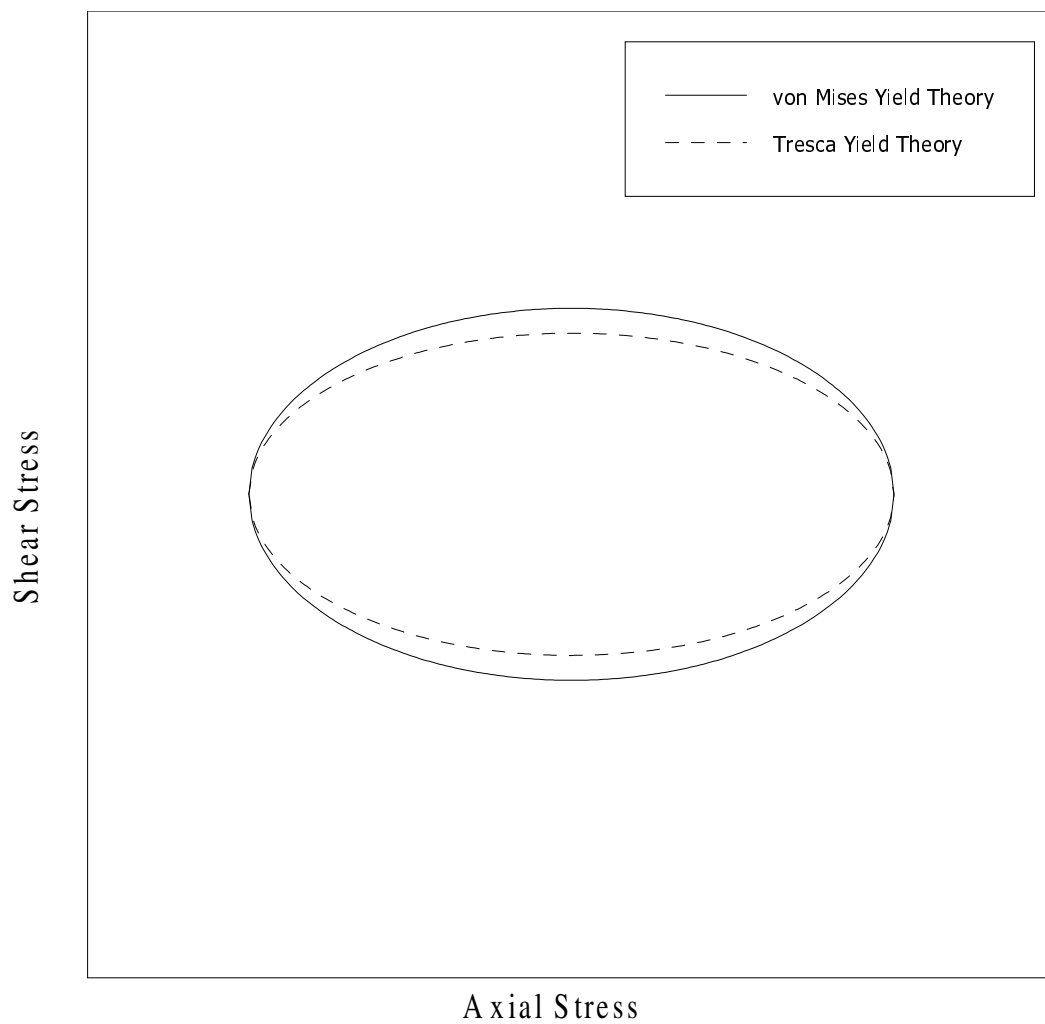
Figure 1.1: Relative difference between yield surfaces predicted by von Mises and Tresca yield criteria.
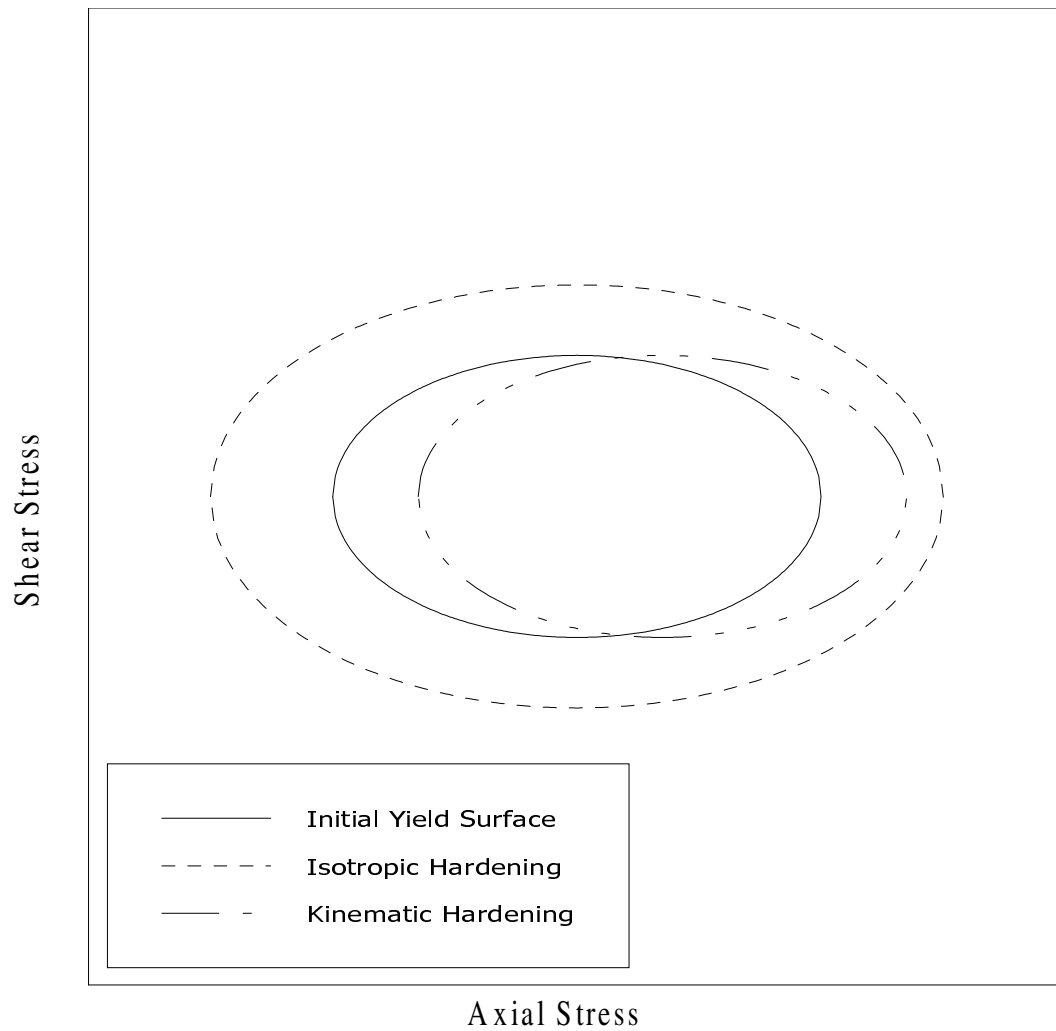
Figure 1.2: The effects of isotropic and kinematic hardening on an initial yield surface.
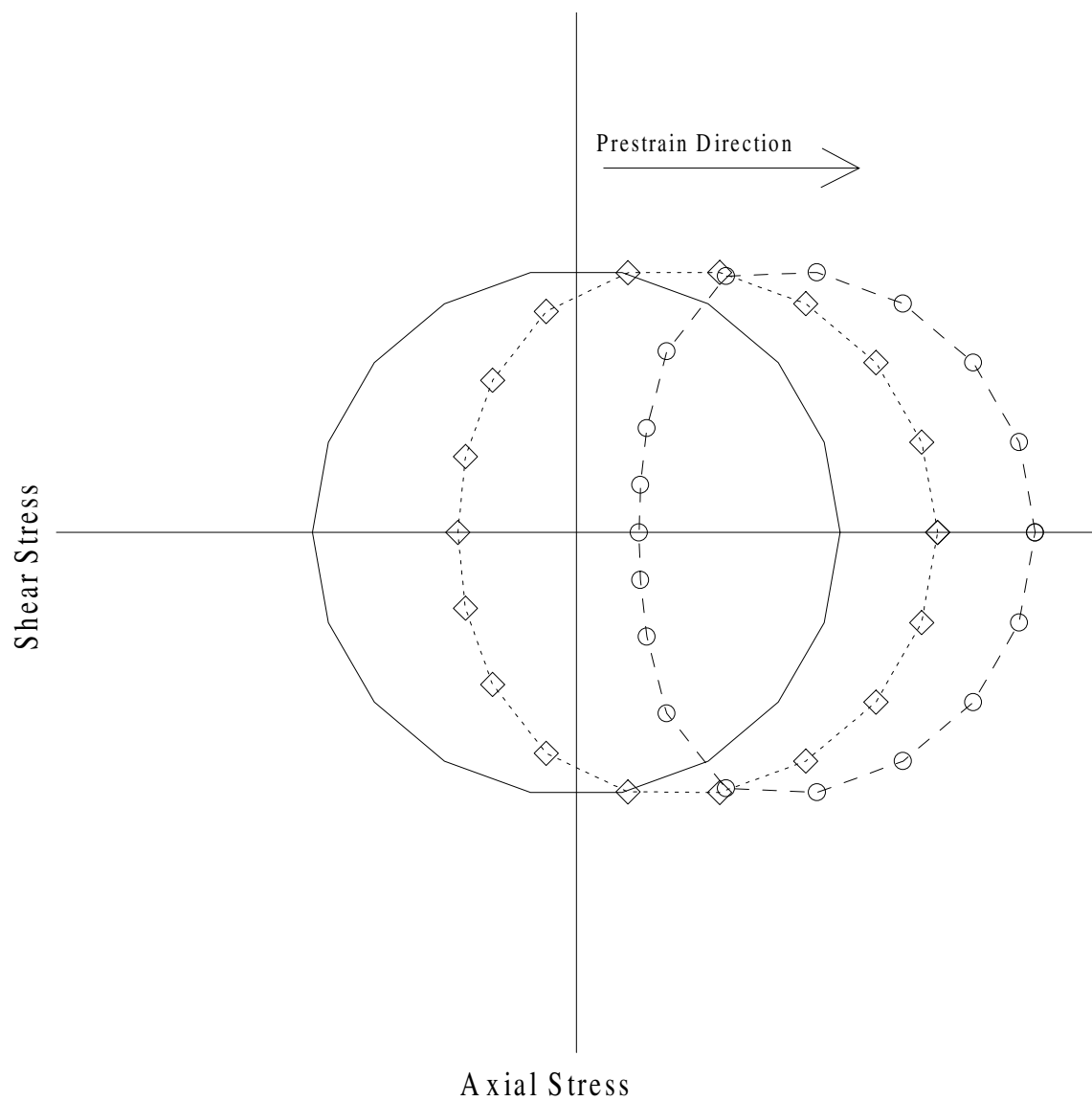
Figure 1.3: Change in curvature of the backside of a yield surface due to an axial prestrain.
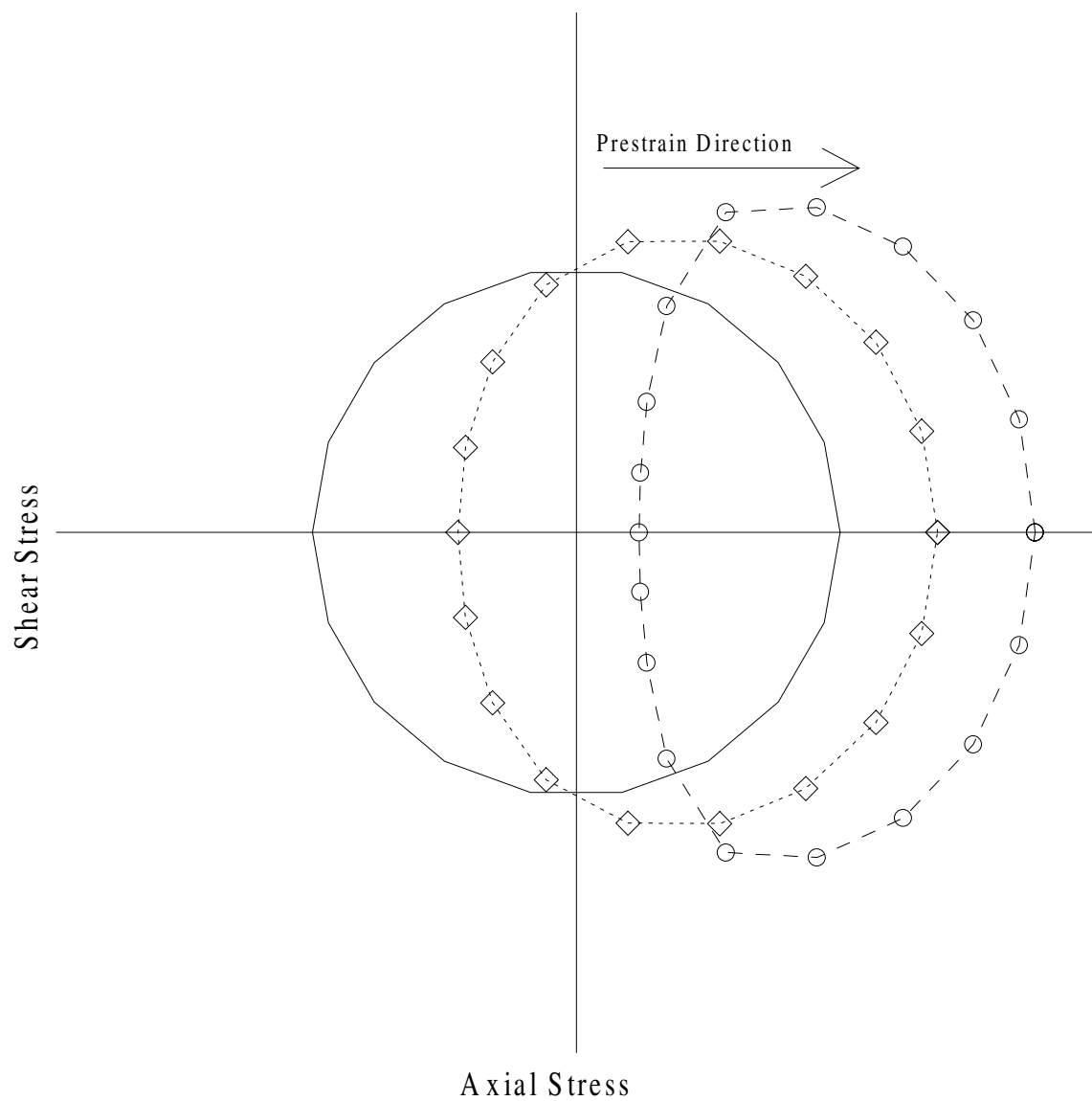
Figure 1.4: Change in curvature of the backside of a yield surface due to an axial prestrain with added cross effects.
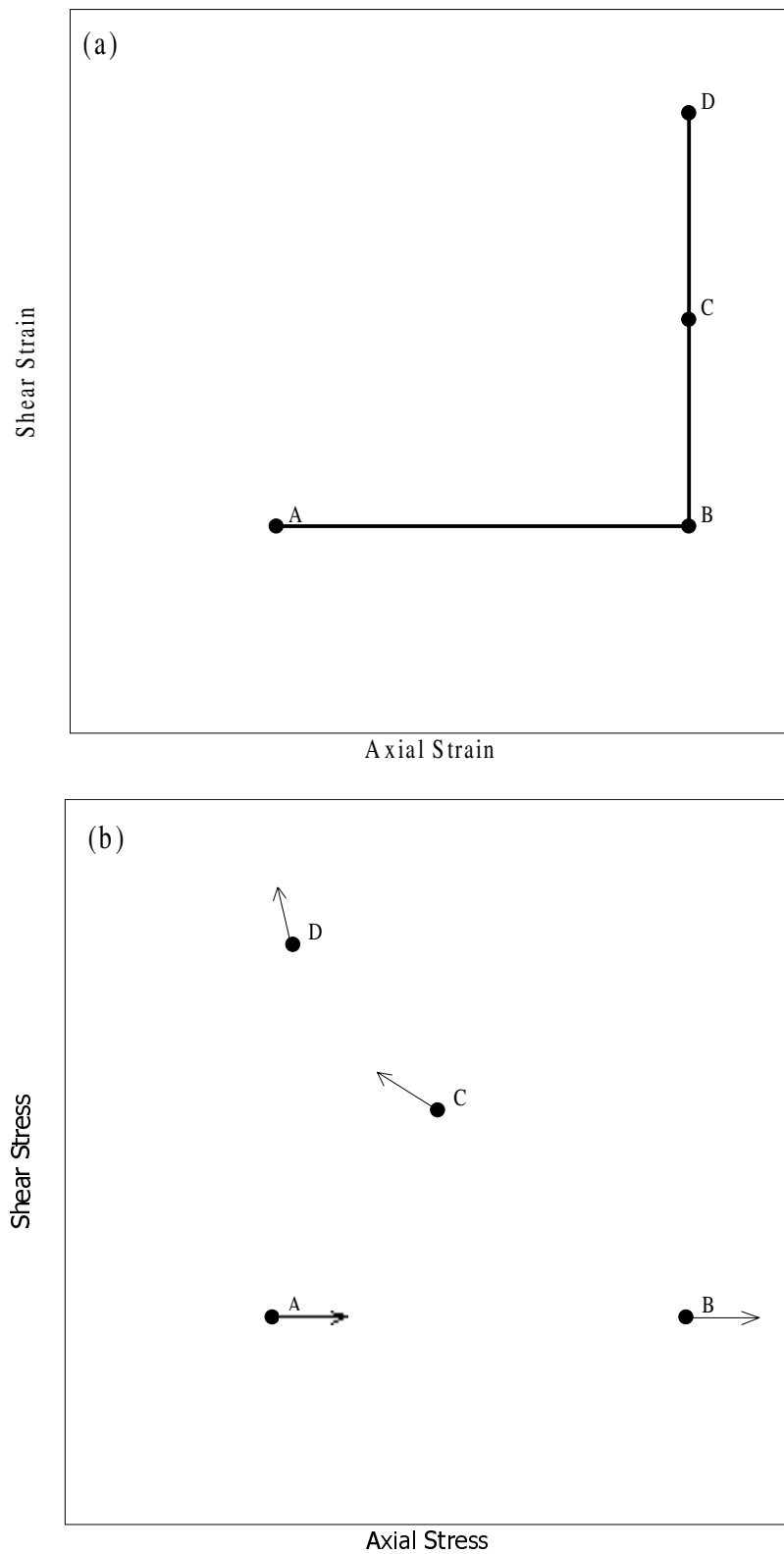
Figure 1.5: Difference between the direction of the strain rate and stress rate during a strain controlled nonproportional loading.
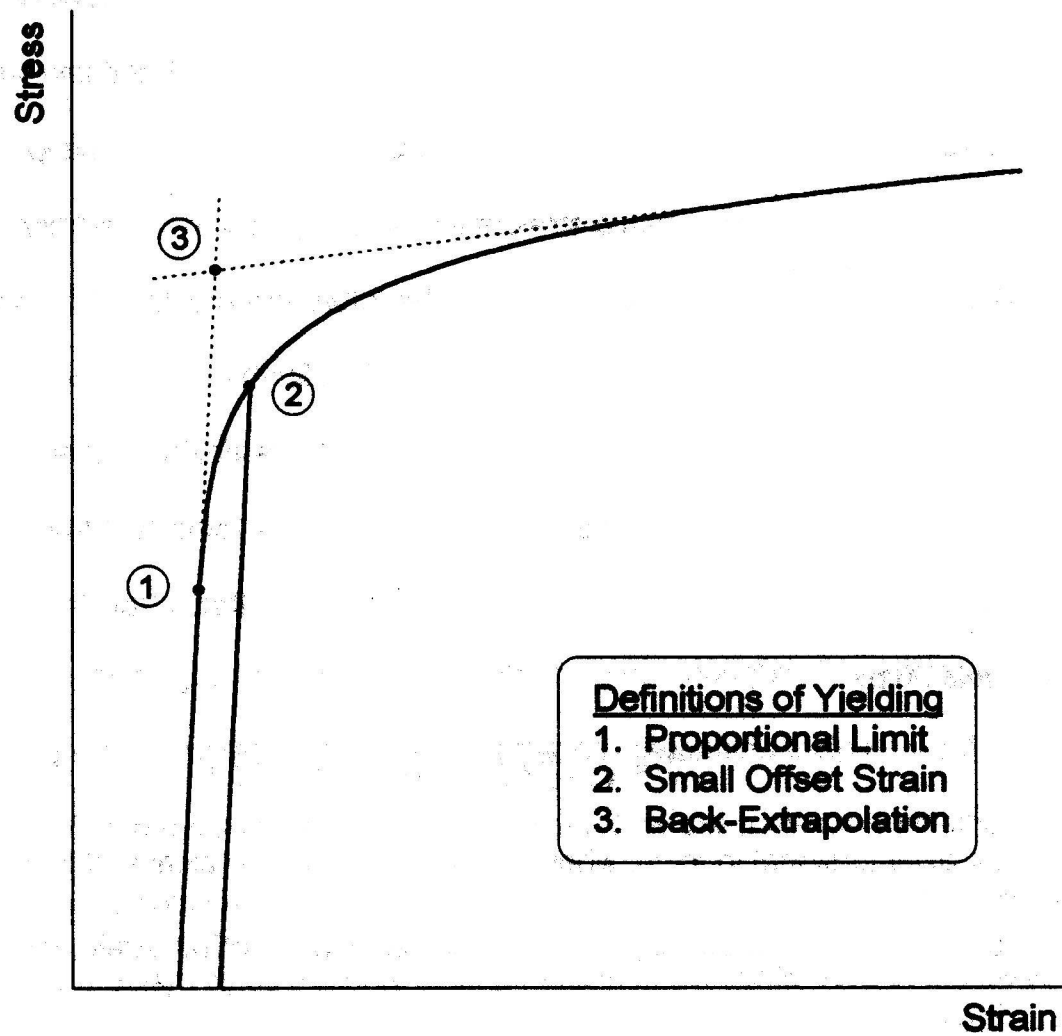
Figure 1.6: Yielding definitions used in yield surface experiments.

Chapter 2

Experimental Methods

The yield surface evolution experiments carried out for this study were complex and tedious. The following discussion concerns the methodology used in this study to perform yield surface evaluations and prestraining of the specimens. This chapter will discuss the materials, test specimen, test equipment, and test procedures used. The goal was to apply the same methodology to a wide range of materials in order to develop yield surface evolution equations.

2.1 Materials

This study consisted of testing three materials with significantly different compositions. The materials tested were Haynes 188, 316 stainless steel, and Inconel 718. By testing such different materials it was hoped that differences in the way the yield surfaces evolve could be seen.

2.1.1 Haynes 188

Haynes 188 (HN 188) is a cobalt-based alloy, see Table 2.1 for the composition given by the manufacturer. Its primary uses include nozzle guide vanes, stator blades, and combustion liners in aero-propulsion systems. The material was tested in a solution annealed state. In this state the microstructure contains second phase carbides that provide an additional hardening component to the material response. The solution annealing process was conducted as follows,

- Anneal at 1175°C for one hour.

- Cool to room temperature in Argon.

The elastic moduli for HN 188 as found from the current study are shown in Table 2.2. All the values in Table 2.2 are averages over each specimen tested from the initial yield surface experiments for each material.

	Fe	Ni	Cr	Co	C	S	Mn	Si	P
SS 316	67.08	10.2	17.7	0.19	0.04	0.013	1.75	0.57	0.03
HN 188	1.17	22.66	22.11	±38.7	0.09	0.002	0.80	0.35	0.005
IN 718	±18.6	53.58	17.52	0.39	0.034	0.002	0.12	0.07	0.006
	Mo	B	Cu	W	Nb+Ta	Ti	Al	La	N
SS 316	2.08	-	0.28	-	-	-	-	-	0.067
HN 188	-	0.003	-	14.06	-	-	-	0.052	-
IN 718	2.87	0.004	0.05	-	5.19	0.95	0.57	-	-

Note: SS 316 heat A12210, HN 188 heat 188061714, IN 718 heat S618

Table 2.1: Chemical Composition of Materials Tested.

	E (GPa)	G (GPa)
HN 188	187.0	71.6
SS 316	171.2	62.9
IN 718	144.4	54.8

Table 2.2: Mechanical Properties of Materials Tested. (Elastic and Shear Modulus)

2.1.2   316 Stainless Steel

Type 316 stainless steel (SS 316) is a stable austenitic alloy with relatively low strength that is primarily used for pressure vessels and piping. The SS 316 specimens were again solution annealed, but with the following procedure.

- Anneal at 1065°C for 30 minutes.

- Cool to 537°C in 9 minutes.

- Furnace cool to room temperature.

The composition of SS 316 is shown in Table 2.1 and the elastic moduli in Table 2.2.

2.1.3 Inconel 718

Inconel 718(IN 718) is a very high strength nickel-based alloy. It is mainly used in aeropropulsion applications for structural components such as disks, blades, and shafts. IN 718 was tested in an aged state. In order to reach this state the specimens were first solution annealed and subsequently aged. The thermal processing was conducted as follows.

- Anneal at 1038°C for 1 hour.

- Air cool to room temperature.

- Age in vacuum at 720°C for 8 hours.

- Cool to 620°C at 55°C/min and hold for 8 hours.

- Cool in Argon to room temperature.

This heat treatment produces γ'' precipitates that significantly increase the hardness of the material. Table 2.1 shows the chemical composition of IN 718 and Table 2.2 gives the elastic moduli.

2.2 Test Specimens

This section details the two different types of test specimen used. It also discusses the procedure for preparing a specimen to be tested.

2.2.1 Specimen Dimensions

All of the test specimens used where of the thin-walled tube type. However, two different size specimens were used. The specimen sizes have no effect on the testing procedure other than the physical setup of the load frame grips and geometric constants used for interpreting the test data. Both HN 188 and SS 316 used the specimen type referred to as the 2-inch specimen due to its two-inch diameter grip section. IN 718 is the specimen referred to as the 1-inch specimen due to its one-inch diameter grip section. The exact dimensions of the 2-inch and 1-inch specimens are shown in Figure 2.1.

2.2.2 Specimen Preparation

Prior to testing each new specimen needed to be dimpled in order to accept the biaxial extensometer and fitted with thermocouples. Dimpling consisted of placing two small indentations in the gauge section of the specimen for the extensometer probes to rest. This was performed by using a dimpling device custom built at NASA GRC. The equipment consisted of a base that firmly held the test specimen in place with a screw used to lower the dimpling tool (supplied with the extensometer) to the specimen. Torque was then applied to the screw via a torque wrench in order to dimple the specimen. This setup allowed the same dimpling force to be applied to each specimen, precisely controlling the size of the dimples. Table 2.3 show the dimpling torques used for each material.

Material	Torque (N*m)
HN 188	2.03
SS316	1.58
IN 718	1.81

Table 2.3: Dimpling torque.

The second step in preparing the test specimens was to spot weld thermocouples to the gauge section of the specimen. A total of three thermocouples were applied to each test specimen. The thermocouples were applied at the center and 12.5 mm above and below center on the gauge section. The center thermocouple was used to control the induction heating system. The remaining two thermocouples defined the temperature gradient across the gauge section.

2.3 Test Equipment

All experiments in this study were conducted on a computer controlled MTS biaxial servohydraulic test machine. The machine is pictured in Figure 2.2 and is located in the NASA GRC multiaxial fatigue lab. The maximum capacities of the load frame are ±220,000 N axial loading and ±2,260 N*m twisting moment. The test specimen is held by water-cooled, hydraulically actuated grips. The top grip is fixed while the bottom grip is attached to a hydraulic actuator that is capable of independent vertical translation and rotation. Two MTS 458 analog controllers, one for axial motion and one for torsional motion, control the actuator. Further details about the biaxial test machine are given by Kalluri and Bonacuse [39].

Specimen heating was accomplished by using a closed-loop induction heating system as described by Ellis and Bartolotta [40]. The system consisted of an Ameritherm 15-kW radio frequency induction heating unit and three adjustable, water-cooled copper coils surrounding the gauge section of the specimen. The copper coils could be raised or lowered independently along the gauge section of the test specimen in order to obtain an

acceptable temperature gradient (± 1% of the absolute test temperature). See Figure 2.3 for a photo of the copper coils around a 1-inch specimen.

In order to conduct yield surface studies, strain measurements accurate to the microstrain level are required. This is because loading must be quickly stopped once yield is detected in order to ensure the material state is not significantly disturbed. In addition, the device used to measure strain must also perform on a micro strain level at elevated temperatures. This depends not only on the strain measurement device, but also on the ability of the heating equipment to maintain a constant temperature and the elimination of electronic noise.

This study utilized an MTS water-cooled biaxial extensometer capable of operating over a large temperature range. The extensometer used two alumina rods, spaced 25mm apart to measure axial deformation and twist. The alumina rods fit into the dimples placed in the test specimen as discussed earlier. Lissenden et al. [41] supply further details on the biaxial extensometer. The biaxial extensometer mounted to a specimen is shown in Figure 2.3.

Custom written software and a PC were used to control all experiments. The PC was equipped with analog-to-digital (A/D) and digital-to-analog (D/A) hardware. The D/A hardware sent a command signal from the PC to the load frame while the A/D hardware received test data. Both sampled at 1000 Hz. The test data received by the A/D hardware averaged the data over every 100 points in order to minimize the effects of electronic noise, providing 10 data points per second written to output files.

The test program utilized two separate control programs. One was used to determined the yield points used to construct the yield loci while the other program preformed the preloadings.

2.4 Strain Controlled Load Paths

All three materials were subjected to a series of three strain controlled load paths. Path I is purely axial strain, Path II is purely shear strain, and Path III is a non-proportional strain path. A schematic of each load path is shown in Figure 2.4. Along each load path several stops were made in order to conduct a pair of yield surface determinations. These points are indicated by letters in Figure 2.4. In addition, each load path was cycled either two or three times depending on the hardening characteristics of each material. For each load path the maximum equivalent strain is 15,000 $\mu\varepsilon$, shown by a dashed circle in Figure 2.4.

Three additional load paths were carried out on IN 718. These paths were not carried out on the other materials due to time constraints and the lack of success with IN 718. These additional load paths all subject the material to both axial and torsional strain. They are designated Path IV, Path V and Path VI and are shown in Figure 2.5.

All six load paths used an equivalent strain rate of 100 $\mu\varepsilon$/s. For axial-torsional loading equivalent strain is given by,

$$\dot{\varepsilon}_{eq} = \sqrt{\frac{2}{3}\dot{\varepsilon}_{ij}\dot{\varepsilon}_{ij}} = \sqrt{\frac{2}{3}\left[\left(1+2\nu^2\right)\dot{\varepsilon}_{11}^2 + 2\dot{\varepsilon}_{12}^2\right]} \tag{2.1}$$

where $\dot{\varepsilon}_{ij}$ is the strain rate tensor, ν is Poisson's ratio, and $\dot{\varepsilon}_{11}$ and $\dot{\varepsilon}_{12}$ are the tensorial axial and shear strain rates respectively.

2.5 Yield Loci

Each yield locus was constructed by probing for yielding in 16 unique directions in the axial-torsional stress plane. The angles used for probing were identical for each locus, however the order of probing varied depending on the prestrain history of the material. The angles were always setup in such a fashion that the first probe was in a direction normal to the prestrain direction. Furthermore, the order of subsequent probes was chosen in order to minimize the changes to the material state. For example, Figure 2.5 shows the order of probing following a torsional prestrain. In this pattern, the angle between probes was either 180° or 90° in the hopes that the effects of the probes would counteract each other. Minimization of the changes in material state while performing yield surface determinations is further discussed by Hecker [42]. In addition, each yield surface was repeated to verify that the material state was undisturbed.

Each of the 16 individual yield probes can be broken down into the following three step process,

(i)   Use a least squares fit to determine the coefficients of the elastic loading line over a predefined stress range within the elastic region. These coefficients include the elastic modulus, E, shear modulus, G, and initial stresses σ_{11}^0 and σ_{12}^0.

(ii)   Continuously calculate the offset strain components using the following equations,

$$\varepsilon_{11}^{off} = \varepsilon_{11} - \frac{\sigma_{11} - \sigma_{11}^{off}}{E} \qquad\qquad (2.2)$$

$$\varepsilon_{12}^{off} = \varepsilon_{12} - \frac{\sigma_{12} - \sigma_{12}^{off}}{2G} \qquad \textbf{(2.3)}$$

From this determine the equivalent offset strain (Equation 1.33) and

compare it to the target value of 30 με.

(iii)   Once the equivalent offset strain exceeds the target value unload the probe

to the starting position.

The 30 με value for the offset strain was chosen based on previous experience

from studies performed by Lissenden et al. [43] and Gil et al. [44]. In order to obtain

optimum results with the least scatter each material used a different probing rate. Prior to

testing a material a rate study was performed in order to determine the optimum probing

rate. This was done by conducting initial yield surfaces tests for each material at various

stress rates. Multiple runs of each rate were perform and the rate that showed the best

repeatability was used as the yield surface probing rate for that material. The results of

these rate studies are given in Table 2.4.

Material	Equivalent Stress Rate (MPa/s)	Equivalent Elastic Strain Rate (μm/m/s)
IN 718	2.07	10
HN 188	17.9	100
SS 316	7.24	50

Table 2.4: Yield surface probing stress rates.
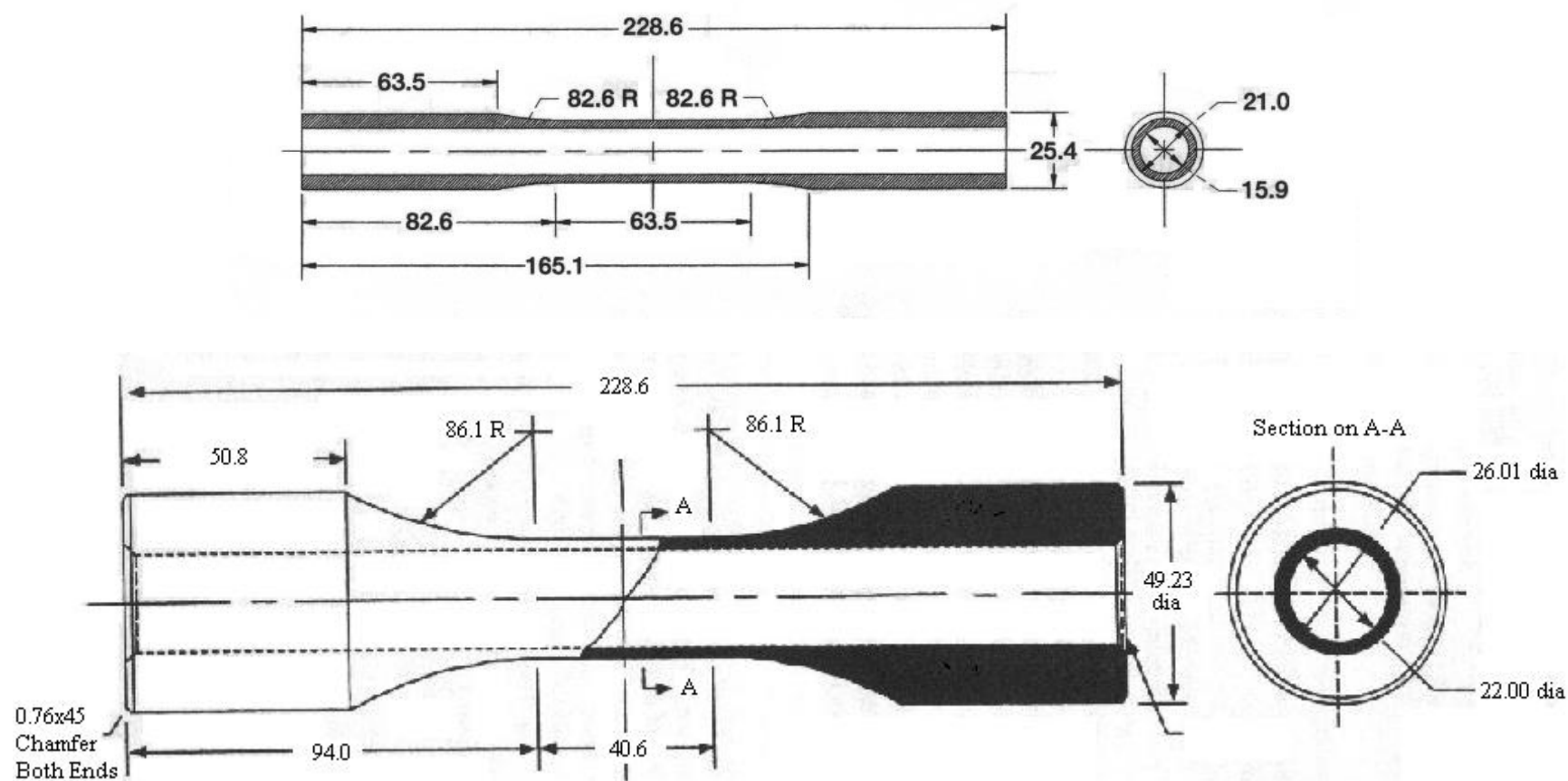
Figure 2.1: Specimen geometry, 2-inch specimen (top) and 1-inch specimen (bottom). (All measurements in mm.)

Figure 2.2: Axial-Torsional test machine and MTS 458 analog controller.
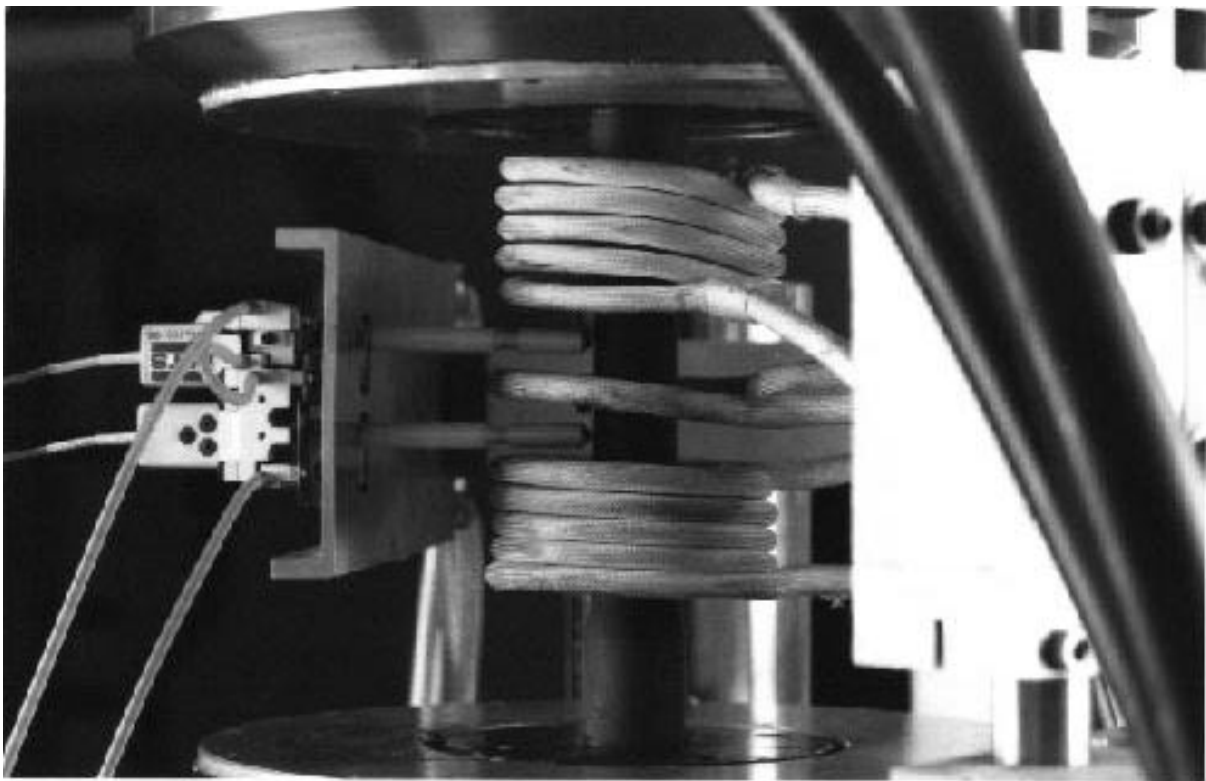
Figure 2.3: Gripped 1-inch specimen with mounted biaxial extensometer and induction heating coils.
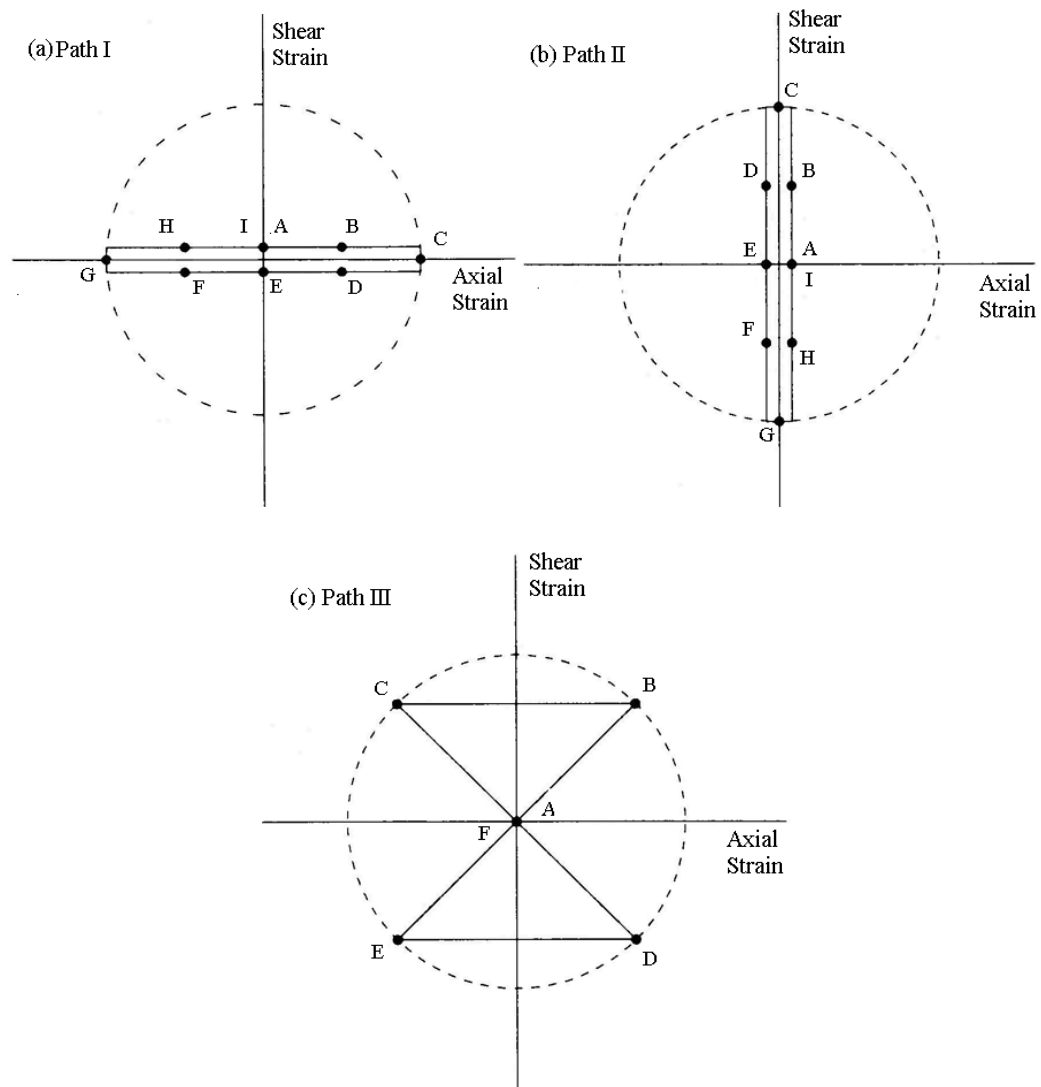
Figure 2.4: Strain controlled paths, (a) pure axial Path I, (b) pure shear Path II, (c) combined axial-shear Path III.
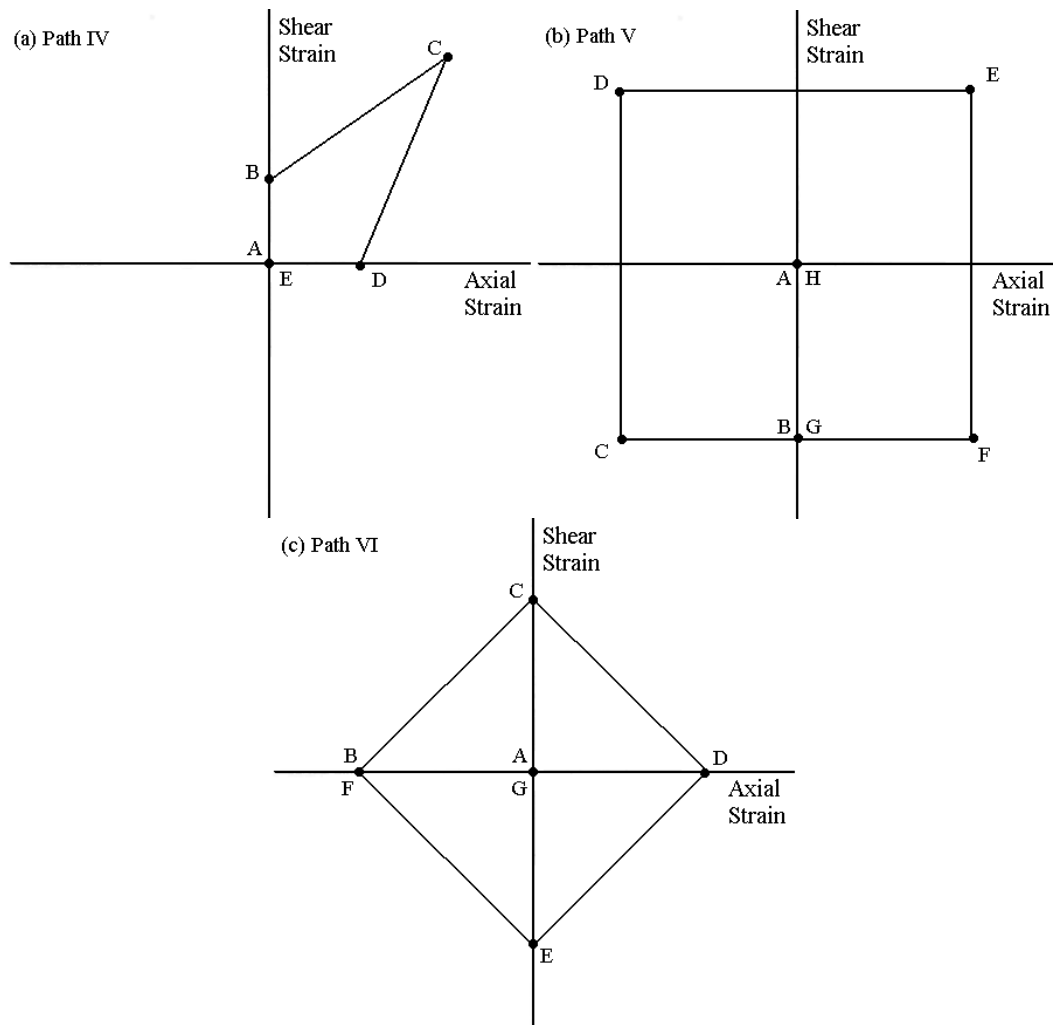
Figure 2.4: Additional In 718 strain paths, (a) Path IV, (b) Path V, (c) Path VI.
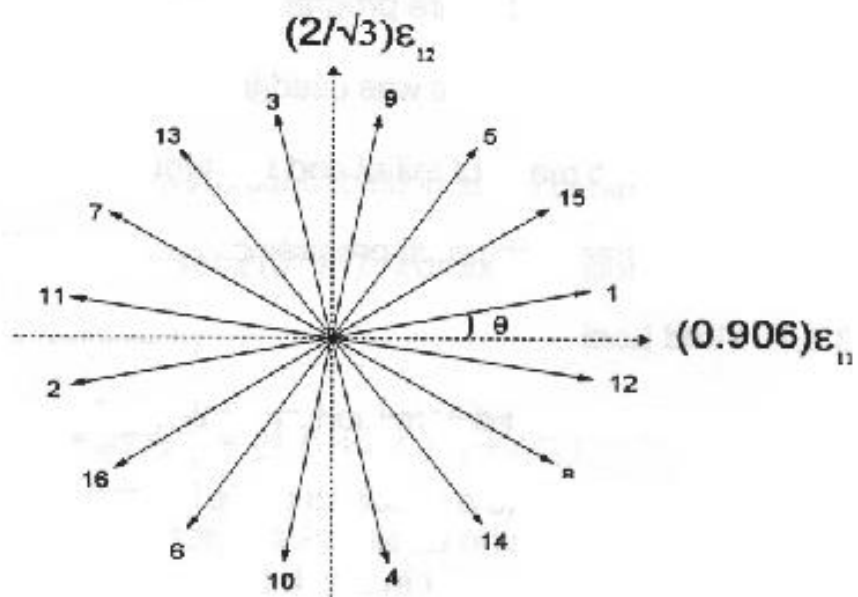
Probe Number	Probe Angle	Probe Number	Probe Angle
1	12°	9	79°
2	192°	10	259°
3	102°	11	170°
4	282°	12	350°
5	57°	13	125°
6	237°	14	305°
7	147°	15	35°
8	327°	16	215°

Figure 2.5: Example of probing order after a torsional prestrain.

Chapter 3

Data Analysis

The overall goal of this research was to describe the evolution of the yield surface when subjected to plastic deformation. As a result, an integral part of the data analysis was to find a way to describe the yield surface by a model with parameters that change as the yield surface evolves. The first section of this chapter will discuss some of the attempts made to find such a model. Section 3.2 will discuss how the model developed by Voyiadjis et al. [13] and its parameters were used to reproduce yield surfaces and how the model parameters affect its shape, size, and position. Section 3.3 will detail the steps taken to reduce the model to an axial-torsional form that could be fit using linear regression. Finally, Section 3.4 will discuss the statistical methods used to quantify goodness of fit.

3.1 Mathematical Representation of Yield Surfaces

The first attempts made at fitting a shape to the yield surface data collected in this study applied the simplistic approach of fitting a circle with a flattened backside. The definition of the backside of a yield surface is the portion of the yield surface from approximately 90 to 270 degrees from the prestrain direction. This initial attempt to describe the yield surface was based on two principles; (i) the initial yield surface as well as the front side of the yield surface are circular in the σ_{11}-$\sqrt{3}\sigma_{12}$ stress plane, (ii) the backside of the surface flattens compared to the front and can be represented by a straight

line. This representation proved adequate for describing yield surfaces with little or no distortion, however, it quickly faltered when exposed to highly distorted yield surfaces. In addition, the backside of the yield surface is not a straight line even when significant distortion is present.

The second approach involved the regression of polynomials. Since the problem at hand is highly nonlinear the polynomials needed to be of order 2 or greater. Furthermore, terms involving both axial and shear stress needed to be included in order to obtain the distorted shape of the yield surface. As a result, the regression parameter became very complex. Nonetheless, the major shortcoming of the approach came from the fact that it was not always possible to obtain a continuous smooth surface. When used to predict a yield surface, the polynomial regression often produced a cusp when the curve intersected the axial-stress axis. This was not consistent with any of the experimental results collected.

The polynomial approach was extended to include conformal mapping. It was hoped that a data conversion could be found that would allow the data to be fitted and then converted back to its original form. This process again produced non-continuous yield surfaces. In addition, the mapping process increased the error between data and fit curves resulting in poor yield surface representations.

Finally it was decided that a yield function approach was needed. Several yield function based distortional models were discussed in Section 1.2.5. Of these, the model developed by Voyiadjis et al. [12, 13] was chosen for two reason: (1) it produced a continuous convex yield surface, (2) all of the pertinent yield surface characteristics

could can be controlled by four parameters. From this point this distortion model will be referred to as the Voyiadjis model.

3.2 Yield Surface Representation

The algorithm used to reproduce a yield surface once the model parameters were determined did not require a reduction to the axial-torsional form. The Voyiadjis model was used in the form shown in Equations 1.20 and 1.21 and programmed in to MathCAD. The yield surface was predicted by incrementing stress in the same probing direction used in the experimental portion of this study. First the program automatically found the starting stress point for all probes. To do this, probes 1 and 2 were fit with a line as well as probes 3 and 4. The intersection between these two lines gave the initial stress point for probing, as shown in Figure 3.1 where C represents the center of probing. From this point probing is carried out in all directions. This technique produced yield points in the same directions as the experimentally determined yield points.

Each of the four parameters control a different type of hardening. The parameter a is related to isotropic hardening. Its value does not have a bound, but $a=1$ corresponds to a radius equal to the initial yield strength averaged from all specimens tested, k_0. Then if $a>1$ the yield surface is smaller than the initial surface and if $a<1$ the yield surface is larger than the initial surface. This is shown in Figure 3.2. The parameter d determines the amount of distortion there is in the backside of the yield surface. A value of zero gives no distortion. If the value is greater then zero than the yield surface distorts with an increase in curvature along the backside, as shown in Figure 3.3. If the value of d is less then zero the yield surface distorts with a decrease in curvature, as shown in Figure 3.4. The backstress parameters, α_{11} and α_{12}, control the location of the center of the yield

surface. The values of these parameters depend on the properties of the material being tested, but they generally have an association with the maximum stress reached during a preloading.

The value of the directional unit tensor, υ_{ij}, was calculated from the prestrain direction. Since all preloadings occurred in the axial-shear strain plane the axial and shear proportions of the loadings could be found from the cosine and sine of the loading angle respectively. If the directional tensor is given as,

$$\upsilon_{ij} = \begin{bmatrix} x \cdot \cos\theta & x \cdot \sin\theta & 0 \\ x \cdot \sin\theta & 0 & 0 \\ 0 & 0 & 0 \end{bmatrix} \tag{3.1}$$

where θ is the prestrain direction. By enforcing $\|\upsilon_{ij}\| = 1$ the value of x can be found from,

$$x^2 \cos^2\theta + 2x^2 \sin^2\theta = 1. \tag{3.2}$$

3.3 Parameter Determination for the Voyiadjis Model

The first step in determining the parameters for the Voyiadjis model was to reduce it to its axial-torsional form by making the appropriate assumptions. Since the entire set of yield surface data is in the axial-torsional stress space the stress and backstress tensors can be reduced to,

$$\sigma_{ij} = \begin{bmatrix} \sigma_{11} & \sigma_{12} & 0 \\ \sigma_{12} & 0 & 0 \\ 0 & 0 & 0 \end{bmatrix} \qquad \alpha_{ij} = \begin{bmatrix} \alpha_{11} & \alpha_{12} & 0 \\ \alpha_{12} & 0 & 0 \\ 0 & 0 & 0 \end{bmatrix}. \tag{3.3}$$

The deviatoric stress and deviatoric backstress are,

$$s_{ij} = \begin{bmatrix} \dfrac{2}{3}\sigma_{11} & \sigma_{12} & 0 \\[2mm] \sigma_{12} & -\dfrac{1}{3}\sigma_{11} & 0 \\[2mm] 0 & 0 & -\dfrac{1}{3}\sigma_{11} \end{bmatrix} \qquad a_{ij} = \begin{bmatrix} \dfrac{2}{3}\alpha_{11} & \alpha_{12} & 0 \\[2mm] \alpha_{12} & -\dfrac{1}{3}\alpha_{11} & 0 \\[2mm] 0 & 0 & -\dfrac{1}{3}\alpha_{11} \end{bmatrix}. \tag{3.4}$$

One additional assumption is that the direction tensor, υ_{ij}, is also contained in the axial-torsional plane giving,

$$\upsilon_{ij} = \begin{bmatrix} \upsilon_{11} & \upsilon_{12} & 0 \\ \upsilon_{12} & 0 & 0 \\ 0 & 0 & 0 \end{bmatrix}. \tag{3.5}$$

When the above assumptions are made only 25 of the 81 components of the tensor M_{ijkl} (Equation 1.21) are non- zero. Next, M_{ijkl} is substituted into Equation 1.20 and the number of non-zero components furthers reduces to 11 for the completed axial-torsional form of the Voyiadjis model.

With the axial-torsional reduction completed, work was initiated to obtain a form that could be used with a regression technique in order to obtain the model parameters. The problem was originally approached with the desire to obtain all four model parameters directly from regression. However, it is assumed that the backstress follows the same direction as the prestrain direction. As a result, it was easier to use an iterative method to find the backstress. An initial guess was input and the value was incremented in the direction of prestrain until the fit no longer improved. The method used to quantify the goodness of fit will be discussed in the next section. Since the backstress was not included in the regression the model reduced to a simple linear problem with the following characteristic equation,

$$Y = \beta_0 k_0^2 + \beta_1 Z \tag{3.6}$$

where,

$$Y = \frac{2}{3}\sigma_{11}^2 + 2\sigma_{12}^2 - \frac{4}{3}\alpha_{11}\sigma_{11} - 4\alpha_{12}\sigma_{12} + \frac{2}{3}\alpha_{11}^2 + 2\alpha_{12}^2 \tag{3.7}$$

$$Z = H_0^{(2)}*W*\left[\frac{4}{9}\sigma_{11}^2 v_{11}^2 - \frac{8}{9}\sigma_{11}\alpha_{11}v_{12}^2 + \frac{8}{3}\sigma_{11}\sigma_{12}v_{11}v_{12} - \frac{8}{3}\sigma_{11}\alpha_{12}v_{11}v_{12}\right.$$
$$\left. - \frac{8}{3}\sigma_{12}\alpha_{11}v_{11}v_{12} + \frac{8}{3}\alpha_{11}\alpha_{12}v_{11}v_{12} + 4\sigma_{12}^2 v_{12}^2 - 8\sigma_{12}\alpha_{12}v_{12}^2 + 4\alpha_{12}^2 v_{12}^2 + \frac{4}{9}\alpha_{11}^2 v_{11}^2\right] \tag{3.8}$$

$$W = \left(\frac{2}{3}\sigma_{11}v_{11} - \frac{2}{3}\alpha_{11}v_{11} + 2\sigma_{12}v_{12} - 2\alpha_{12}v_{12}\right) \tag{3.9}$$

$$H_0^{(2)} = H(-W) \tag{3.10}$$

$$\beta_0 = \frac{1}{\left(\dfrac{1}{2}+a\right)} \tag{3.11}$$

$$\beta_1 = \frac{-d}{\left(\dfrac{1}{2}+a\right)} = -d*\beta_0 \tag{3.12}$$

and k_0 is the initial yield strength averaged over all specimens of the same material tested.

Linear regression was applied to Equation 3.6 to obtain following system of equations

that can be solved by using matrix inversion,

$$\begin{bmatrix} n \cdot k_0^2 & \sum Z \\ k_0^2 \cdot \sum Z & \sum Z^2 \end{bmatrix} \begin{Bmatrix} \beta_0 \\ \beta_1 \end{Bmatrix} = \begin{Bmatrix} \sum Y \\ \sum YZ \end{Bmatrix} \tag{3.12}$$

where *n* denotes the number of probes in a yield surface. Finally Equations 3.11 and 3.12

are used to solve for *a* and *d*.

The yield surface fits were produced using both repeated yield surfaces at each point along a load path. This provided a maximum of 32 separate yield points in 16 directions for each yield surface. Prior to, fitting the data were inspected visually to determine if a set contained outliers. A point was considered an outlier if it clearly did not fit the pattern suggested by the remaining data points. If a point was suspected of being an outlier fits were conducted with and without the data point and the better of the two was accepted. Yield points were excluded on an individual basis. If a yield point was excluded the corresponding point in the repeated surface was not necessarily excluded.

3.4 Goodness of Fit Statistics

The next problem was to quantify the goodness of the fit reproduced by the outlined process. Since linear regression was used the correlation coefficient was found to be sufficient for analyzing the fits. The experimental data and model predictions had to first be converted to fit the form given by Equation 3.6. This was accomplished by substituting the data and model parameters into Equations 3.7 and 3.12. The correlation coefficient statistic in terms of Y and Z is,

$$R = \frac{\sum ZY - \dfrac{\sum Z \sum Y}{n}}{\sqrt{\left(\sum Z^2 - n\bar{Z}^2\right)\left(\sum Y^2 - n\bar{Y}^2\right)}} \qquad (3.12)$$

where $\bar{Z}$ and $\bar{Y}$ are the average of all Z and Y values respectively. The value of R was then squared to get the coefficient of determination. It is stated by Kiemele et al. [45] that $|R| > 0.7$ represents a good fit. However the yield surface data did not produce R^2 values that large, but still produced good fits in the axial-torsional stress plane. The

actual R^2 values range between 0.4 and 0.15. There is a correlation between R^2 and cycle number such that the R^2 values tend to decrease in the later cycles. This is largely due to an increase in experimental scatter in the later cycles. In addition, the fits used were not always statistically the best fit. This is due to the assumption that $d{\leq}0$. All fits used were the best fit where this assumption was satisfied.

3.5 Yield Surface Fitting Methodology

Each yield surface was fit using the same series of steps. First an initial guess for the backstress parameters was made. This was accomplished by fitting a circle to the front side of the yield surface and using the center of the circle as the backstress. This worked very well for initial yield surfaces and for surfaces in the first cycle of a strain path. However, surfaces from later cycles sometimes required the initial backstress to be determined from experience. This was because as the distortion increased in later cycles the backstress no longer corresponded with the center of the front side. Therefore the initial backstress was obtain from the patterns observed in the evolution of the backstress from the initial cycle.

Once an initial backstress was found the yield function was fit to the experimental data. The fitting process produced the isotropic parameter, a, and the distortional parameter, d, for a given backstress. Next, the backstress was incremented in the direction of prestraining. Because of this iterative process it was often desirable to make the initial guess for the backstress slightly under predict the magnitude of the expected final backstress value. This enabled the generation of data on both sides of the optimum fit. The best fit was the one with the largest R^2 statistic and a negative value of d.

Once the best fit was obtained, it was compared to the experimental data in order to search for possible outliers. An outlier was considered to be a yield point that did not follow the pattern given by the other data. Outliers were determined largely by judgment. However, if a yield point was suspected it was removed from the fit and the entire process outlined above was conducted again. The new fit, without the outlier, was then compared to the original. The fit that had the largest R^2 statistic was then chosen as the fit for that yield surface.
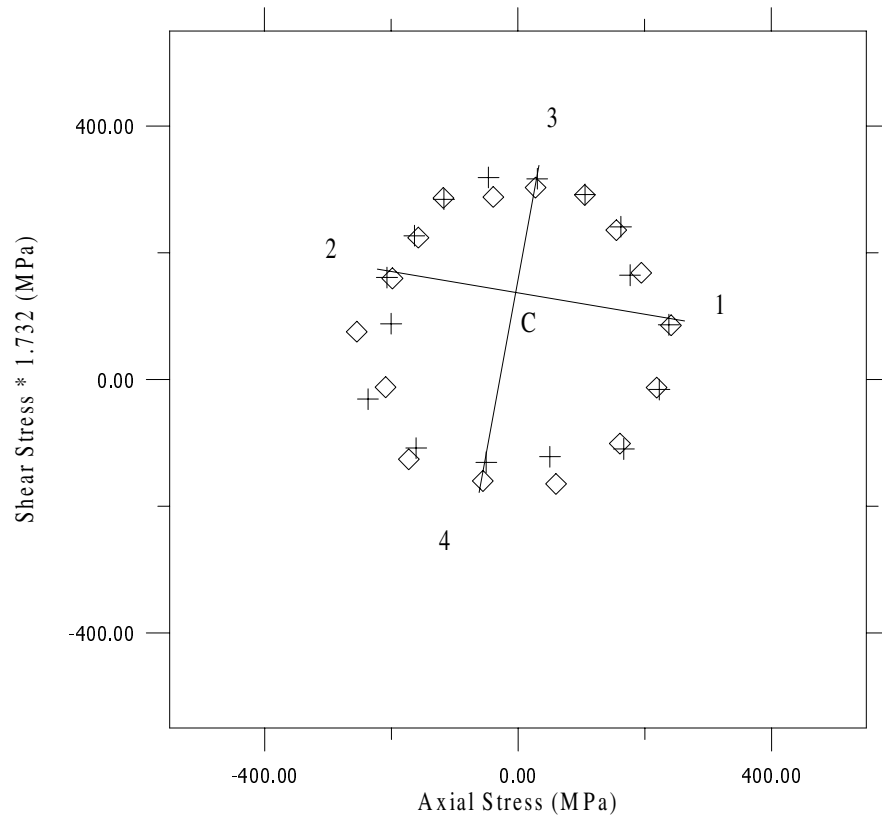
Figure 3.1: HN 188 Path II, Point C, Cycle 1 showing how the intersection of two lines between yield points gives the center of probing.
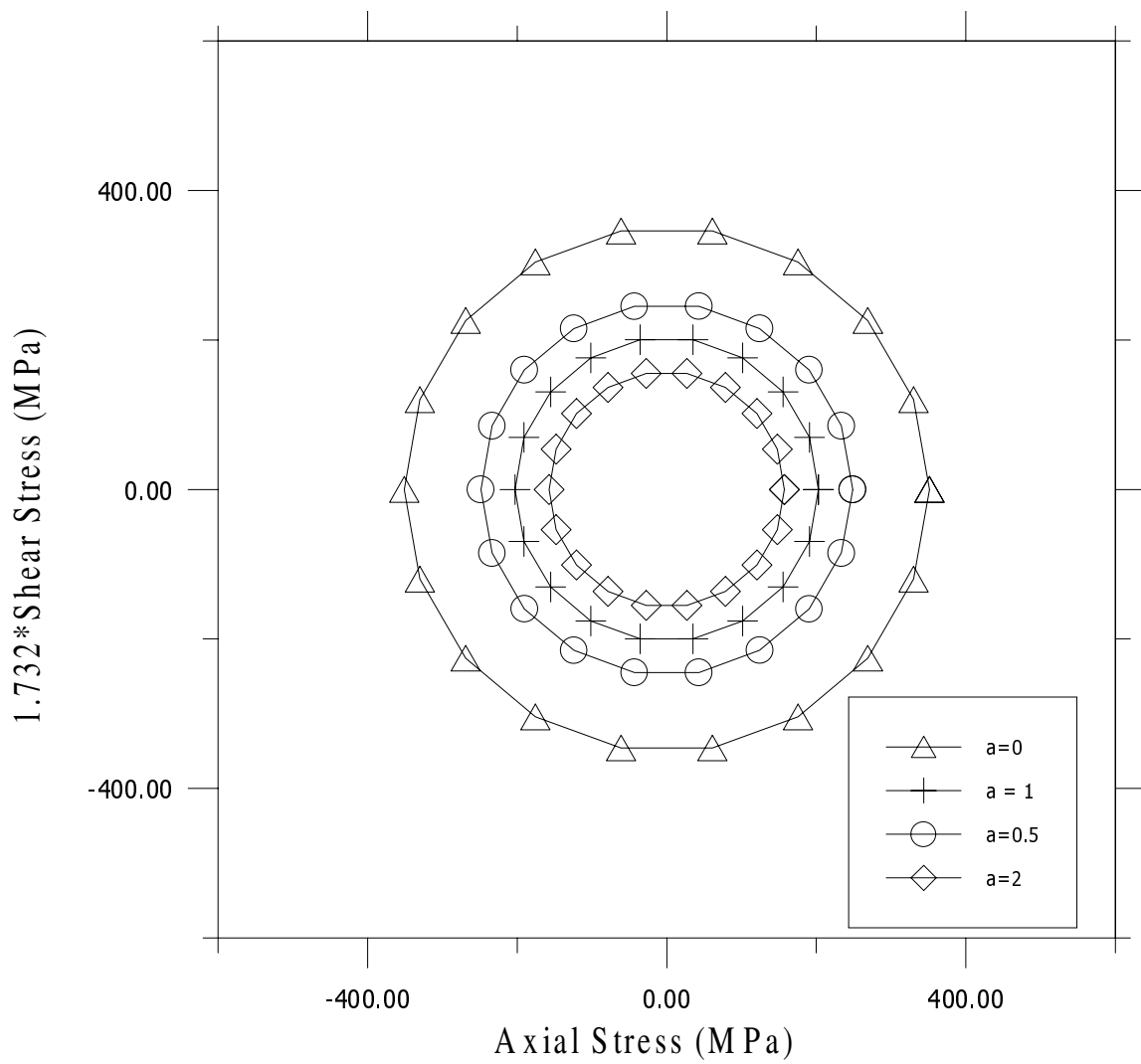
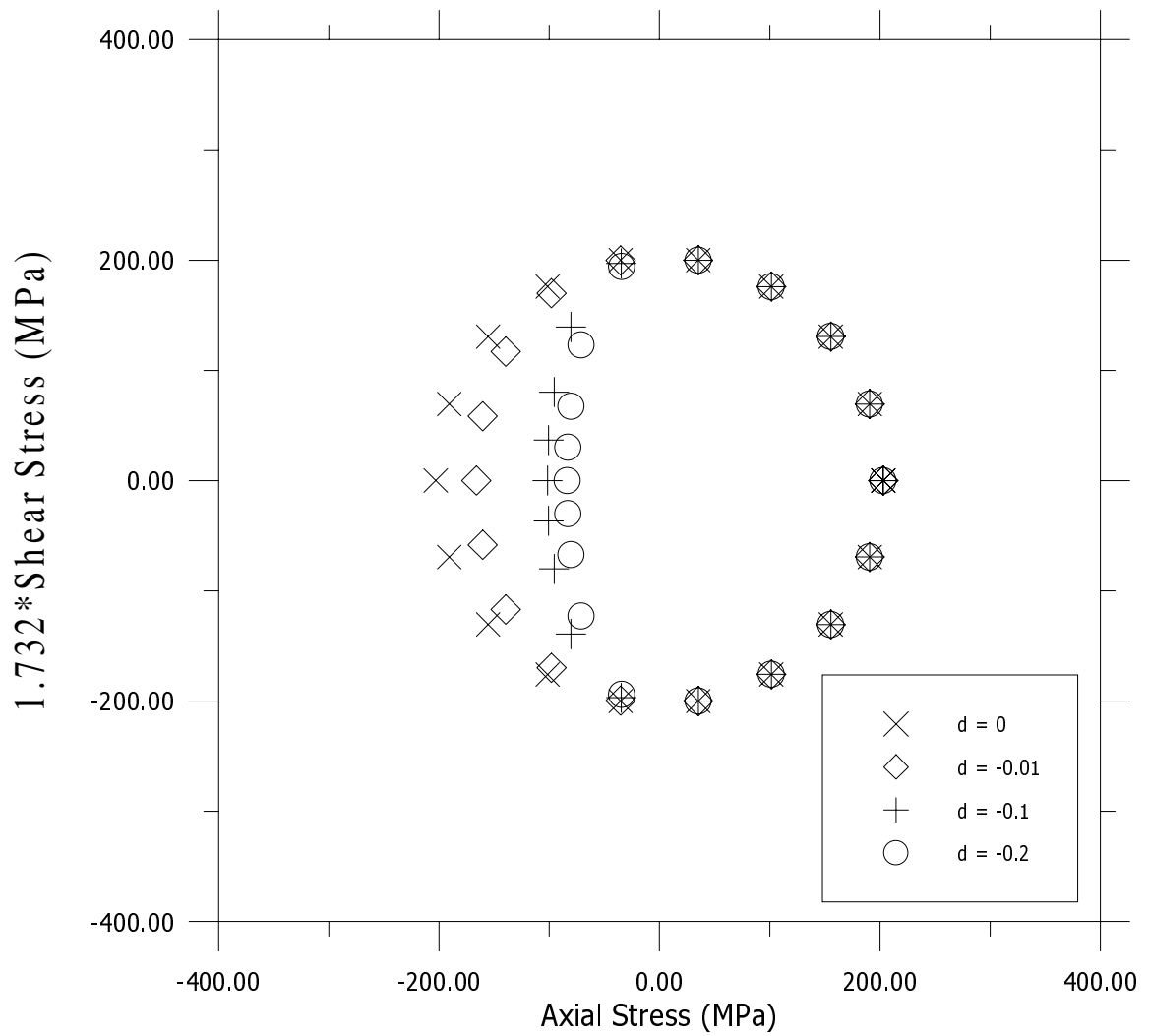**Figure 3.2:** Size change of a yield surface with changing *a*. (k_0 = 203.1 MPa)

Figure 3.3: Distortion of a yield surface with changing *d* ranging from 0.0 to –0.2. (k_0 = 203.1 MPa)
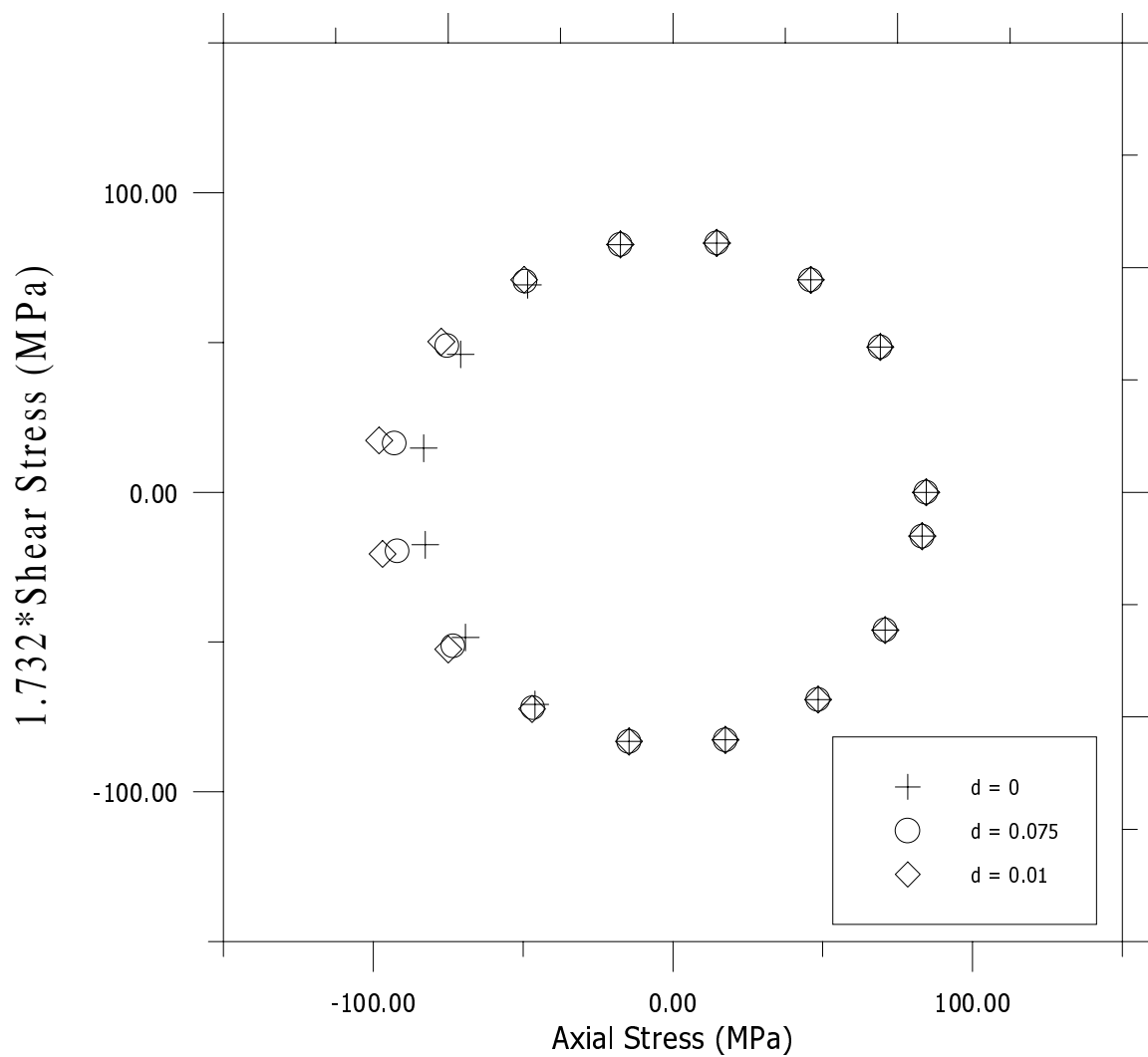
Figure 3.4: Distortion of a yield surface with changing *d* ranging from 0.0 to 0.01. (k_0 = 84.4 MPa)

Chapter 4

Results and Discussion

With the amount of experimental data collected it is important that the results be presented in a concise manner. It was decided that the data should be given in a format that handled each strain path separately. This allows for comparison between the three materials for each strain path. Section 4.1 will first introduce some of the experimental yield surface data. Each section from there will briefly discuss the behavior of each material for a given load path and then show summary plots of the evolution of the primary variables. The variables of interest are a, d, α_{11}, and α_{12} because these are the four parameters that describe the yield surface in the Voyiadjis distortion model. After the three primary strain paths are discussed the additional paths applied to IN 718 will be discussed. Note, this section does not try to present all of the yield surface data collected. An entire set of the data and model fits can be found in Appendix A.

4.1 Yield Surface Data

All yield surface tests revolve around the ability to obtain individual yield points from each probing direction. Therefore, it is appropriate to show details of at least one yield probe. Figure 4.1 shows (a) the stress-strain response and (b), the offset strain-total strain response of a 12° yield probe for HN 188. From Figure 4.1 (a) the small offset strain is visible from the separation between the loading and unloading lines of the stress-strain curve. Furthermore, Figure 4.1 (b) shows that the offset strain reached a value of

31.6, slightly overshooting the target of 30. This discrepancy is acceptable and does not constitute a large deviation from the target. In addition, Figure 4.1 (b) shows that the offset value slightly decreases during the unloading of the probe. This decrease can be contributed to vicoplasticity effects due to the elevated temperature of the testing. It could also be the result of a slightly nonlinear elastic stress-strain response.

The first step for all yield surface evolution tests was determining the initial yield surface. The initial yield surface was assumed to be circular in the σ_{11}-$\sqrt{3}*\sigma_{12}$ stress plane. Therefore, each initial yield surface was regressed to a circle by setting the directional unit tensor, υ_{ij}, in the Voyiadjis model equal to zero. This caused the distortion portion of the model to go to zero and produce a circular yield surface. Figure 4.2 shows an initial yield surface and model prediction for SS316, Path I. In this figure there is one yield point that falls well inside of the fitted surface. This is typical of the experimental scatter inherent to this study.

Each of the three materials has considerably different initial yield surfaces. All three have different radii and the initial yield surface for IN 718 is translated in the compressive direction due to its strength differential. More information on the strength differential in IN 718 and other materials can be found in Gil [46] and Hirth and Cohen [46]. Figure 4.3 presents the average yield surface fit for all of the specimens tested. The difference in initial yield strengths and the strength differential are clearly visible.

Different types of subsequent yield surfaces were produced for each of the six prestrain directions included in paths I-III. Figures 4.4-4.6 shows subsequent yield surfaces for each of these prestrain directions for HN 188, SS 316, and IN 718, respectively.

The solid line in each figure represents the initial yield surface. From the graphs it is clear that the kinematic hardening component of the yield surfaces follow the prestrain direction. It can also be seen that the distortion is in the opposite direction of the prestrain. In addition, when compared to the initial surface each subsequent surface shows isotropic hardening. Closer inspection of the data shows that each yield surface has two distinct parts: (1) a well-defined circular front side, and (2) a poorly defined flattened backside. The front side of the surfaces encompasses the yield point within the range of ±90º from the direction of the most recent prestrain direction. The front side is also more-or-less centered with respect to the prestrain direction. Along the backside of the yield surface (approximately 90º to 270º) the curvature decreases. Significant experimental scatter in the yield points along the backside of the yield surface was typically observed. This scatter tended to increase as the specimen accumulated plastic strain as it proceeded through a given load path.

4.2 Effect of Load Path Cycling

Each load path was cycled for two or three cycles. The number of cycles was determined by when the yield surfaces stopped evolving. Each material behaved differently when the load paths were cycled, but in general, HN 188 and IN 718 required 2 cycles and the SS 316 required three cycles for cyclic hardening to stop. In fact, IN 718 stopped evolving by the end of the first cycle, but a second was conducted to confirm this. Figure 4.7 shows the cyclic evolution of the yield surfaces at selected points for HN 188, Figure 4.8 for SS 316, and Figure 4.9 for IN 718. From these figures it can be seen that the yield surfaces changed the most in the first cycle. Each consecutive cycle then

produced less hardening effects. SS 316 continued to harden through all three cycles.

HN 188 showed considerable hardening between the first and second cycles, but little

between the second and third. As a result, only Path II was carried out for three cycles

for HY 188. Path II and Path III were stopped after just two cycles. The hardening of

IN718 nearly stopped after just one cycle. The yield surfaces for cycles two virtually

overlap those for cycle one. In general, the number of cycles needed for the yield surface

evolution to stop was inversely related to the initial yield strength of the material.

4.3 Strain Path I

Strain path I was a purely axial strain path as shown in Figure 2.4 (a). Both HN

188 and IN 718 were subjected to 2 cycles of this path while SS 316 was cycled three

times. In addition, time constraints made it necessary to conduct the yield surface

determination for HN 188 and IN 718 at only points A, C, E, G, and I. (see Figure 2.4a).

Figure 4.10 (a) shows the axial strain paths produced by Path I. Only one example for

each load path is shown in Figure 4.10 because the strain paths were well controlled and

the results for all materials look identical. All cycles are shown and overlap. Figure 4.11

provides the axial stress-axial strain response of each material for Path I. It clearly shows

the relative amount of isotropic hardening each material exhibits. Both HY 188 and SS

316 show a continuous increase in the maximum stress while IN 718 quickly reaches a

maximum value. Of primary concern in this section is the evolution of the parameters

for the Voyiadjis model. The parameters are shown in Figure 4.12-4.14. The data is

presented in the order of the yield surface determinations along the load path. From

Figures 4.13 it can be seen that SS 316 has the most isotropic hardening because it has

the largest change in the parameter *a*. SS 316 is also the only material for which *a*

becomes negative. HN 188 has the second largest change in a and IN 718 the least. For each of the three materials a decreases the most during the first cycle and then begins to level off. This mirrors the observations made about the cyclic evolution of the materials in section 4.2.

The parameter d does not have a well-defined trend. Since this term measures the distortion in the yield surface it is greatly influenced by the scatter in the data for the backsides of the yield surfaces. The most well behaved test, from the standpoint of the distortion parameter, d, was HY 188 Path 1 (Figure 4.12). It shows d as nearly constantly decreasing. This indicates an increase in distortion along the backside as the load path progressed. The other two materials show this through roughly the first cycle but then it becomes difficult to see a trend. Most tests included a few yield surfaces that had more distortion than those around them. These yield surfaces often showed considerable experimental scatter and outliers that were not used in the fit.

The axial backstress component, α_{11}, follows the same pattern as the axial stress. It starts at a value of zero for the initial yield surface for both HY 188 and SS 316. However, due to the strength differential shown by IN 719 α_{11} has a value of -145 MPa for the initial yield surface. After the initial yield surface, α_{11} takes on the same sign as the maximum axial stress obtained during the prestrain prior to a given subsequent yield surface. In addition, α_{11} increased in magnitude with each consecutive prestrain in the same direction. The torsional backstress component, α_{12}, is not shown for Path I because it does not evolve during the load path.

It is worth discussing here that IN 718 showed considerably more data scatter than the other materials. The additional scatter did affect the quality of the fits that were

obtained. For some of the IN 718 yield surfaces the front side contained scatter as well as the backside. Several attempts were made during testing to eliminate this problem. The yield surfaces for IN 718 were run at considerably lower stress rates than the other materials (see Table 2.4 for rates). This did reduce the scatter somewhat, but it is present in all IN 718 yield surfaces.

4.4 Strain Path II

Strain Path II is pure shear and is shown in Figure 2.4 (b). IN 718 was subjected to two cycles of this strain path while HN 188 and SS 316 were tested for three. Again, IN 718 was tested only at every other point shown in Figure 2.4 (b). Figure 4.10 (b) shows an example of the axial strain-shear strain response for this load path. The shear stress-shear strain response for each material is shown in Figure 4.15. Figures 4.16-4.18 show the evolution graphs for the Voyiadjis model parameters for HY 188, SS 316, and IN 718 respectively.

In general, the same observations for the evolution of the parameters a and d were found for Path II as Path I. Parameter a again decreased as the strain path proceeded with the same relative changes between materials as seen with Path I. The evolution of a for HN 188 showed more scatter than for Path 1. The distortion parameter again provided no definite trend. It again decreased at the start of the load path and then became scattered in later cycles.

Path II involved the evolution of the torsional backstress component, α_{12}. It followed the shear stress as α_{11} followed the axial stress for Path I. The axial backstress component did not evolve during this load path, but for IN 718 it had a non-zero value for

the entire test. This is again a manifestation of the strength differential of IN 718. The axial backstress maintained a constant value of –145 MPa.

4.5 Strain Path III

Unlike Path I and Path II, Path III subjects the test specimen to a nonproportional loading. Points B and F follow prestrains at 45 degrees and point D follows a prestrain at 315 degrees (see Figure 2.4(c)). The axial strain-shear strain response is shown in Figure 4.10 (c). Both the axial stress-shear strain and shear stress-shear strain graphs are shown for each material in Figure 4.19. Figures 4.20-4.24 show the evolution graphs for the Voyiadjis model parameters for HY 188, SS 316, and IN 718 respectively. Note that Figures 4.20 and 4.21 show repeats runs of Path III for HN 188 on separate specimens. In addition, Figure 4.22 shown the two runs of HN 188 overlaid on the same graph.

All four model parameters evolved during this load path.   Both *a* and *d* showed the same response as with the other load paths. The model parameter *a* decreased while *d* exhibited scatter and showed no real trend. The scatter in *d* was particularly evident with the yield surfaces at points C and E. The distortion parameter grew large at these two points. The yield surfaces for Path III showed more experimental scatter than the other load paths. This was due to the fact that Path III imparted more plastic strain on the test specimen per cycle than the other load paths.

The backstress terms both evolved for this load path. Again they closely followed the movement of their stress counterparts. The axial backstress followed the axial stress and the torsional backstress followed the torsional stress, both at a lower magnitude but with the same sign.

Unfortunately the test of Path III on IN 718 was not completed for even one cycle. The test specimen buckled during the prestrain between point D and E. This is likely due to a difference in the heat treatment of the specimen used for the test. The specimen was aged separately from the test specimens used for the other IN 718 tests. The same procedure was followed, but at a different time. For an unknown reason the specimen had a yield strength, in the virgin state, that was higher than the other IN 718 specimens. It is suspected that this increase in initial yield strength also decreased the ductility of the specimen.

4.6 Additional Inconel 718 Strain Paths

For IN 718 three additional load paths were attempted. They were created as an attempt to gain additional data from specimens needed for other studies. See Figure 2.5 for schematics of these additional strain paths. Only Path IV was successfully carried out for an entire cycle. The other two strain paths caused the specimens to buckle during prestraining. The evolution of the Voyiadjis model parameters for Path IV is shown in Figure 4.25.

4.7 Summary of Experimental Results

The materials tests provide a wide range of microstructures, compositions, and material properties. However, the evolution of the yield surface of all three materials can be described by a combination of isotropic, kinematic, and distortional hardening. Therefore, it appears that the same type of hardening laws can be used to describe each alloy. This study also has shown that distortional hardening is difficult to accurately

capture experimentally. The scatter in the backsides of the yield surfaces was relatively small for the first cycle, but became significant in later cycles. This makes it difficult to discuss the evolution of distortional hardening parameter with any confidence.   The remaining parameters, a, α_{11}, and α_{12}, are all well behaved and there is high level of confidence in the results.

4.8 Parameter Evolution

Of the four yield surface parameters in the Voyiadjis model three have regular patterns to their evolution. These are a, α_{11}, and α_{12}. As a result, it was attempted to find equations to represent this evolution.

This first parameter that was considered was a. It is clear that a decreases as the material is subjected to more plastic deformation. Therefore, it is logical to assume that it has a relationship to the plastic work where plastic work is defined as,

$$W_p = \sigma_{ij}\varepsilon_{ij}^p .$$
(4.1)

When a was plotted versus plastic work the relationship proved to be of an exponential nature. Because a is not always positive there was a problem fitting an exponential equation to the data. To eliminate the problem the data was shifted by adding the absolute value of the largest negative value of a to the data. Figures 4.26-4.28 show the results of exponential fits for each material. For each fit all of the experimental data from each load path was used. The equations of the lines and R^2 statistics for each material are as follows,

1. HN 188

$$a = 1.185 * e^{-0.0404Wp} \qquad R^2 = 0.421$$
(4.2)

2. SS 316

$$a = 1.021 * e^{-0.0555Wp} \qquad R^2 = 0.465 \qquad\qquad \textbf{(4.3)}$$

3. IN 718

$$a = 0.7664 * e^{-0.0155Wp} \qquad R^2 = 0.7340 \qquad\qquad \textbf{(4.4)}$$

The back stress parameters were more difficult to fit to evolution equations. This was because during each load path the sign of the backstress alternated several times. As a result it was necessary to use the sign function to define the evolution of the backstress. The sign of the stress at a given point was taken while the magnitude of the backstress was related to the equivalent total strain. This relationship was used because the sign of the backstress was always the same as the stress, but its magnitude increased as total strain increased. Figures 4.29 and 4.30 show the results of this procedure for HN 188 and the evolution equations obtained are,

$$\alpha_{11} = 113.18 + 3.19Z - 0.035Z^2 + 0.00084Z^3 + 3.22 \cdot 10^{-6} Z^4 \qquad \textbf{(4.5)}$$

$$\alpha_{12} = -67.53 + 3.33Y + 0.89Y^2 - 0.0011Y^3 - 7.86 \cdot 10^{-6} Y^4 \qquad \textbf{(4.6)}$$

where,

$$Z = \sigma_{11}\varepsilon_{11}^2$$
$$Y = \sigma_{12}\varepsilon_{12}^2 \qquad\qquad \textbf{(4.7)}$$

The R^2 statistics for Equation 4.5 and 4.6 are 0.79 and 0.33 respectively.
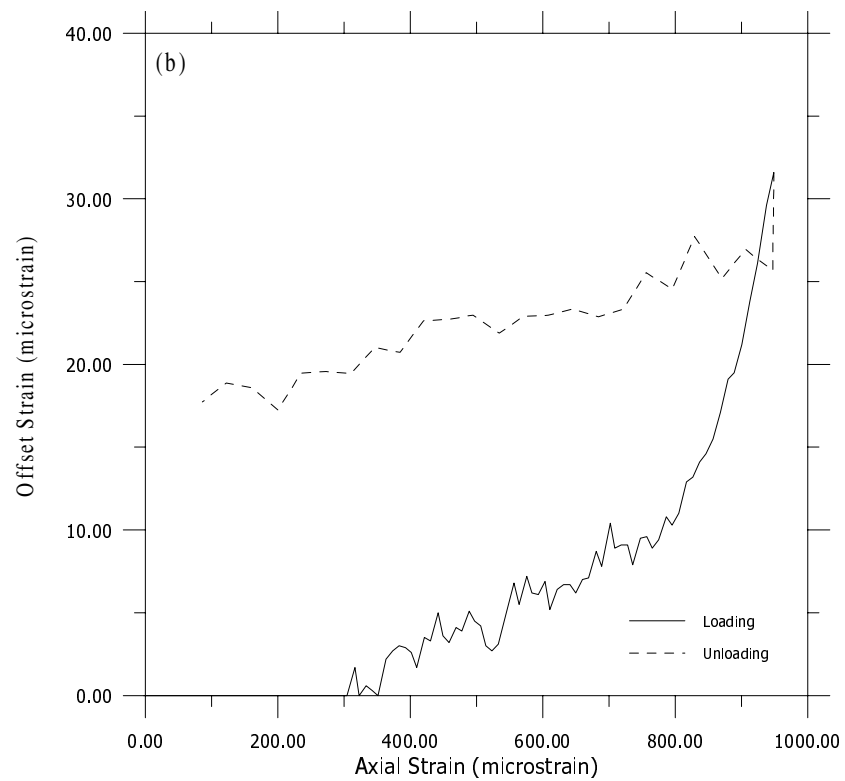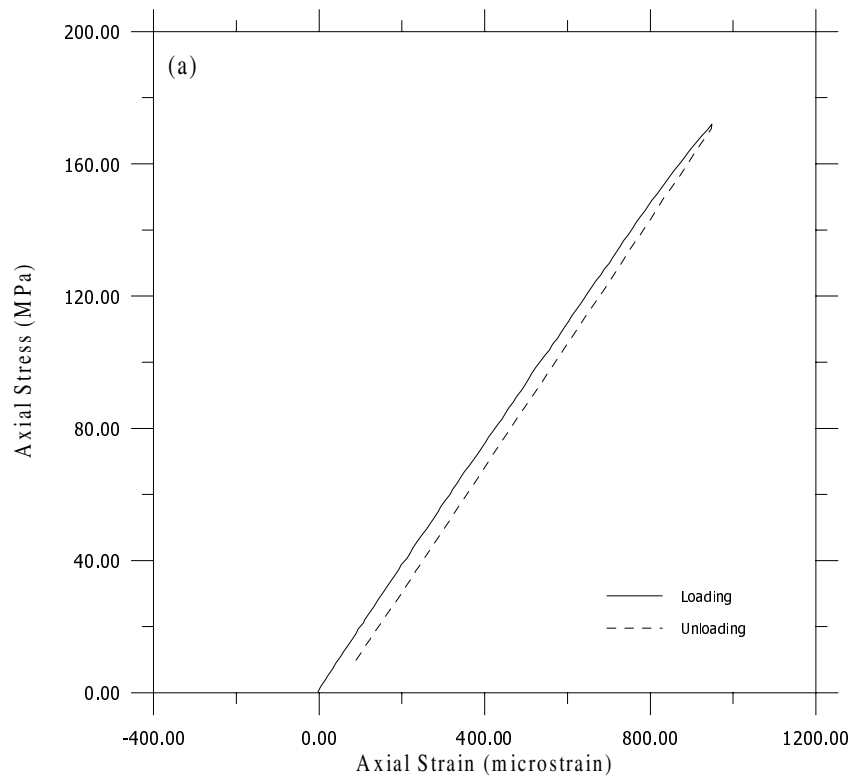
Figure 4.1: Stress-Strain, (a), and Offset Strain-Axial Strain, (b), response for an individual yield probe.
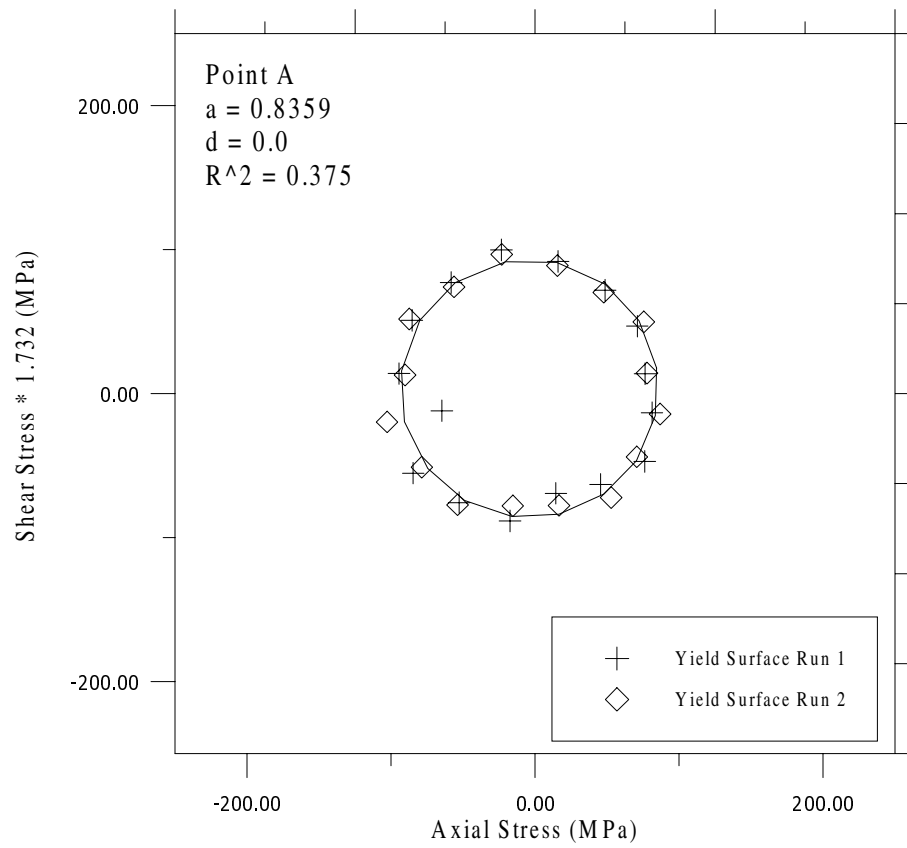
Figure 4.2: Initial yield surface for SS 316 showing model fit and parameters.
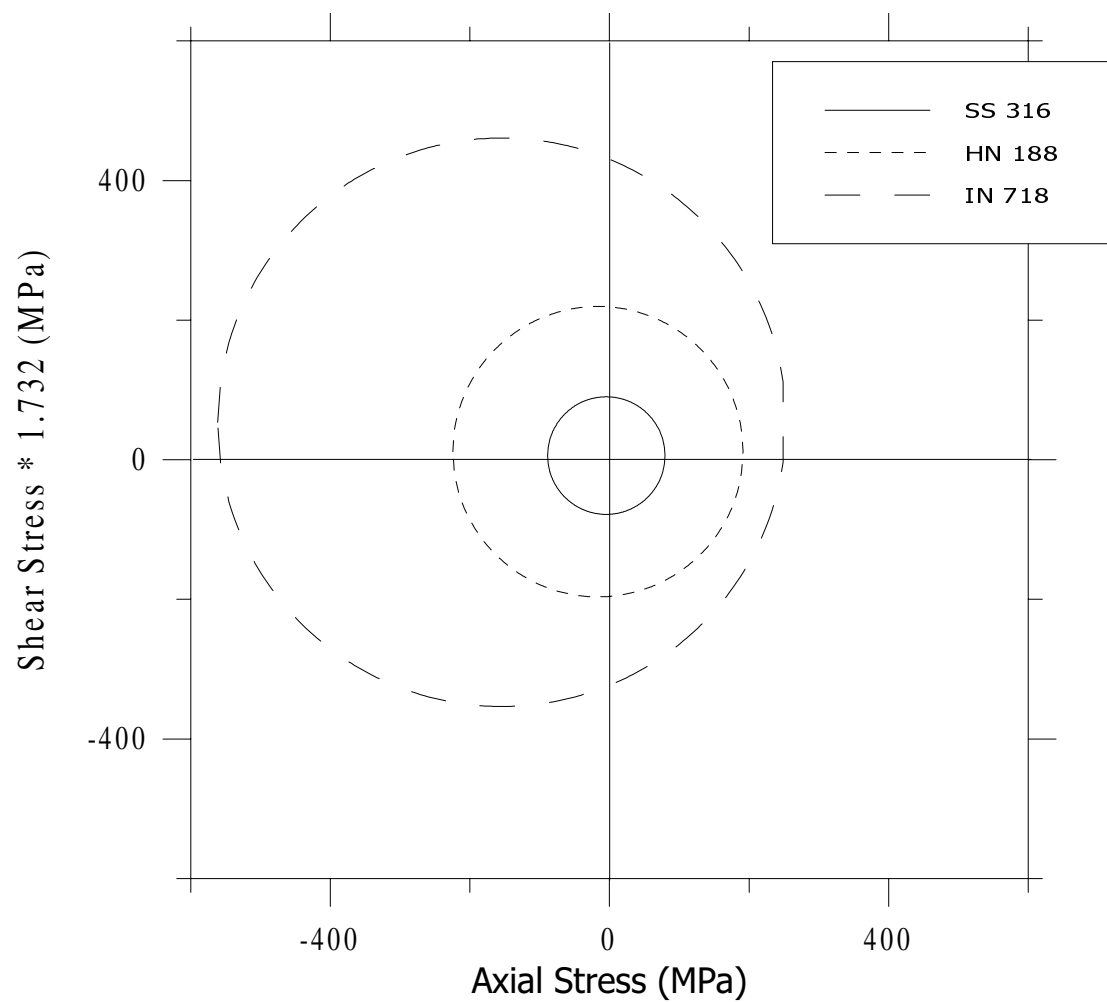
Figure 4.3: Initial yields surfaces for HN 188, SS 316, IN 718. (Averaged over all specimens tested.)
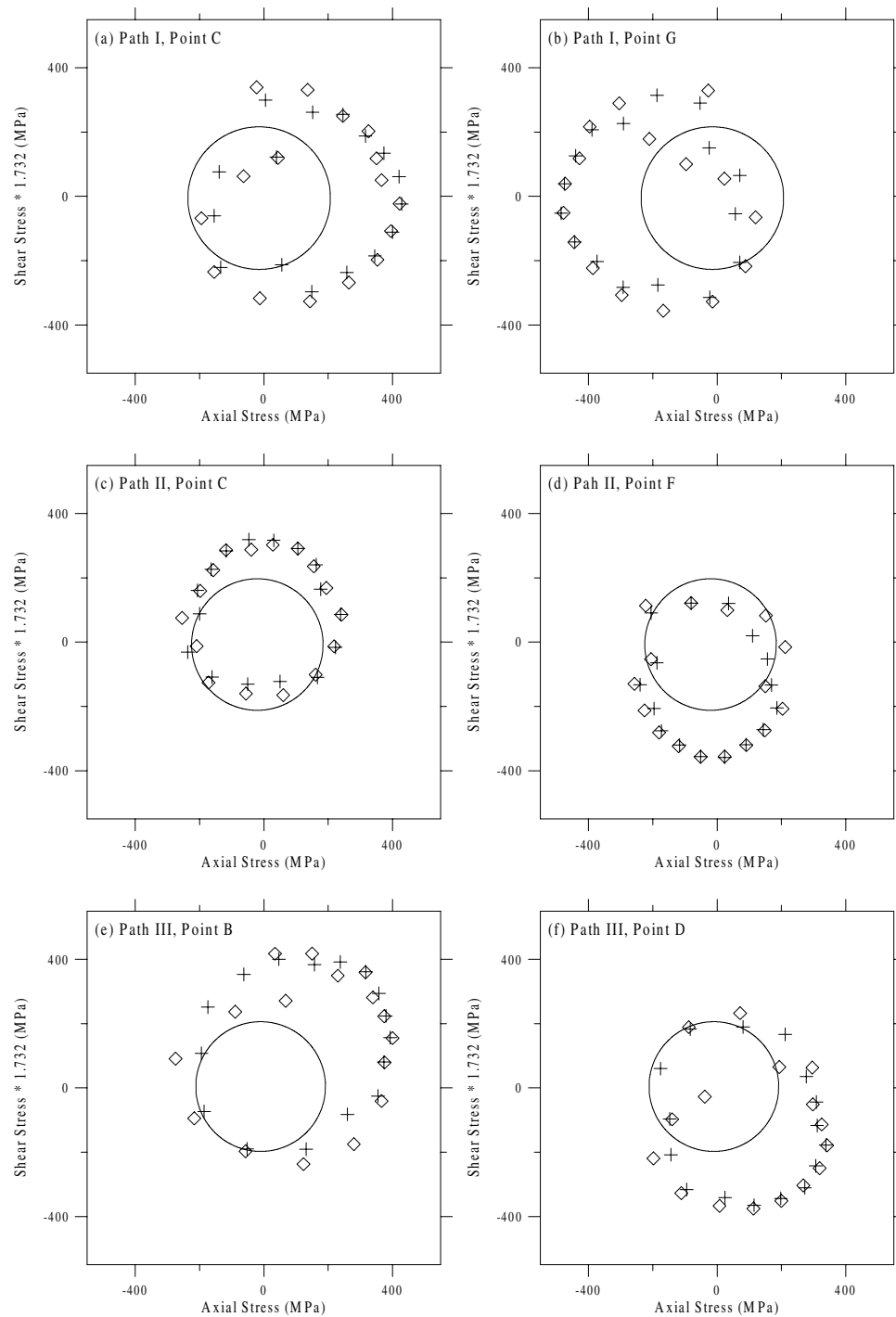
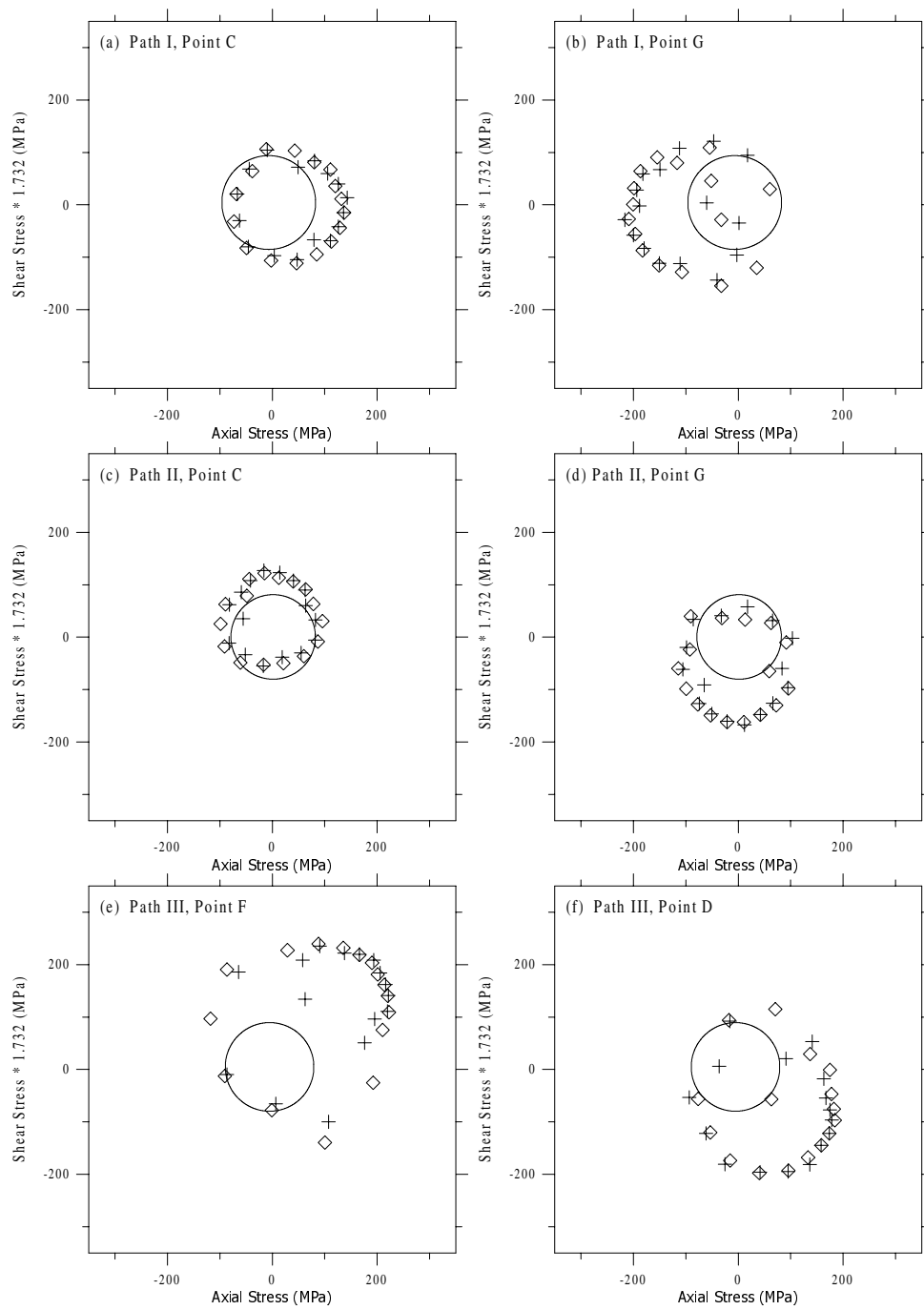**Figure 4.4:** Examples of HN 188 yield surfaces.

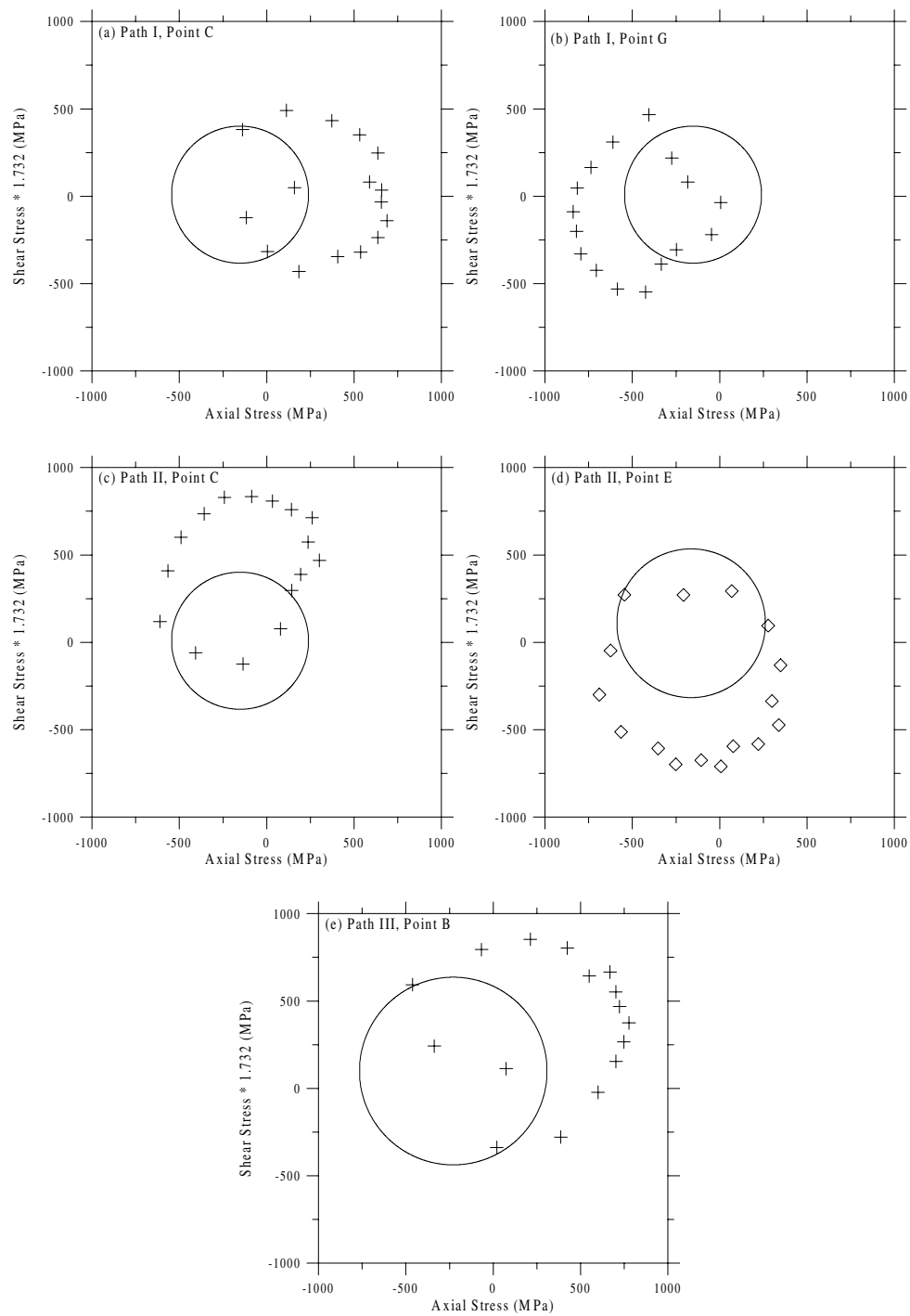**Figure 4.5:** Examples of SS 316 yield surfaces.
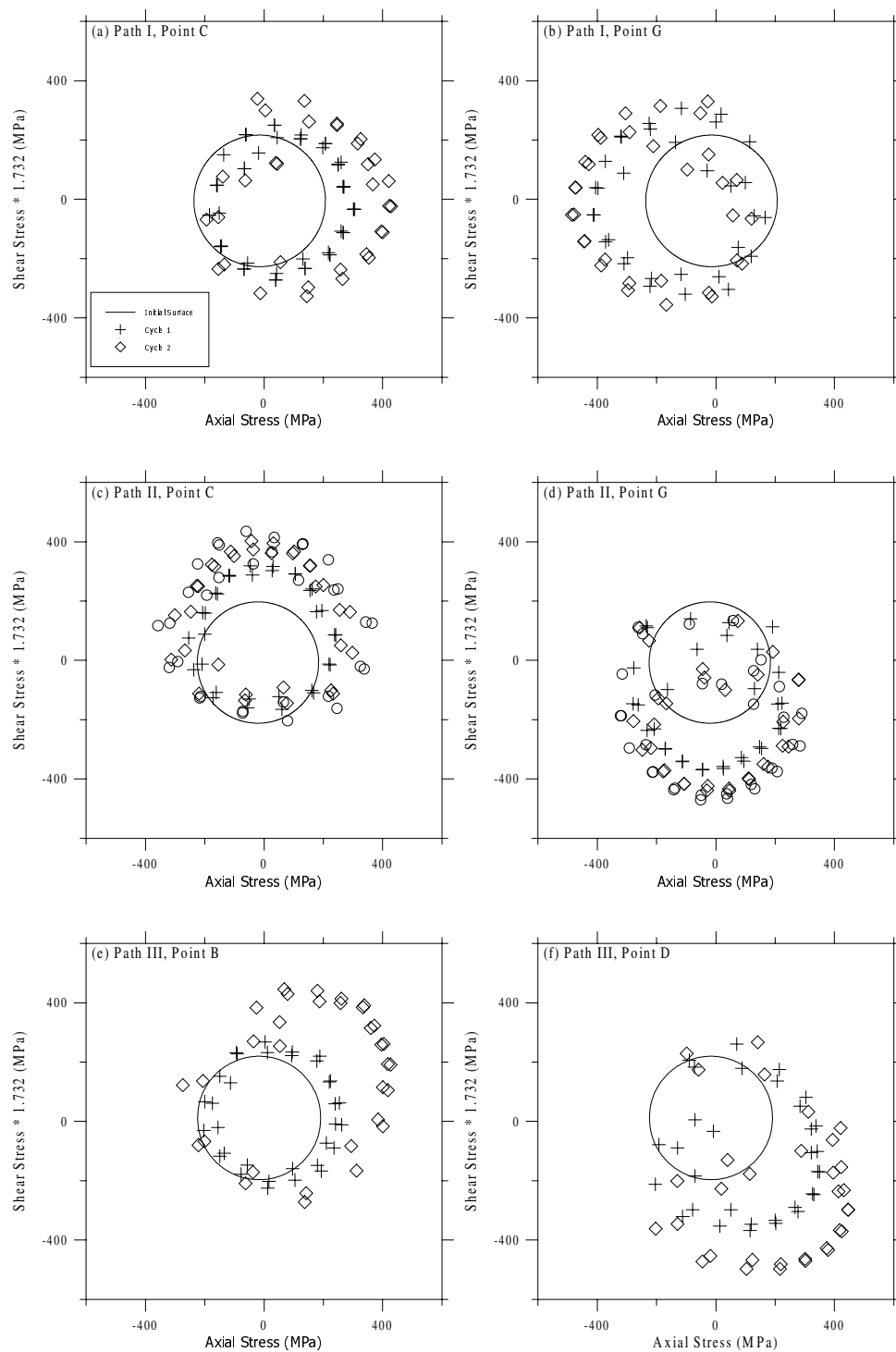
Figure 4.6: Examples of IN 718 yield surfaces.

Figure 4.7: Cyclic evolution of HN 188 at selected points.
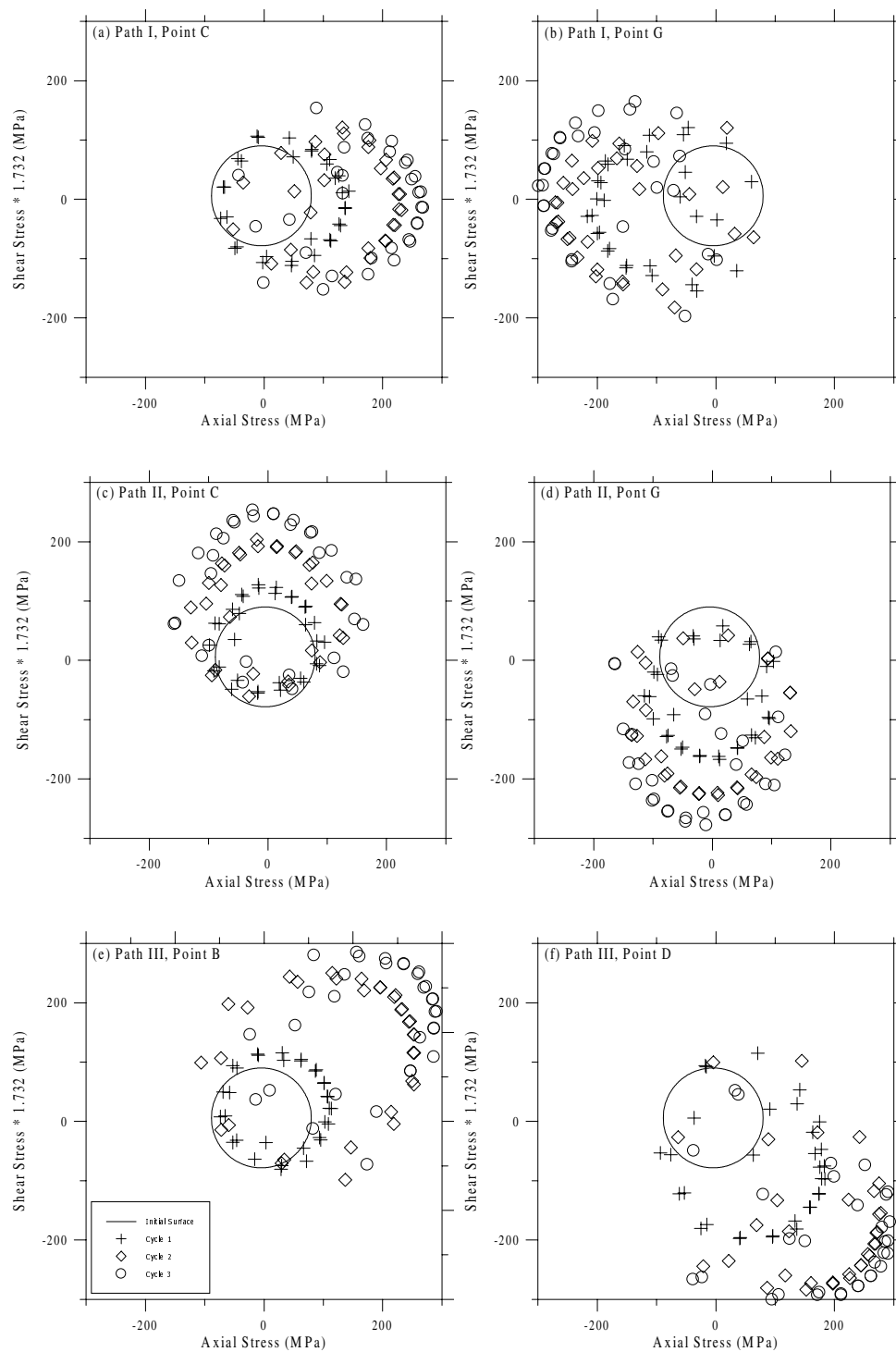
Figure 4.8: Cyclic evolution of SS 316 at selected points.
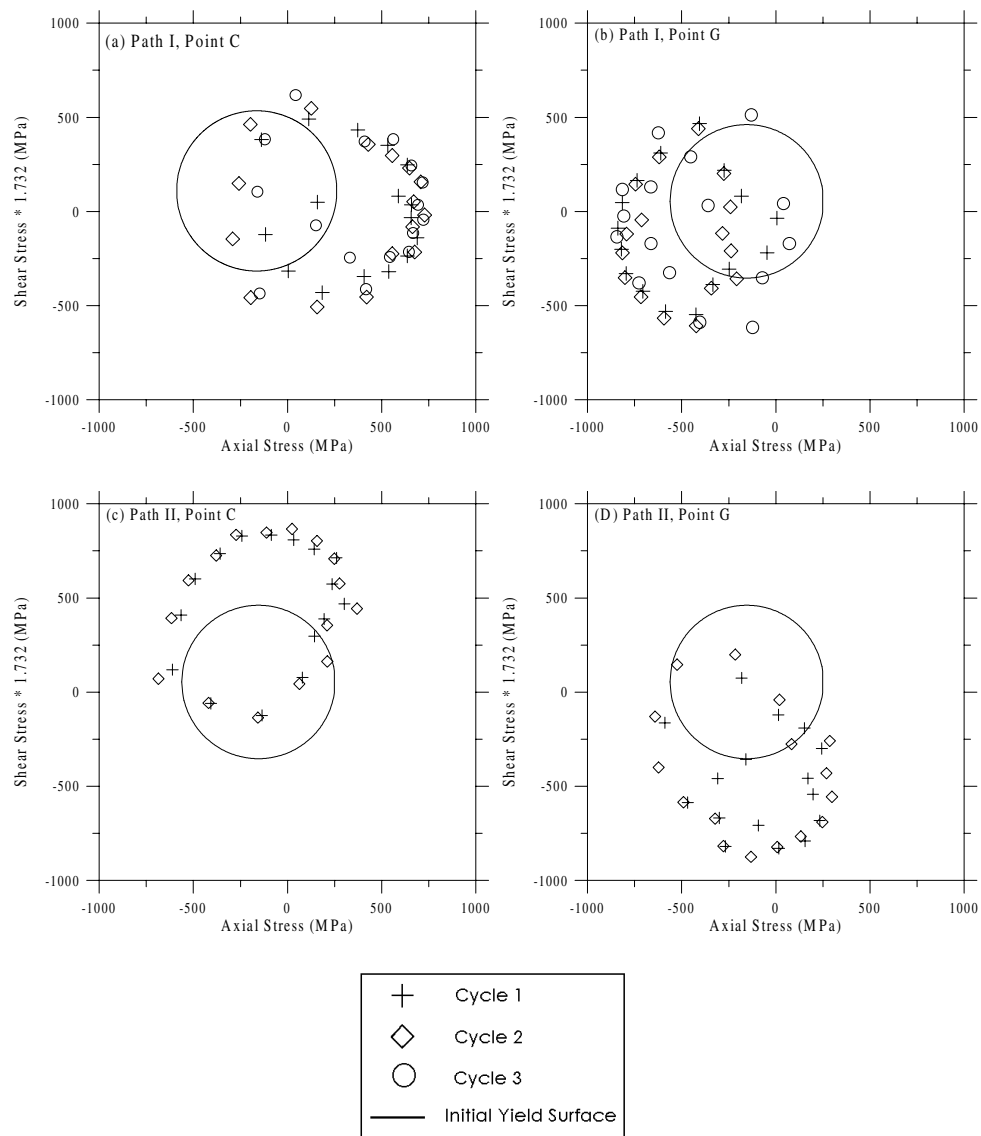
Figure 4.9: Cyclic evolution of IN 718 at selected points.
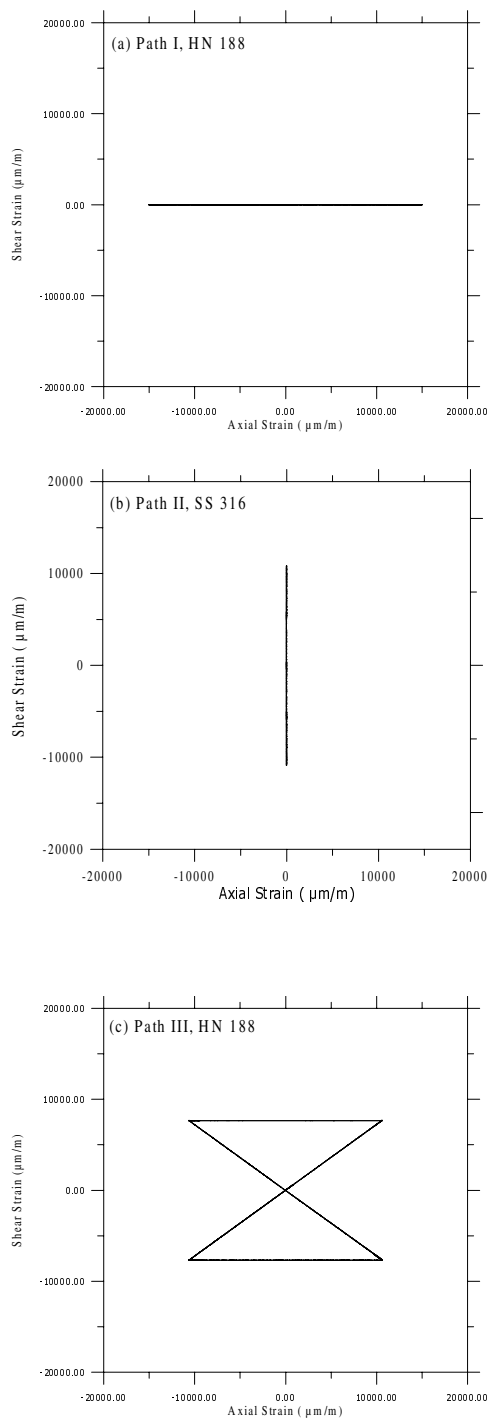
Figure 4.10: Strain paths produced by Path I, (a), Path II, (b), and Path III, (c).
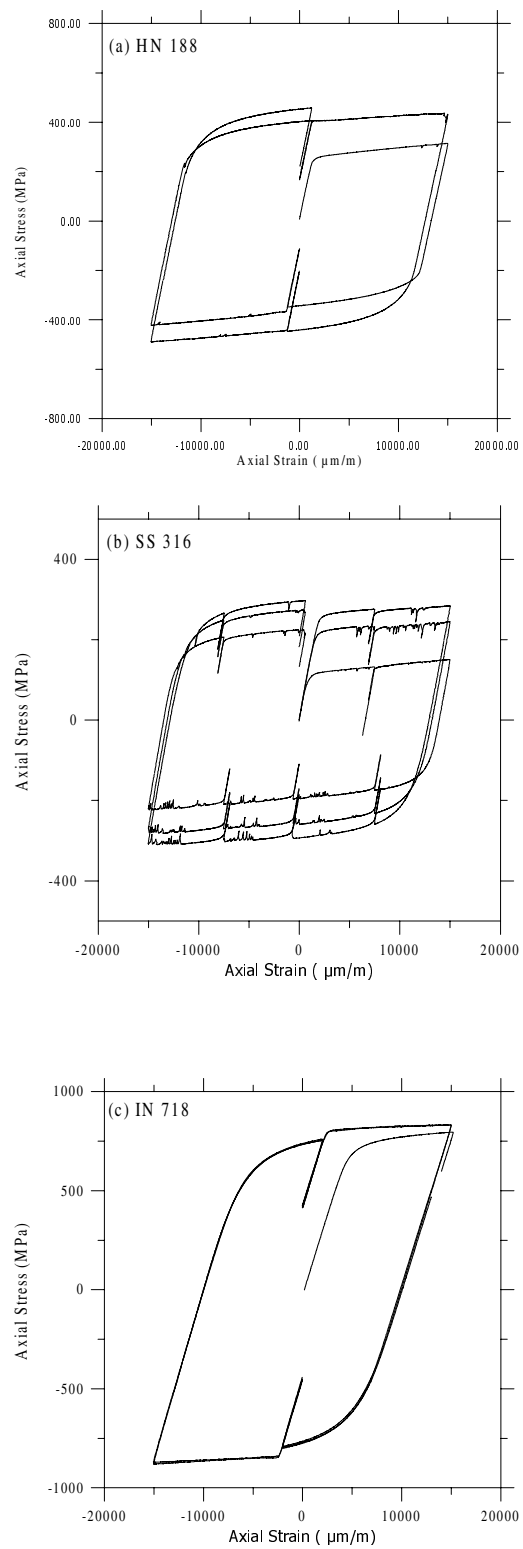
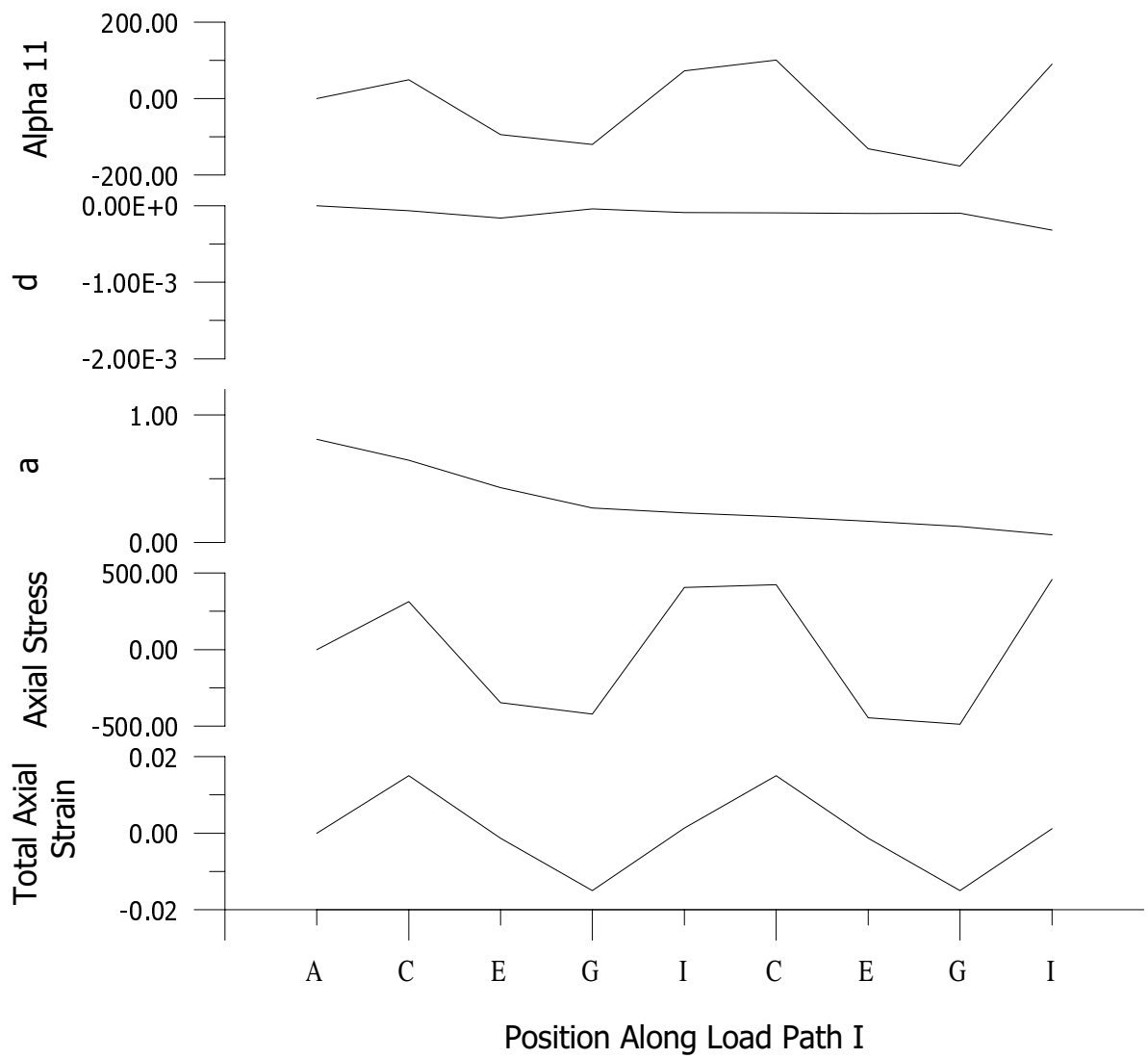**Figure 4.11:** Axial Stress-Axial Strain response for Path I.

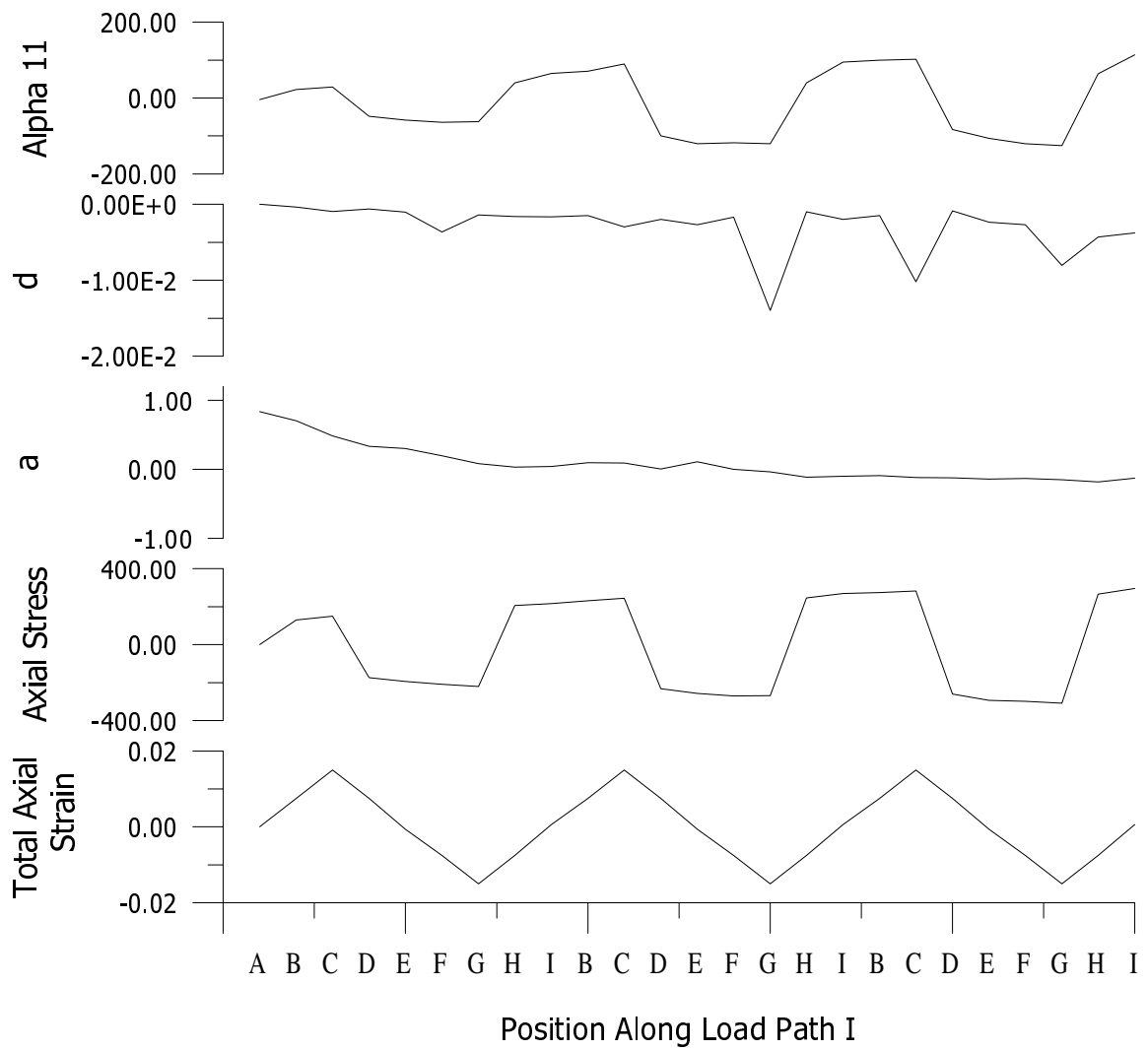**Figure 4.12:** Voyiadjis model parameter evolution for HN 188, Path I, HYII 89.

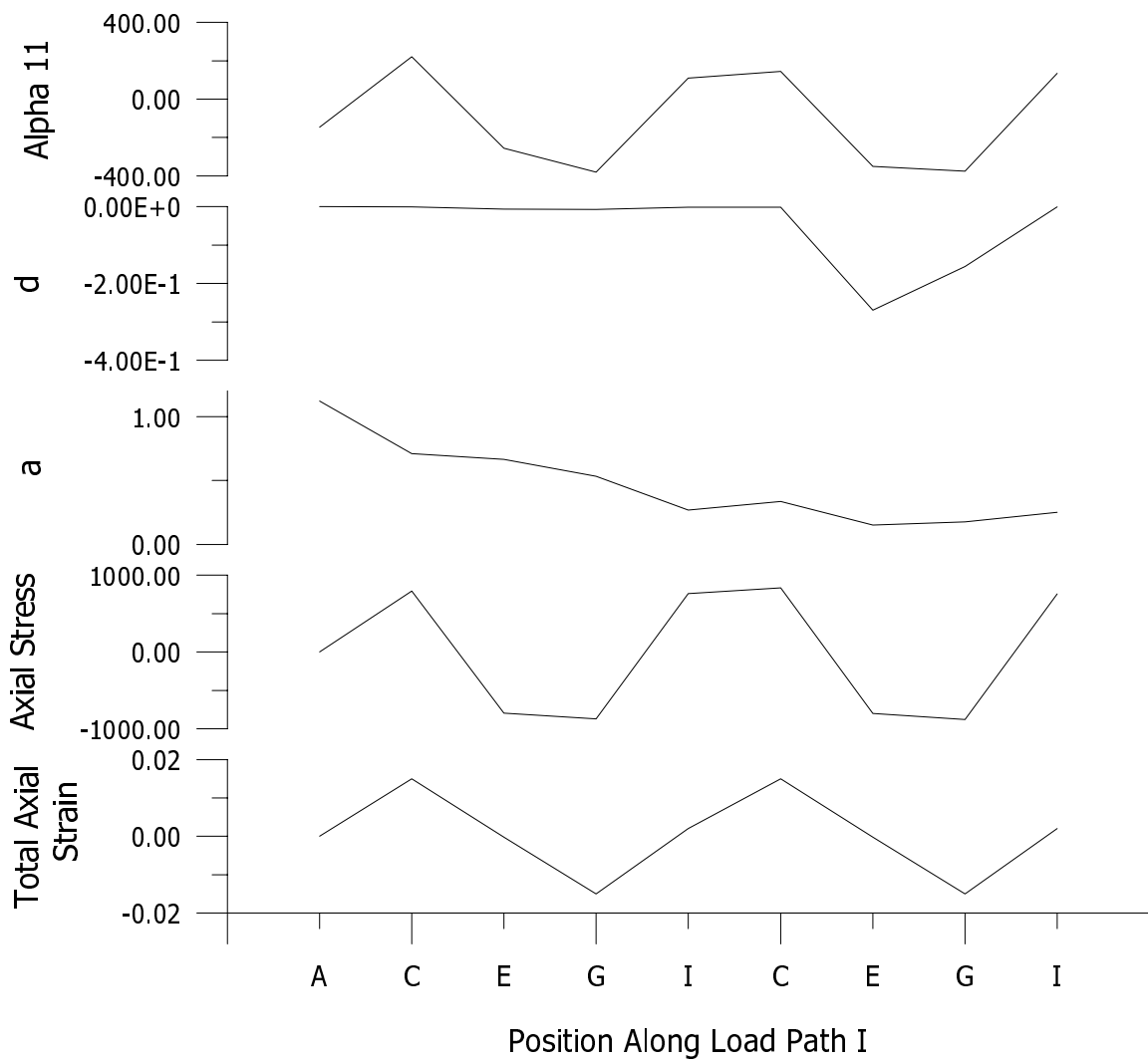**Figure 4.13:** Voyiadjis model parameter evolution for SS 316, Path I, 610-01.

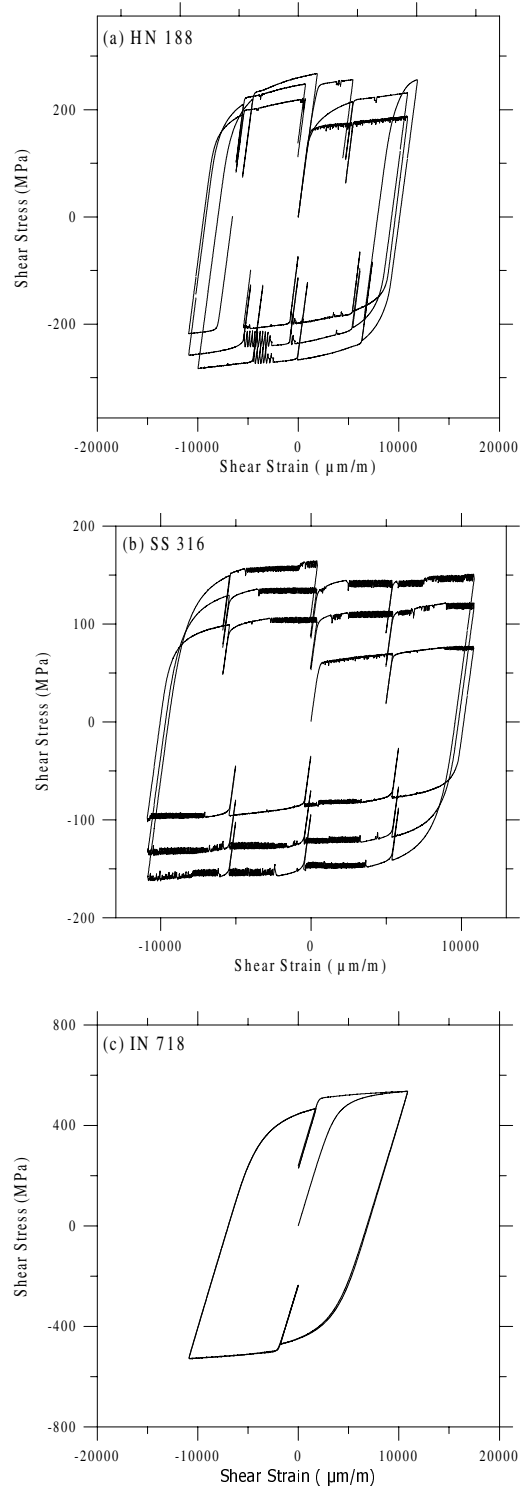**Figure 4.14:** Voyiadjis model parameter evolution for IN 718, Path I, IN-16.

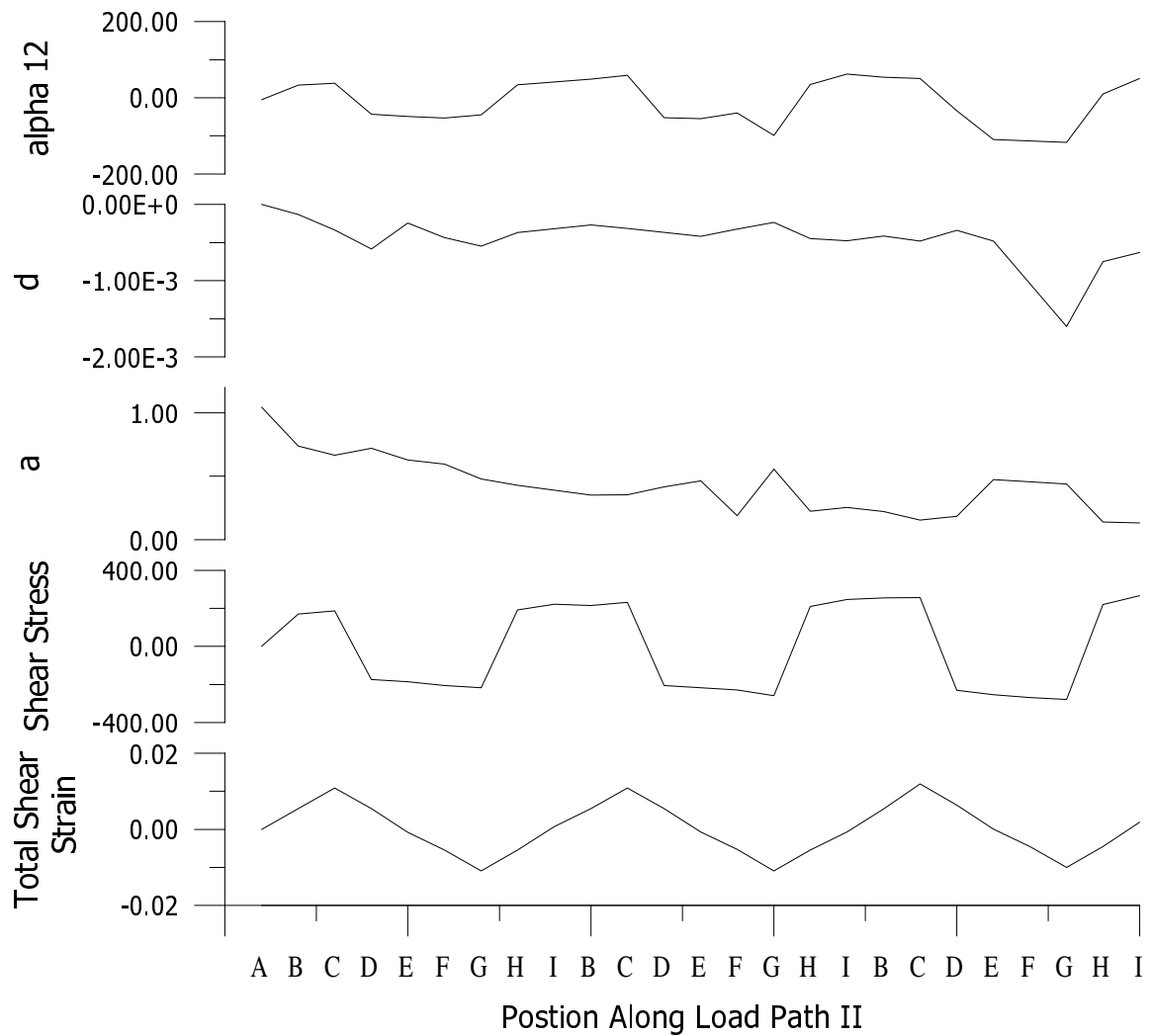**Figure 4.15:** Shear Stress-Shear Strain response for Path II.

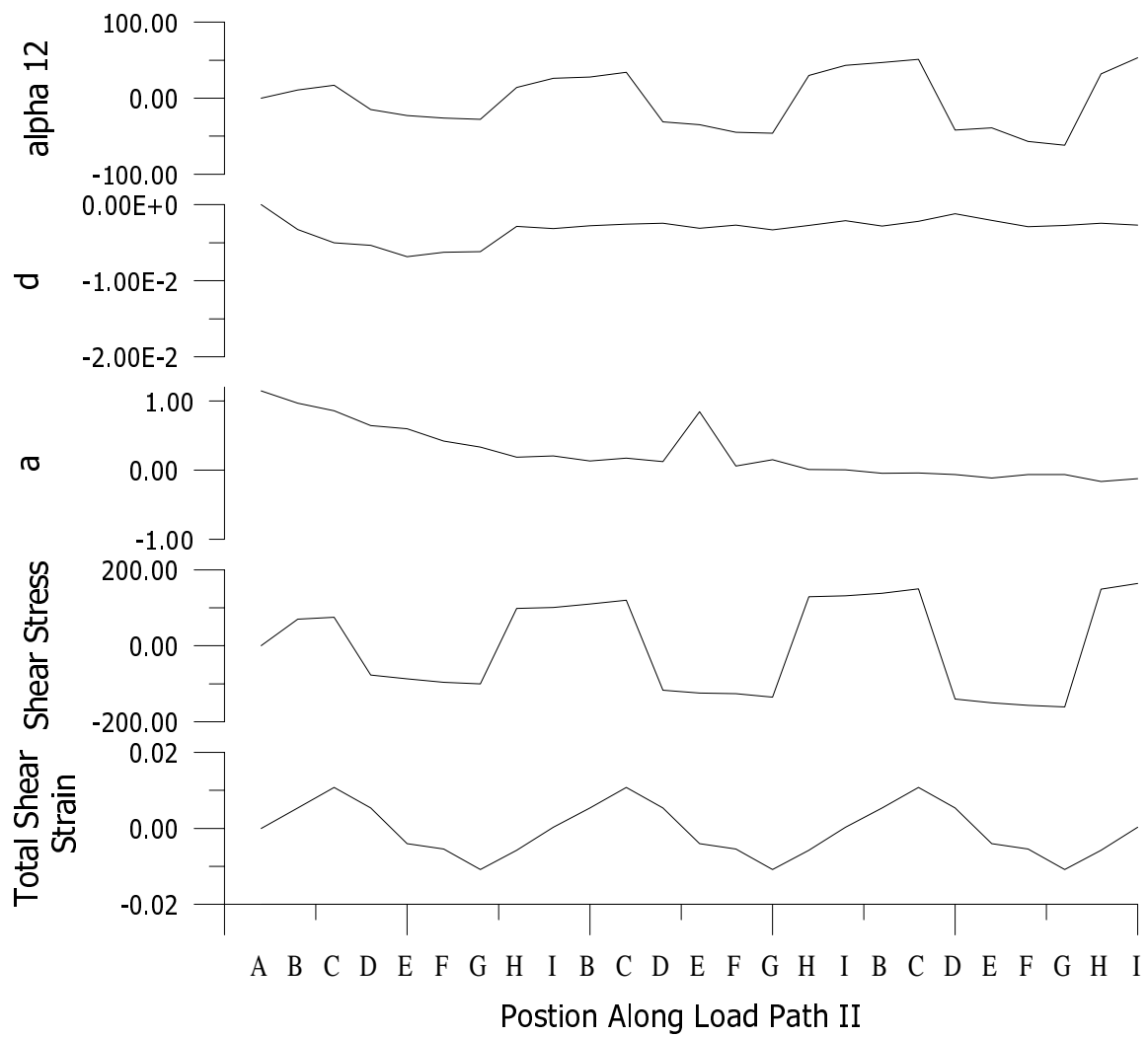**Figure 4.16:** Voyiadjis model parameter evolution for HN 188, Path II, HYII-86.

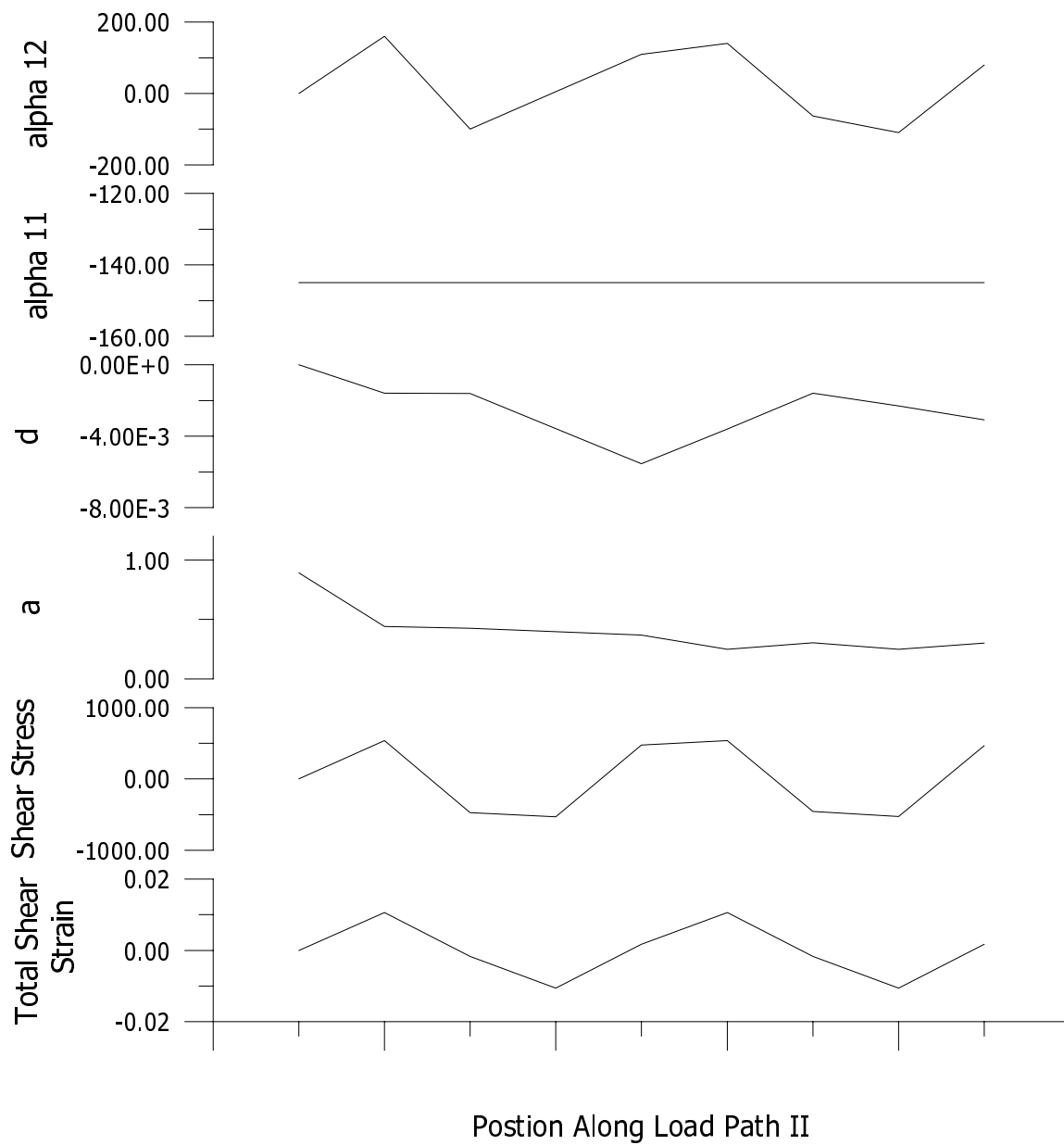**Figure 4.17:** Voyiadjis model parameter evolution for SS 316, Path II, 610-04.

Figure 4.18: Voyiadjis model parameter evolution for IN 718, Path II, IN-23.

Figure 4.19: Axial Stress-Axial Stress and Shear Stress-Shear Strain response for Path III.

Figure 4.20: Voyiadjis model parameter evolution for HN 188, Path III, HYII-90.
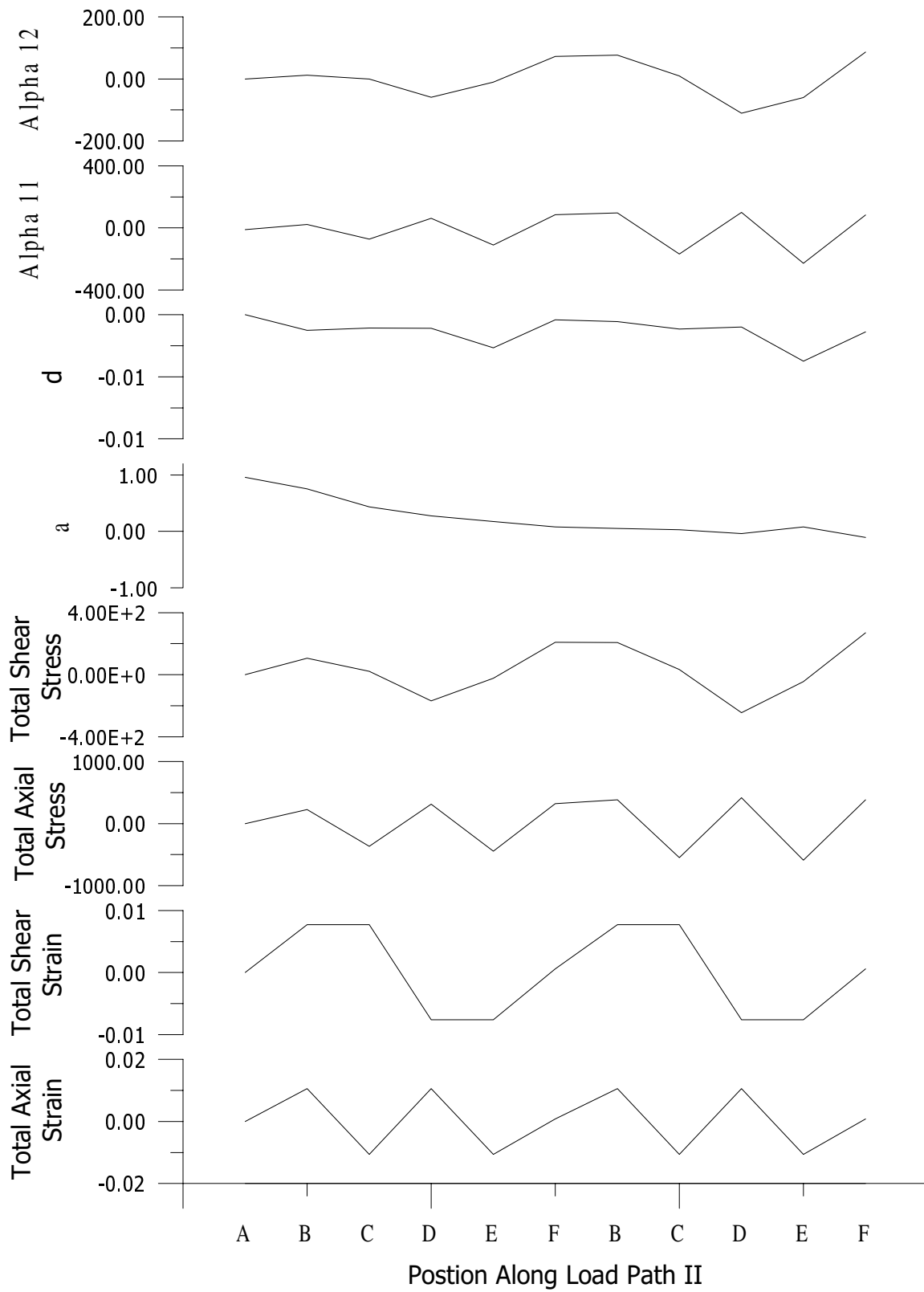
Figure 4.21: Voyiadjis model parameter evolution for HN 188, Path III, HYII-82.
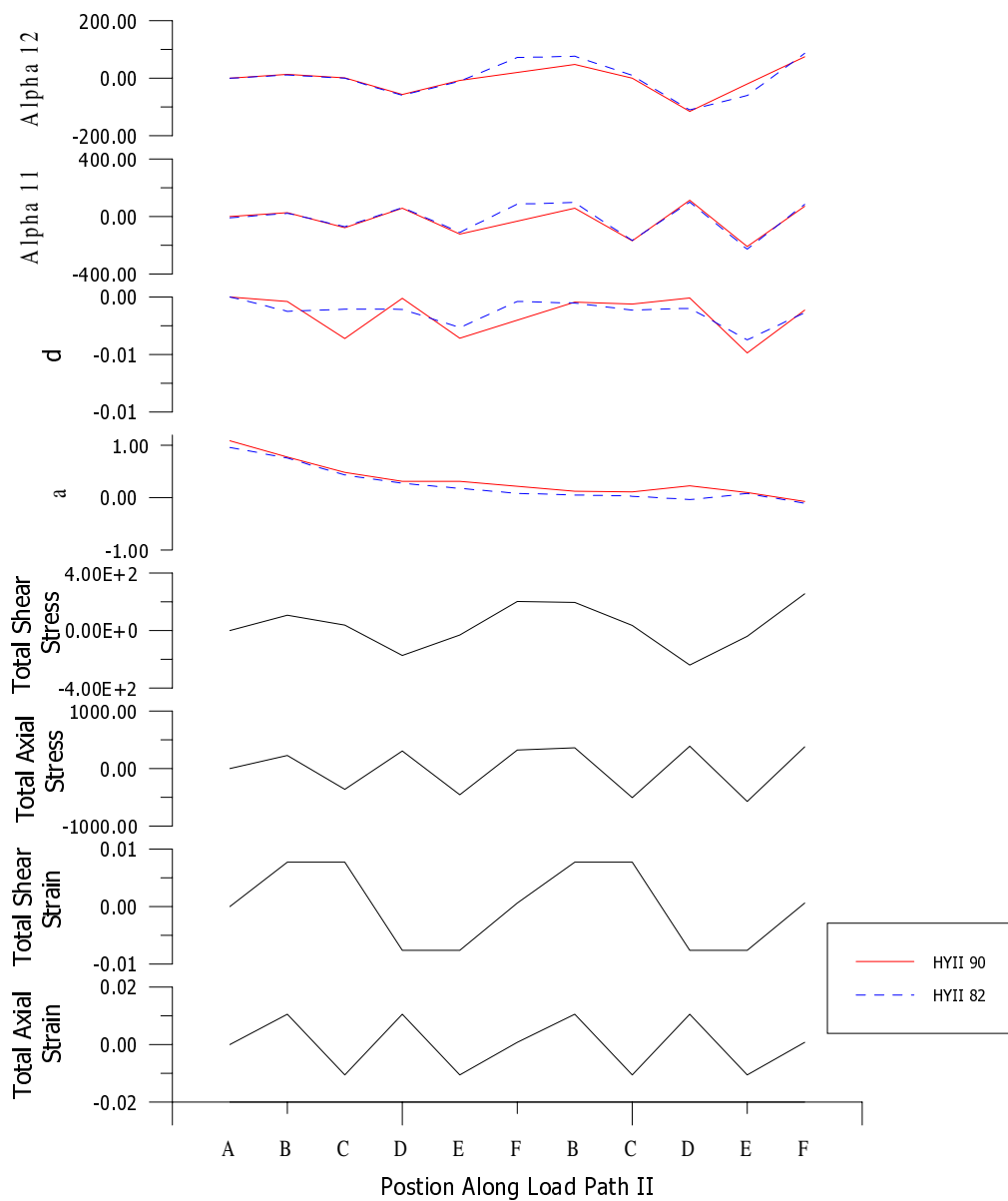
Figure 4.22: Voyiadjis model parameter evolution for HN 188, Path III for runs 1 and 2.
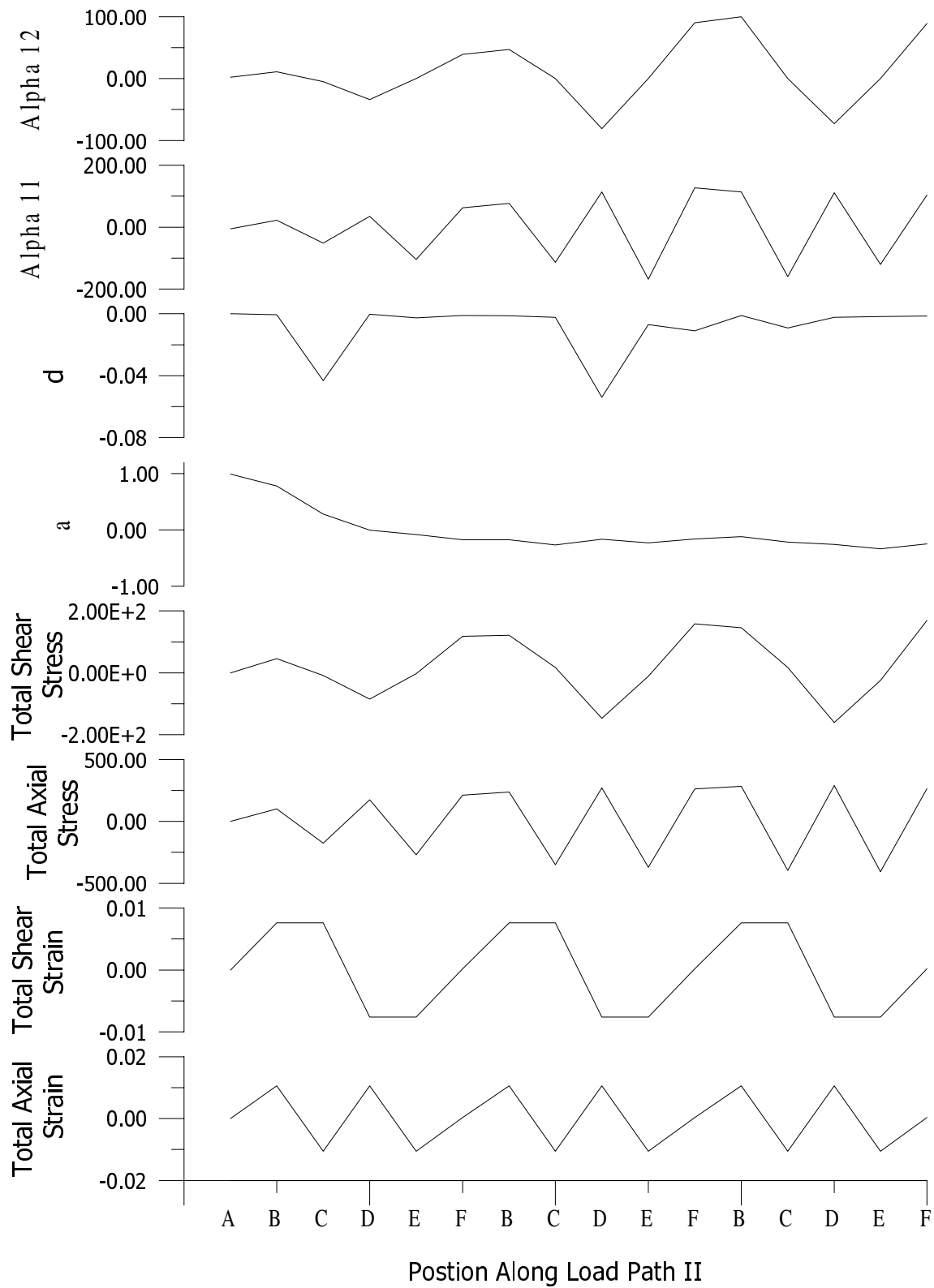
Figure 4.23: Voyiadjis model parameter evolution for SS 316, Path III, 610-05.

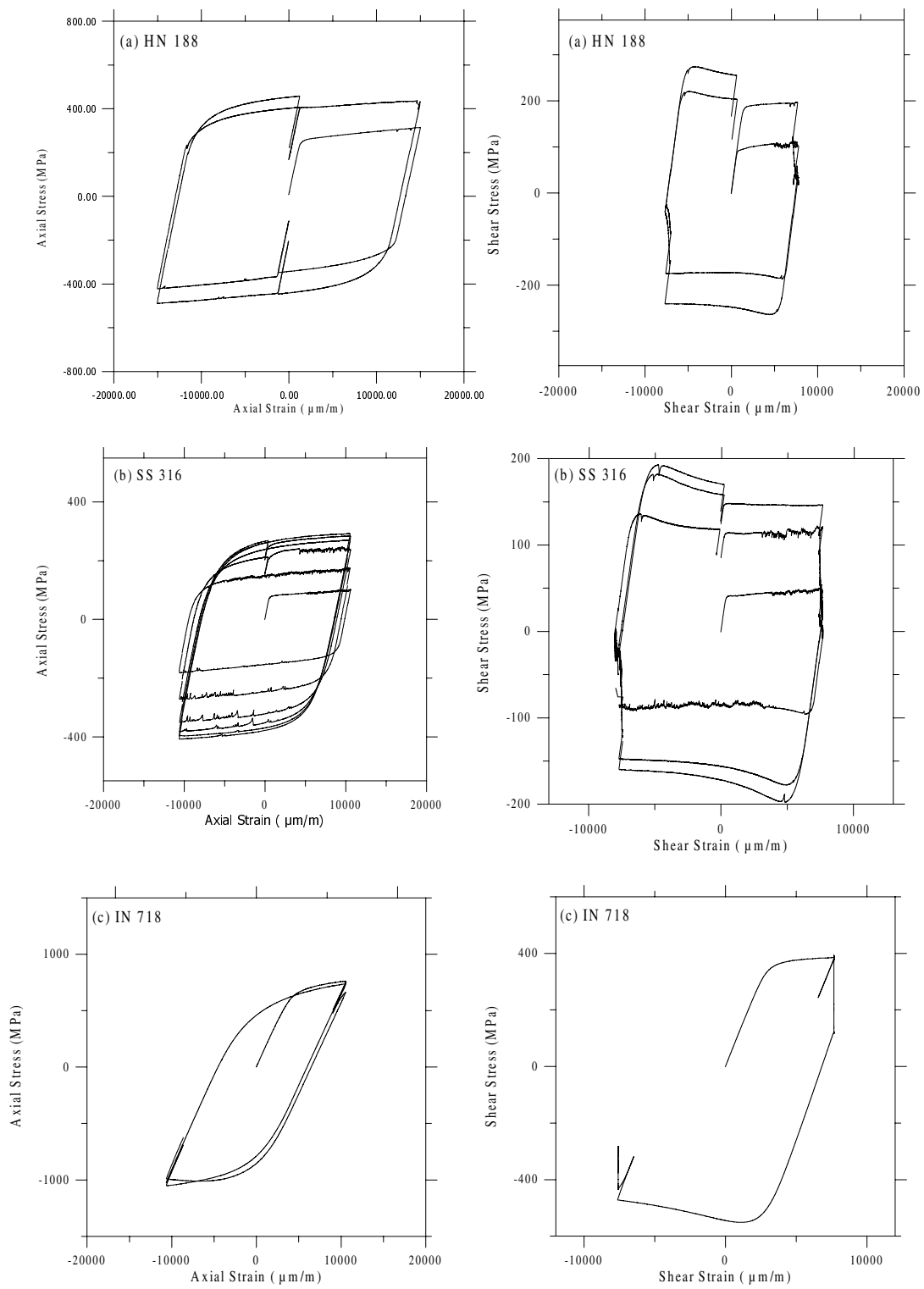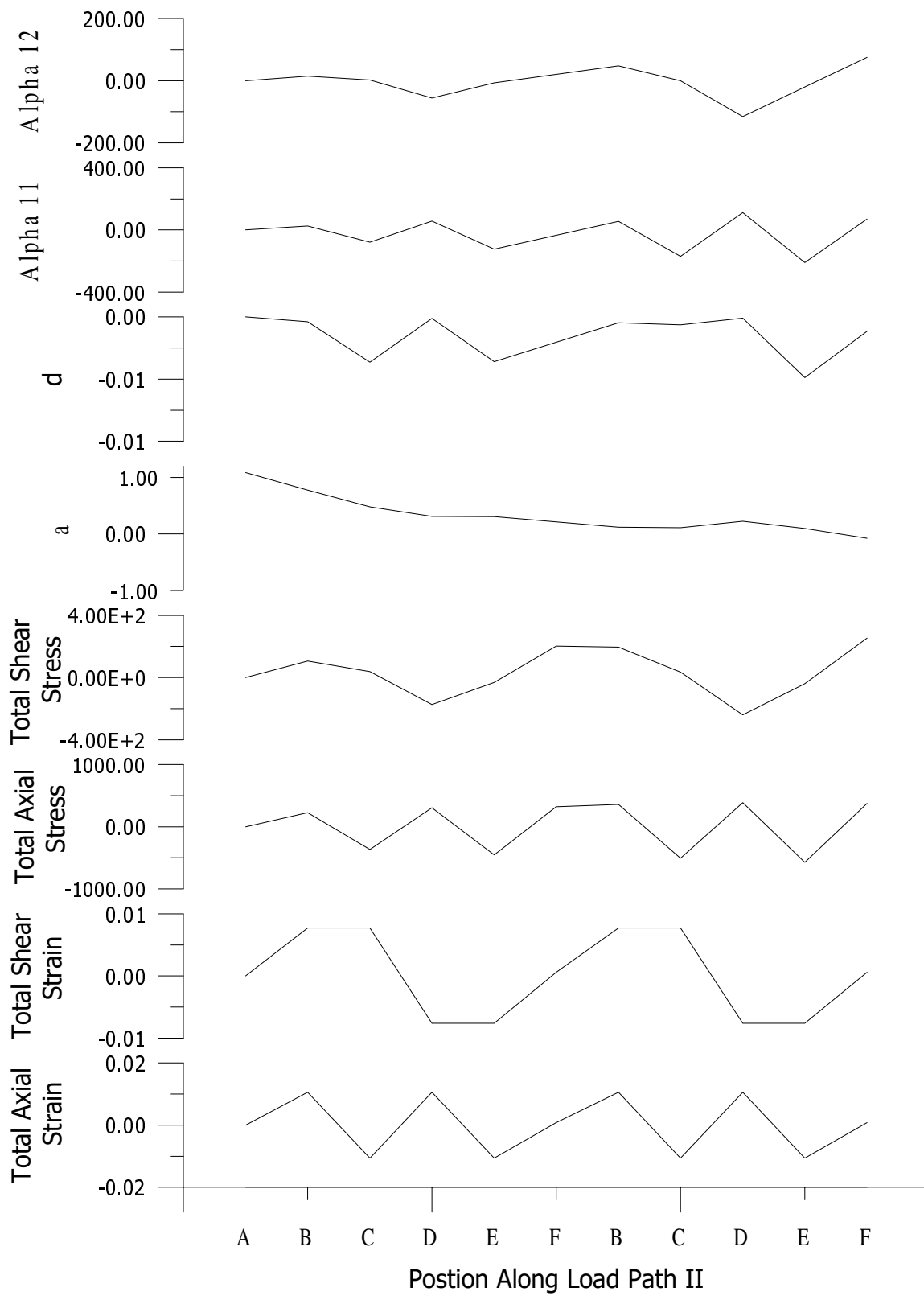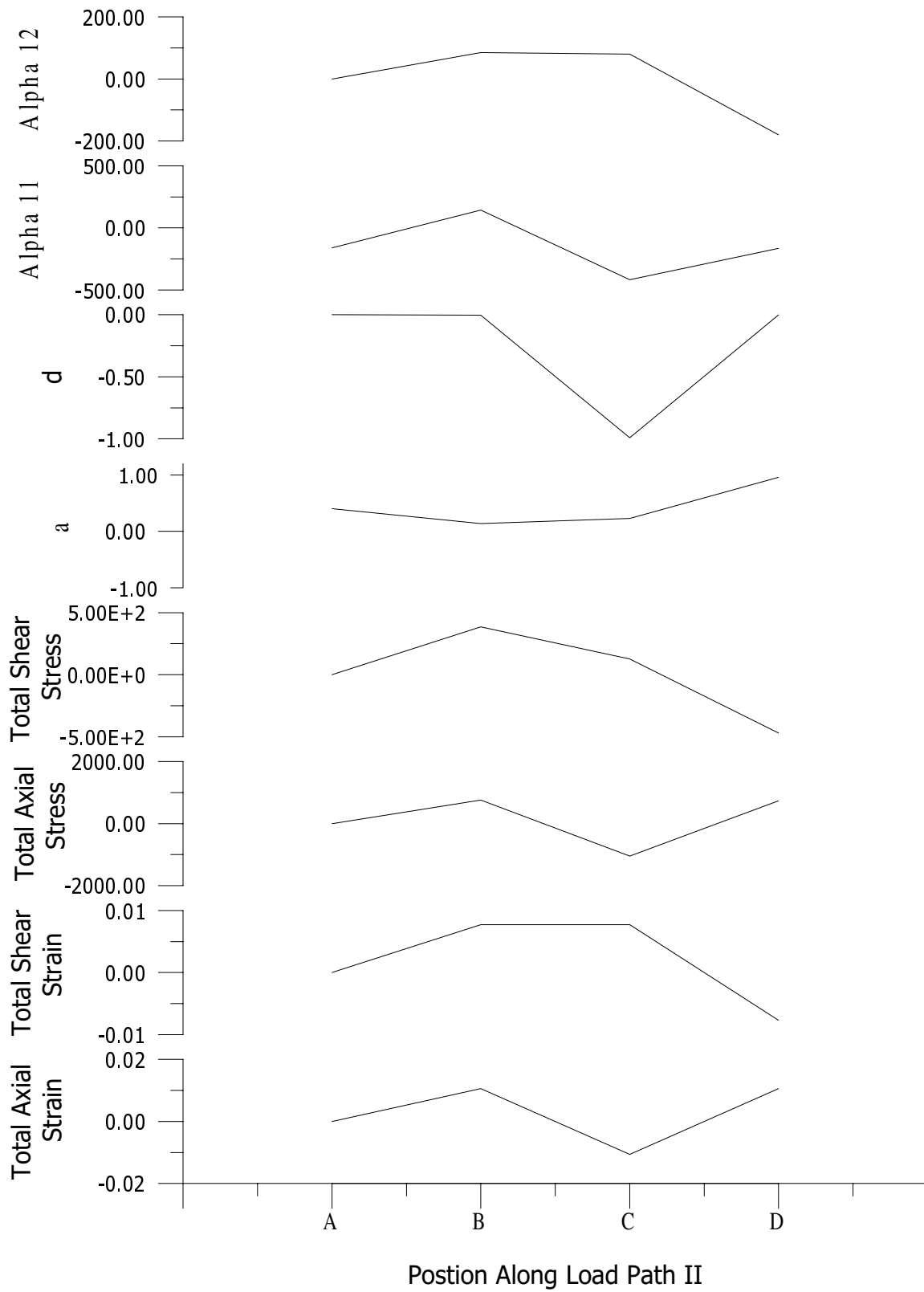**Figure 4.24:** Voyiadjis model parameter evolution for IN 718, Path III, IN-27.
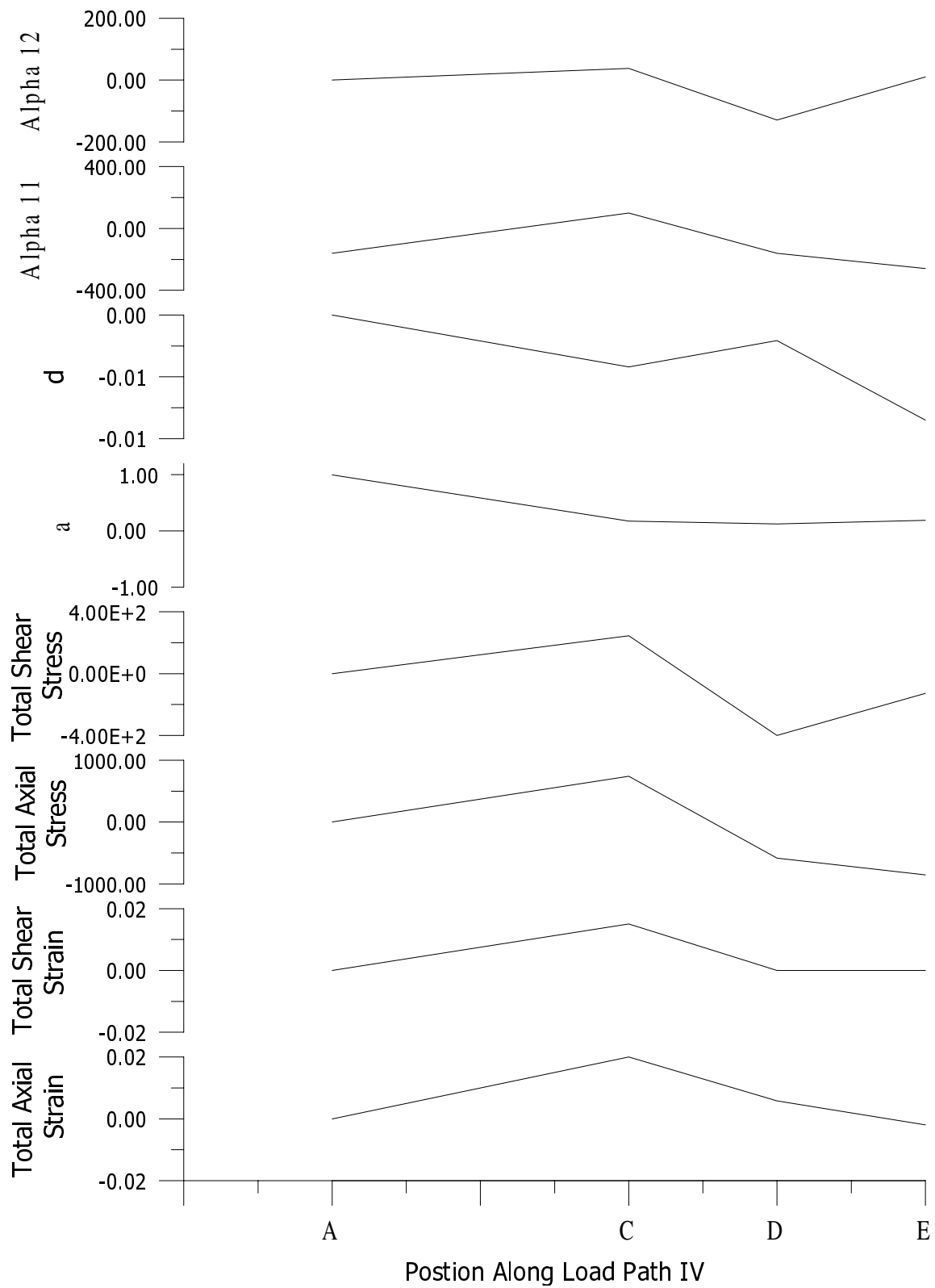
Figure 4.25: Voyiadjis model parameter evolution for IN 718, Path IV, IN-11.
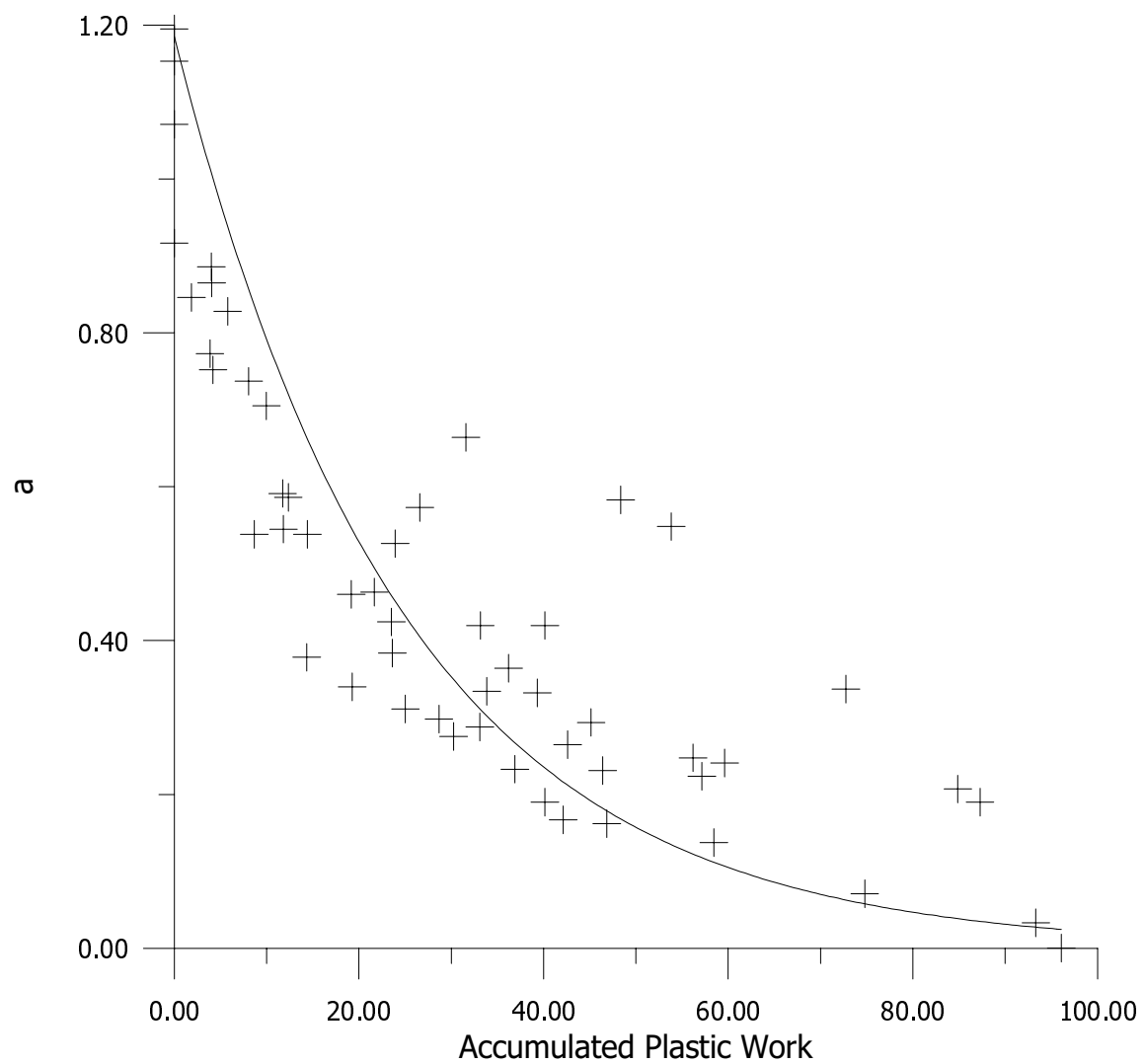
Figure 4.26: Evolution of *a* versus plastic work for HN 188.
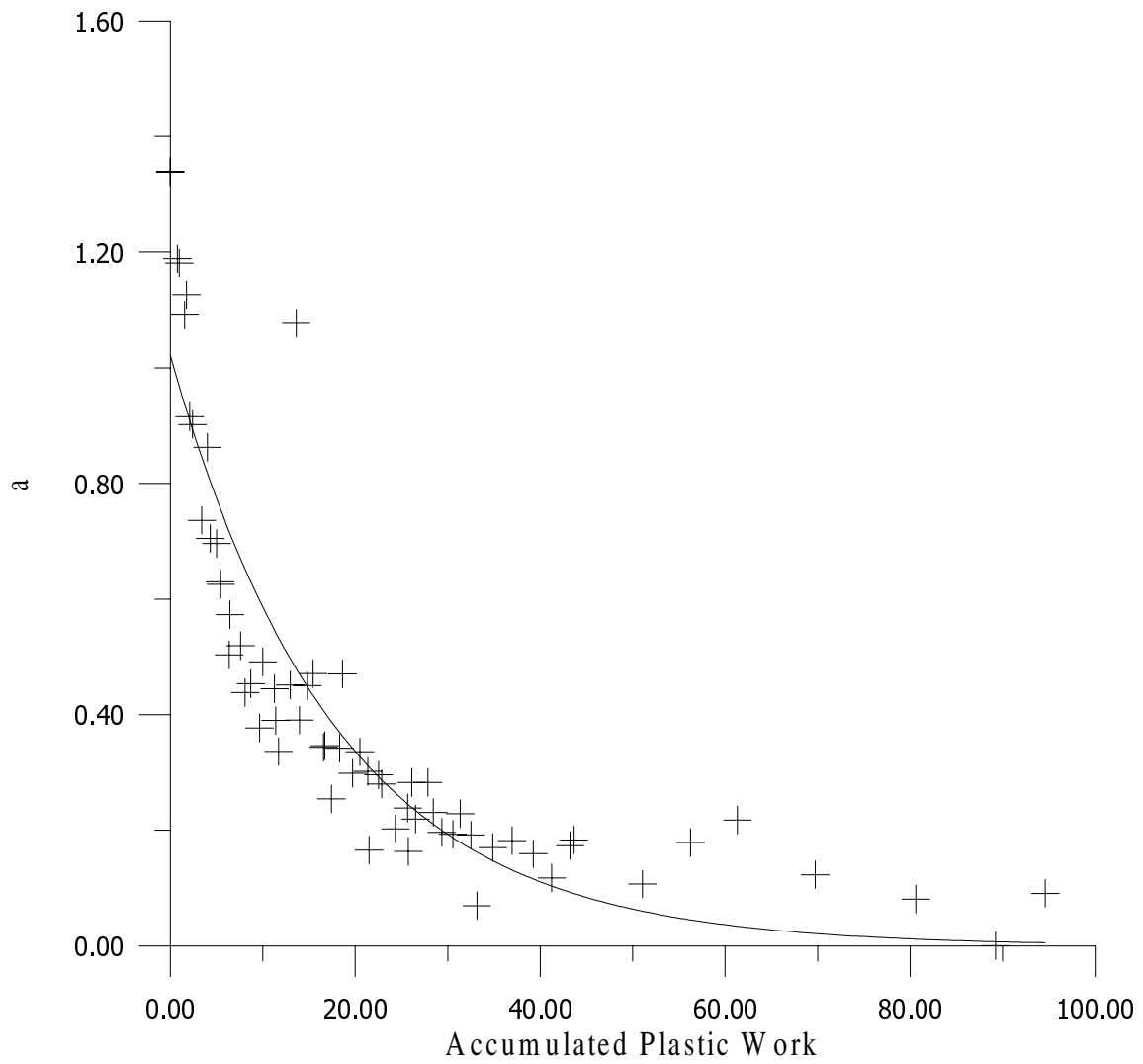
Figure 4.27: Evolution of *a* versus plastic work for SS 316.
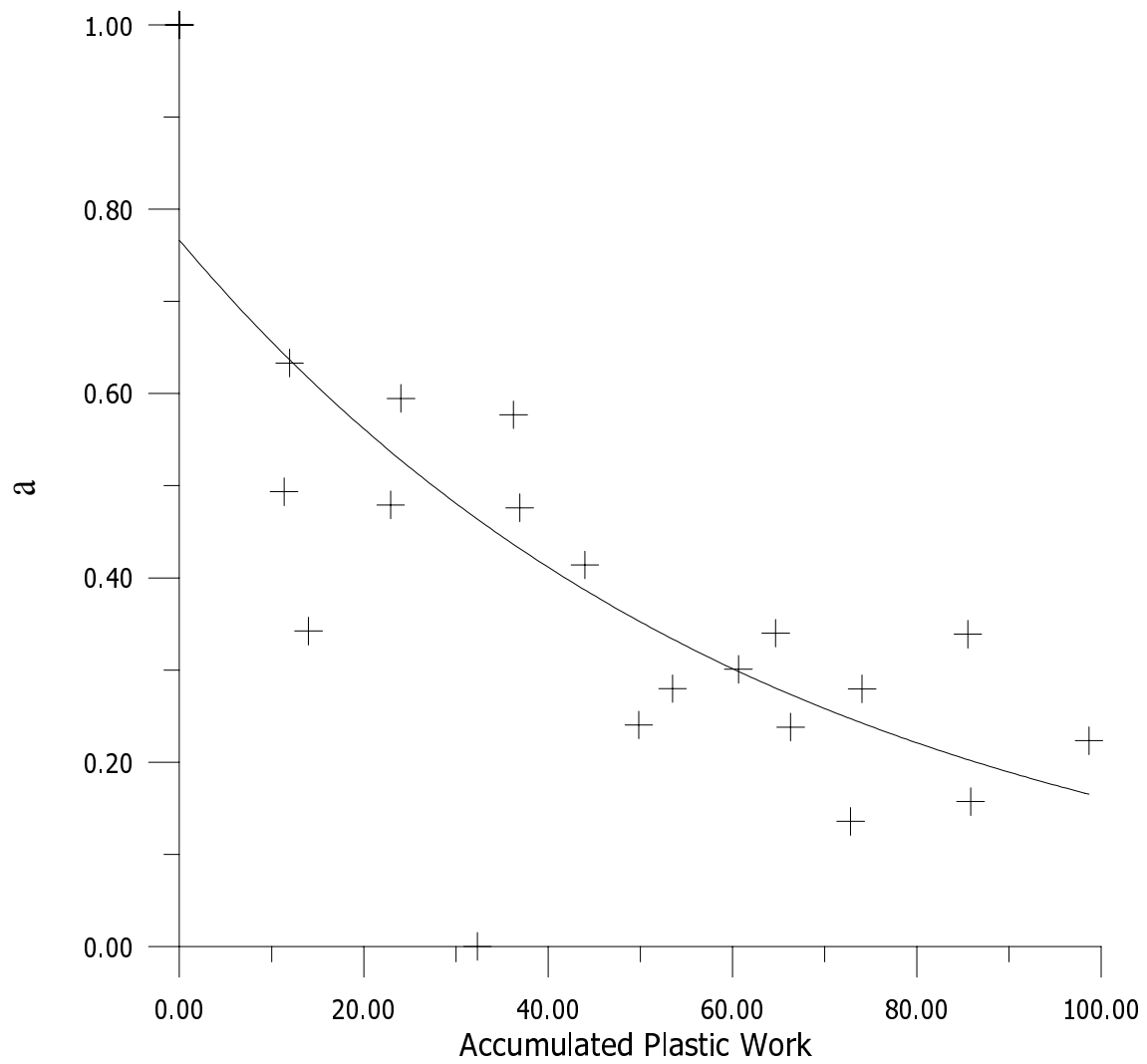
Figure 4.28: Evolution of *a* versus plastic work for IN 718.
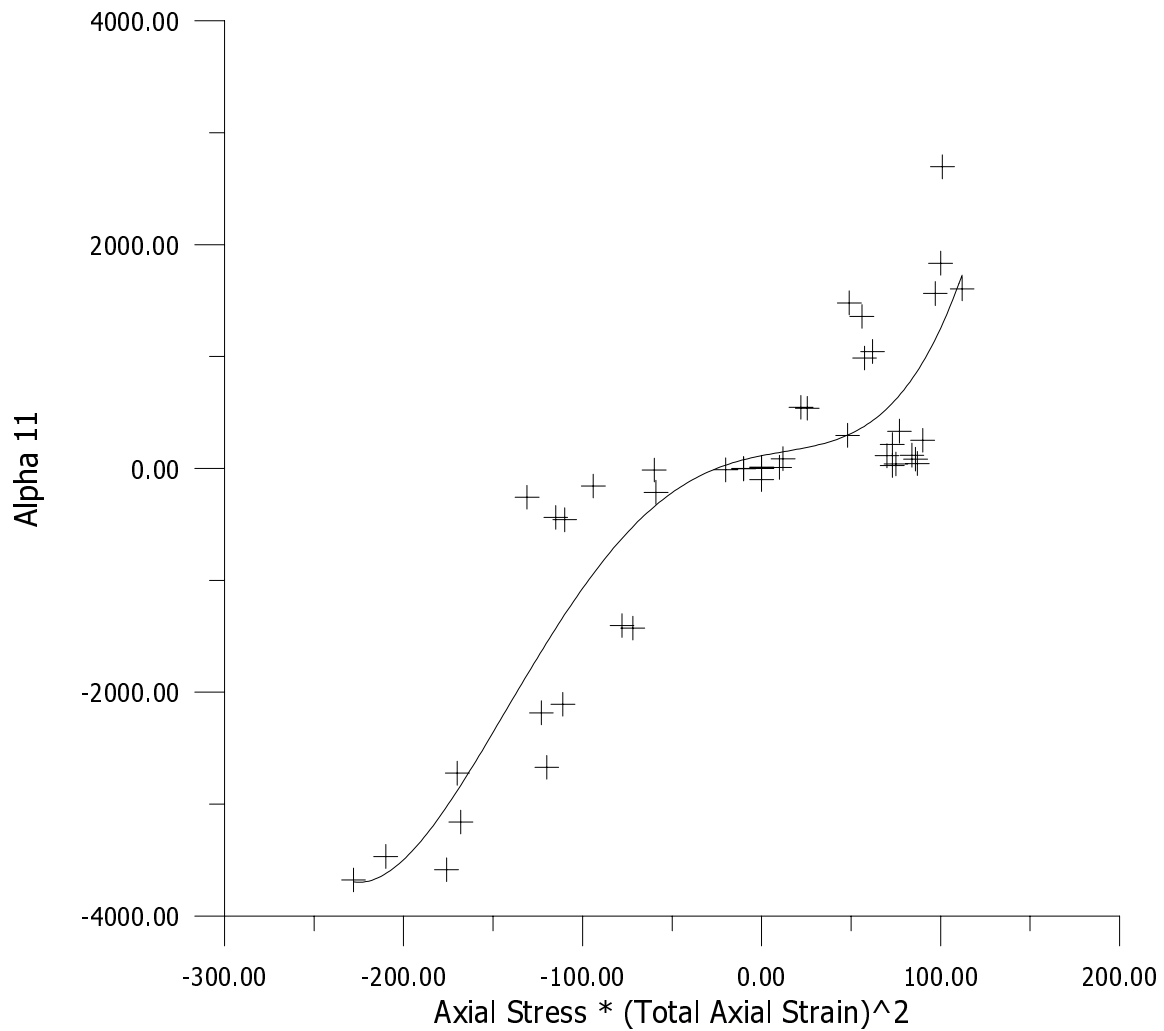
Figure 4.29: Evolution of α_{11} versus stress times total strain squared for HN 188
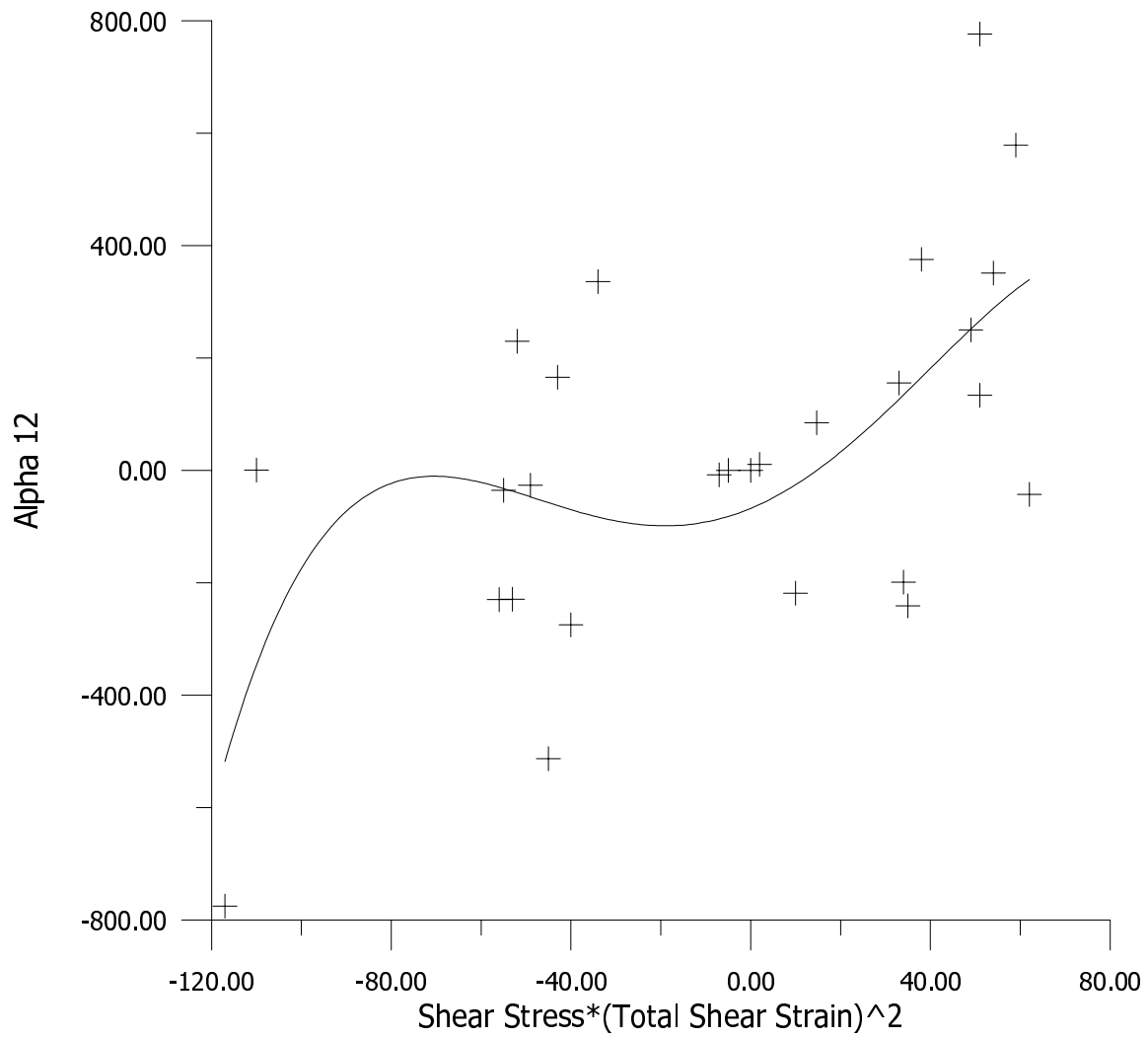
Figure 4.30: Evolution of α_{12} versus stress times total strain squared for HN 188

Chapter 5

Conclusions and Future Work

This chapter provides a summary of the major conclusions from both the experimental and analysis portions of this study as well as some suggestions for future work.

5.1 Conclusions

This study had two very distinct parts. First was the experimental portion and the other was the data analysis portion. Both has it own set of conclusions.

Experimental

- Plastic flow in Haynes 188, 316 Stainless Steel, and Inconel 718 complicated and highly alloy dependent, with each material exhibiting varying degrees of each of the three components of hardening; isotropic, kinematic, and distortional.

- All subsequent yield surfaces had two distinct parts; a well defined front side and a poorly defined backside. The front side was nearly circular in the axial-shear stress plane and the backside was flattened.

- Subsequent yield surfaces continued to evolve through multiple cycles of a given load path.

- Even thought the three alloys tested were vastly different it appears that the same type of evolution equations could represent the multiaxial hardening of each material.

Data Analysis

- The Voyiadjis model adequately describes subsequent yield surfaces with only four parameters; one isotropic, one distortional, and two backstress parameters.

- The isotropic parameter, a, and kinematic parameters, α_{11} and α_{12}, evolve smoothly though the entire set of yield surface tests.

- The distortional hardening parameter, d, is difficult to describe, partly because of the large amount of scatter in the yield points on the backside of the yield surface.

- Evolution of the isotropic hardening parameter and kinematic hardening parameters can be reasonably well described by simple equations.

5.2 Future Work

The work presented here attempts to quantify the evolution of subsequent yield surfaces. This process includes many experimental and mathematically difficulties. However, now that the groundwork is set for determining the necessary parameters for quantifying yield surfaces there are many areas that require more attention. Of primary concern is improving the yield surface fits. Some suggestions are,

- Reducing the amount of experimental scatter in the backside of subsequent yield surfaces. Two approaches would apply,

  1. Study the effect of probing rate on backside scatter.

2. Study the effect of the offset strain target value on backside scatter.

In either case the sensitivity studies would be carried out for subsequent yield surfaces instead of initial yield surfaces as done with the current study.

- Further investigate the increased yield surface scatter observed in IN 718 as instead of SS 16 and HY 188.

In addition to improving the experimental data further work is needed in developing evolution equations for the yield surface parameters. The ultimate goal is to develop evolution equations to be used in a viscoplasticity model to predict yield surfaces for a given plastic strain value.

References

1. Tresca, H. (1864) "Sur l'ecoulement des corps solides soumis 'a defortes pression," *C.R. Acad. Sci*, Paris, Vol 59, pp 754.

2. von Mises, R. (1913) "Mechanics of Solids in the Plastically Deformable State" NASA Technical Memorandum 88488, 1986. (translation of " Zustrand, Nachrichten von der Koniglichen," *Gesellschaft der Wissenschaften*, pp 582-592.

3. von Mises, R. (1928) "Mechanik der plastischen Formaenderung von Kristallen," *Zeitschrigt fur Angewandte Mathematik und Mechanik*, Vol 8, pp 161-185.

4. Prandtl, L. (1924) "Spannungsverteilung in plastischen Koerpern," *Preceedings. 1ˢᵗ International Congress on Applied Mechanics*, Delft, J Waltman, jr. Ed., Technische Boekhandel en Druckerij, pp 43-54.

5. Reuss, E. (1930) "Beruecksichtigung der elastischen Formaenderungen in der Plastizitaetstheorie," *Zeitschrift fur Angewandte Mathematik und Mechanik*, Vol 10, pp 266-274.

6. Ortiz, M. and Popov, E. (1983) "Distortional Hardening Rules for Metal Plasticity," *Journal of Engineering Mechanics*, Vol 109 No. 4, pp 1042-1057.

7. Eisenberg, M.A. and Yen, C. (1984) "The Anisotropic Deformation of Yield Surfaces," *Journal of Engineering Material and Technology*, Vol 106, pp 355-360.

8. Kurtyka, T. and Zyczkowski, M. (1985) " A Geometric Description of Distortional Plastic Hardening of Deviatoric Materials," *Archives of Mechanics*, Vol 37, pp 383-395.

9. Kurtyka, T. and Zyczkowski, M. "A Description of Distortional Plastic Hardening of Anisotropic Materials," *Yielding, Damage, and Failure of Anisotropic Solids*, J. P. Boehler Ed., 1990, Mechanical Engineering Publications, London, pp 97-111.

10. Kurtyka, T. and Zyczkowski, M. (1995) "Evolution Equations for Distortional Plastic Hardening," *International Journal of Plasticity*, Vol 12, no. 2, pp 191-213.

11. Rees, D. W. A. (1984) "An Examination of Yield Surface Distortion and Translation," *Acta Mechanica*, Vol 52, pp 15-40.

12. Voyiadjis, G. Z. and Foroozesh, M. (1990) "Anisotropic Distortional Yield Model," *Journal of Applied Mechanics*, Vol 57, pp 537-547.

13. Voyiadjis, G. Z., Thiagarajan, G., and Petrakis, E. (1994) "Constitutive Modelling for Granular Media Using an Anisotropic Distortional Yield Model," *Acta Mechanica*, Vol 107, pp 1-21.

14. Hill, R. (1948) "A Theory of the Yielding and Plastic Flow of Anisotropic Metals," Proc. Roy. Soc., London, Series A, Vol. 193, pp 281-297.

15. Arnold, S. M. and Saleeb, A. F. (1994) " On the Thermodynamic Framework of Generalized Coupled Thermoelastic-Viscoplastic-Damage Modeling," *International Journal of Plasticity*, Vol 10 No. 3, pp 263-278.

16. Arnold, S. M., Saleeb, A. F., Castelli, M. G. (1996) "A Fully Associative, Nonlinear Kinematic Unified Viscoplastic Model for Titanium Bases Matrices," *Life Predication Methodology for Titanium Matrix Composites, ASTM STP 1253*, Johnson W. S., Larsen J. M., and Cox, B.N. Eds., American Society for Testing and Materials, pp 231-256.

17. Arnold, S. M., Saleeb, A. F., Wilt, T. E. (1995) "A Modeling Investigation of Thermal and Strain Induced Recovery and Nonlinear Hardening in Potential Based Viscoplasticity," *Journal of Engineering Materials and Technology*, Vol. 117, pp 157-167.

18. Bonder, S. R. and Partom, Y. (1975) "Constitutive Equations for Elastic-Viscoplastic Strain-Hardening Materials," *Jouranl of Applied Mechanics*, Vol 42, pp 385-389.

19. Bonder, S. R. and Partom, Y. (1972) " A Large Deformation Elastic-Viscoplastic Analysis of a Thick-Walled Spherical Shell," *Journal of Applied Mechanics*, Vol 39, pp 751-756.

20. Hecker, S. S. (1976) "Experimental Studies of Yield Phenomena in Biaxially Loaded Metals," *Constitutive Equations in Viscoplasticity: Computational and Engineering Aspects*, ASME, pp 1-33.

21. Michno, M. J. and Findely, W. N. (1976) "An Historical Perspective of Yield Surface Investigations for Metals," *International Journal of Non-Linear Mechanics*, Vol. 11, pp 59-82.

22. Phillips, A., Liu, C. S., and Justusson, J. W. (1972) "An Experimental Investigation of Yield Surfaces at Elevated Temperature," *Acta Mechanica*, Vol. 14, pp 119-146.

23. Phillips, A. and Tang, J. L. (1972) "The Effects of Loading Path on the Yield Surface at Elevated Temperature," *International Journal of Plasticity*, Vol. 8, pp 463-474.

24. Phillips, A. and Moon, H. (1977) "An Experimental Investigation Concerning Yield Surface and Loading Surfaces," *Acta Mechanica*, Vol. 27, pp 91-102.

25. Phillips, A. and Lu, W. (1984) "An Experimental Investigation of Yield Surface and Loading Surfaces of Pure Aluminum with Stress-Controlled and Strain-Controlled Paths of Loading," *Journal of Engineering Material and Technology, Trans. ASME*, Vol. 106, pp 349-354.

26. Helling, D. E., Miller, A. K., and Stout, M. G. (1986) "An Experimental Investigation of the Yield Loci of 1100-0 Aluminum, 70:30 Brass, and an Overaged 2024 Aluminum Alloy After Various Prestrains," *Journal of Engineering Material and Technology*, Vol. 108, pp 313-320.

27. Helling, D. E., and Miller, A. K. (1987) "The Incorporation of Yield Surface Distortion into a Unified Constitutive Model, Part 1: Equation Development," *Acta Mechanica*, Vol. 69, pp 9-23.

28. Helling, D. E., and Miller, A. K. (1988) "The Incorporation of Yield Surface Distortion into a Unified Constitutive Model, Part 2: Predictive Capabilities," *Acta Mechanica*, Vol. 72, pp 39-53.

29. Lissenden, C. J., Lerch, B. A., Robinson, D. N. (1996) "Verification of Experimental Techniques for Flow Surface Determination," NASA Technical Memorandum 107053.

30. Gil, C. M., Lissenden, C. J., Lerch, B. A. (1999) "Yield of Inconel 718 by Axial-Torsional Loading at Temperatures up to 649°C," *Journal of Testing and Evalution,* Vol. 20, no.5, pp 327-336.

31. Naghdi, P. M., Cailletaud, G. (1996) "Finite Element Analysis of the Mechanical Behavior of Two-Phase Single-Crystal Superalloys," *Scripta Materialia*, Vol. 34, no. 2, pp 565-571.

32. Taylor, G. I., Quinney, H. (1931) "The Plastic Distortion of Metals," *Philosophical Transactions of the Royal Society*, London, Vol. A230, pp 323-363.

33. Wu, H. C., Yeh, W. C., (1991) "On the Experimental Determination of Yield Surfaces and Some Results of Annealed 304 Stainless Steel," *International Journal of Plasticity*, Vol. 7, pp 803-826.

34. Ellis, J. R., Robinson, D. N., and Pugh C. E. (1985) "Time Dependence in Biaxial Yield of Type 316 Stainless Steel at Room Temperature," *Journal of Engineering Materials and Technology*, Vol. 105, pp 250-256.

35. Lui, K.C. (1977) "Yield Surfaces and Elastic-Plastic Behavior of Type 304 Stainless Steel," *ORNL/TM-5421*, Oak Ridge National Laboratory, Oak Ridge, TN, April.

36. Hecker, S. S. (1971) "Yield Surfaces in Prestrained Aluminum and Copper," *Metall. Trans.*, Vol. 2, pp 2077-2086.

37. Khan, A. and Wang, X. (1993) "An Experimental Study on Subsequent Yield Surfaces After Finite Shear Prestraining," *International Journal of Plasticicty*, Vol. 9, pp 889-905.

38. Williams, J. F. and Svensson, N. L. (1970) "Effect of Prestrain on the Yield Locus of 1100-F Aluminum," *Journal of Strain Analysis*, Vol. 5, pp 128-139.

39. Kalluri, S. and Bonacuse, P. J. (1990) "A Data Acquisition and Control Program for Axial-Torsional Fatigue Testing," *Applications of Automation Technology to Fatigue and Fracture Testing, ASTM STP 1092,* A. A. Braun, N. E. Ashbaugh, and F. M. Smith, Eds., American Society for Testing and Materials, Philadelphia, pp. 269-287.

40. Ellis, J. R. and Bartolotta, P. A. (1997) "Adjustable Work Coil Fixture Facilitation the Use of Induction Heating in Mechanical Testing," *Multiaxial Fatigue and Deformation Testing Techniques, ASTM STP 1280*, S. Kalluri and P. J. Bonacuse, Eds., American Society for Testing and Materials, pp 43-62.

41. Lissenden, C. J., Lerch, B. A., Ellis, J. R., and Robinson, D. N. (1997) "Experimental Determination of Yield and Flow Surfaces Under Axial-Torsional Loading," *Multiaxial Fatigue and Deformation Testing Techniques, ASTM STP 1280*, S. Kalluri and P. J. Bonacuse, Eds., American Society for Testing and Materials, pp 92-112.

42. Hecker, S. S. (1976) "Experimental Studies of Yield Phenomena in Biaxial Loaded Metals," *Constitutive Equations in Viscoplasticity: Computational and Engineering Aspects*, ASME, pp 1-33.

43. Lissenden, C. J., Walker, M. A., and Lerch, B. A. (2000) "Axial-Torsional Load Effects of Haynes 188 at 650ºC," *Multiaxial Fatigue and Deformation: Testing and Predicition, ASTM STP 1387*, S. Kalluri and P. J. Bonacuse, Eds., American Society for Testing and Materials, pp 99-125.

44. Gil, C. M., Lissenden, C. J., and Lerch B. A. (1998) "Determination of Yield in Inconel 718 for Axial-Torsional Loading at Temperatures up to 649ºC," NASA Technical Memorandum 208658.

45. Kiemele, M. J., Schmidt, S. R., and Berdine, R. J. (1997) <u>Basic Statistics: Tools for Continuous Improvement</u>. Air Academy Press, Colorado Springs, Colorado.

46. Gil, C. M. (1998) "Determination of Yield and Flow Surfaces for Inconel 718 Under Axial-Torsional Loading Temperatures up to 649ºC." Thesis, Penn State University.

47. Hirth, J. P. and Cohen, M. (1970) "On the Strength-Differential Phenomenon in Hardened Steel," *Metallurgical Transactions*, Vol. 1, pp 3-8.

48. Ziebs, J., Meersmann, J., Kuhn H. J., and Ledworuski, S. (996) "Experimental Techniques for Testing Materials Under Multiaxial Loading," *Multiaxial Fatigue and Design*, A. Pineau, G. Cailletaud, and T. C. Lindley Eds., Mechanical Engineering Publications, London, pp 173-193.

49. Winstone, M. R. (1983) "Influence of Prestress on the Yield Surface of the Cast Nickel Superalloy MAR-M002 at Elevated Temperature," *Mechanical Behaviour of Materials IV*, J, Carlsson and N. G. Ohlson Eds., Vol. 1, pp 199-205.

50. Lubliner, J. (1990) <u>Plasticity Theory</u>. Macmillan Publishing Company, New York.

51. Kassner, M. E., Ziaai-Moayyed, A. A., and Miller, A. K. (1985) "Some Trends in the Elevated Temperature Kinematic and Isotropic Hardening of Type 304 Stainless Steel," *Metallurgical Transactions*, Vol 16A, pp 1069-1076.

52. Klarstrom, D. L. (1993) "Wrought Cobalt-Base Superalloys," *Journal of Materials Engineering Performance*, Vol. 2, pp 523-529.

53. Wegener, K. and Schlegel, M. (1996) "Suitability of Yield Functions for the Approximation of Subsequent Yield Surfaces," *International Journal of Plasticity*, Vol. 12, no. 9, pp 1151-1177.

54. Wu, H. C. and Yeh, W. C. (1987) "Some Considerations in the Endochronic Description of Anisotripic Hardening," *Acta Mechanica*, Vol. 69, pp 59-76.

55. Gupta, N. K. and Meyers, A. (1994) "An Alternative Formulation for Interpolation Experimental Yield Surfaces," *International Journal of Plasticity*, Vol. 10, no. 7, pp 795-805.

56. Gil, C. M., Lissenden, C. J., and Lerch, B. A. (1999) "Unusual Nonlinear Response of Some Metallic Materials," *Mechanics of Materials*, Vol. 31, pp 565-577.

57. Gil, C. M., Lissenden, C. J., and Lerch, B. A. (1998) "Investigation of Anomalous Behavior in Metallic-Based Materials Under Compressive Loading," NASA Technical Memorandum 206640.

58. Cho, H. W. and Dafalias, Y. F. (1996) "Distortional and Orientational Hardening at Large Viscoplastic Deformations," *International Journal of Plasticicty*, Vol. 12, no. 7, pp 903-925.

59. Yen, C. F. and Eisenburg, M. A. (1987) "The Role of a Loading Surface in Viscoplasticity Theory." *Acta Mechanica*, Vol 69, pp 77-96.

Appendix A

Catalog of Yield Surface Data

Appendix A begins with a list of all specimens tested and the dimensions of each.
The second section contains all yields surfaces collected along with the fit data for each.

A.1 Specimen Dimensions

Material	Specimen Number	Test Path	Outside Diameter (in)	Inside Diameter (in)
Haynes 188	HYII 82	III	1.0241	0.8669
	HYII 85	I	1.0227	0.8660
	HYII 86	II	1.0238	0.8656
	HYII 89	I	1.0231	0.8663
	HYII 90	III	1.0237	0.8653
316 Stainless	610-01	I	1.0257	0.8675
	610-04	II	1.0252	0.8678
	610-05	III	1.0257	0.8680
Inconel 718	11	IV	0.8225	0.6244
	14	VI	0.8220	0.6238
	16	I	0.8195	0.6245
	23	II	0.8230	0.6244
	27	III	0.8190	0.6236
	28	V	0.8203	0.6242

Table A.1: Specimen dimensions and test matrix.

A.2 Yield Surface Data

All yield surface data are presented here. Figures A.1 through A.12 show HN 188 data, Figures A.13 through A.27 show SS 316 data, and Figures A.28 through A.32 show IN 718 data. The experimental data is represented by plus signs and diamonds (the first and second repeated surfaces), the fits are shown by a solid line, and the initial surface is shown by a dashed line. In addition, the model parameters a and d as well as the R^2 values are shown on each graph.
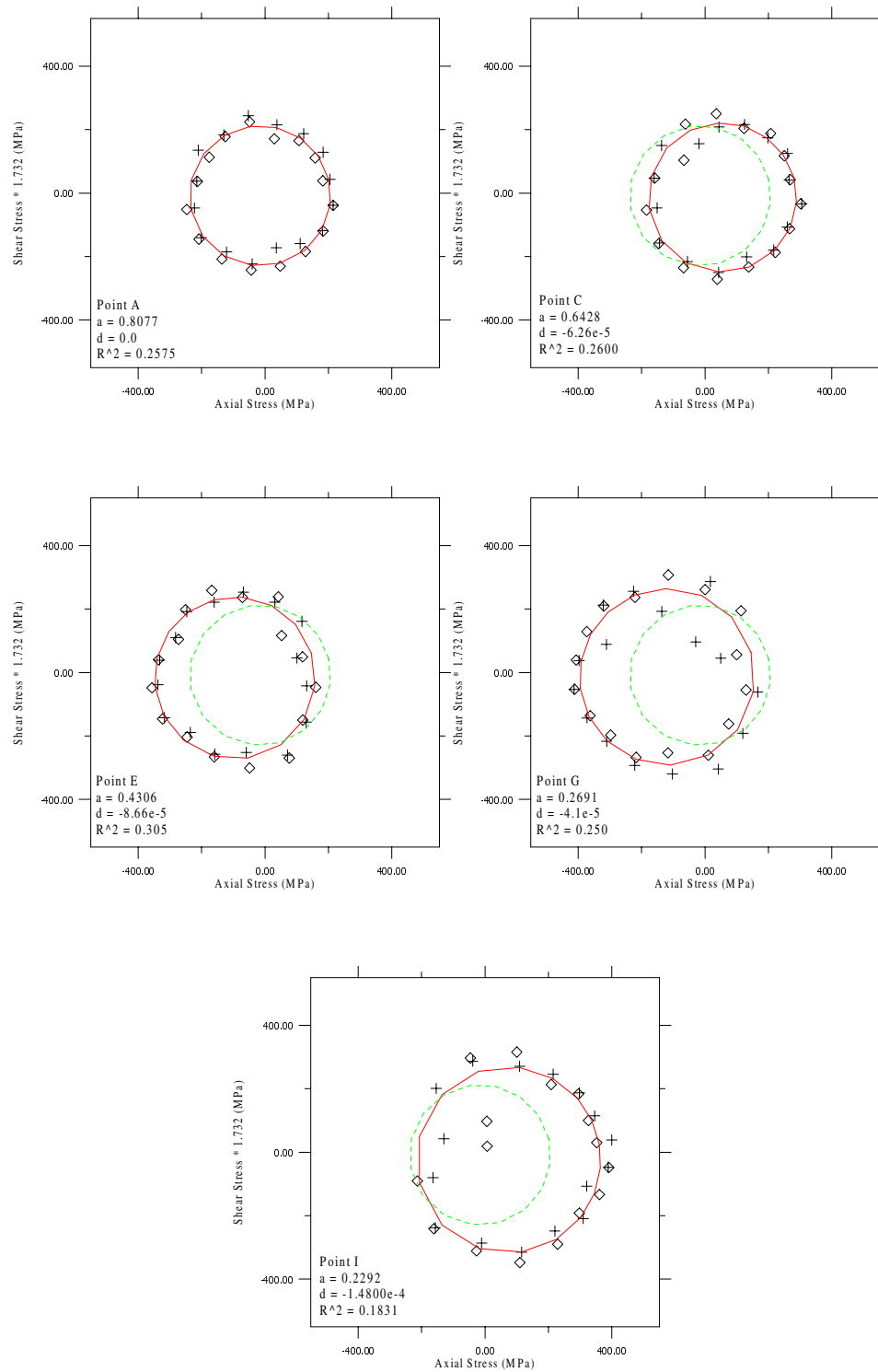
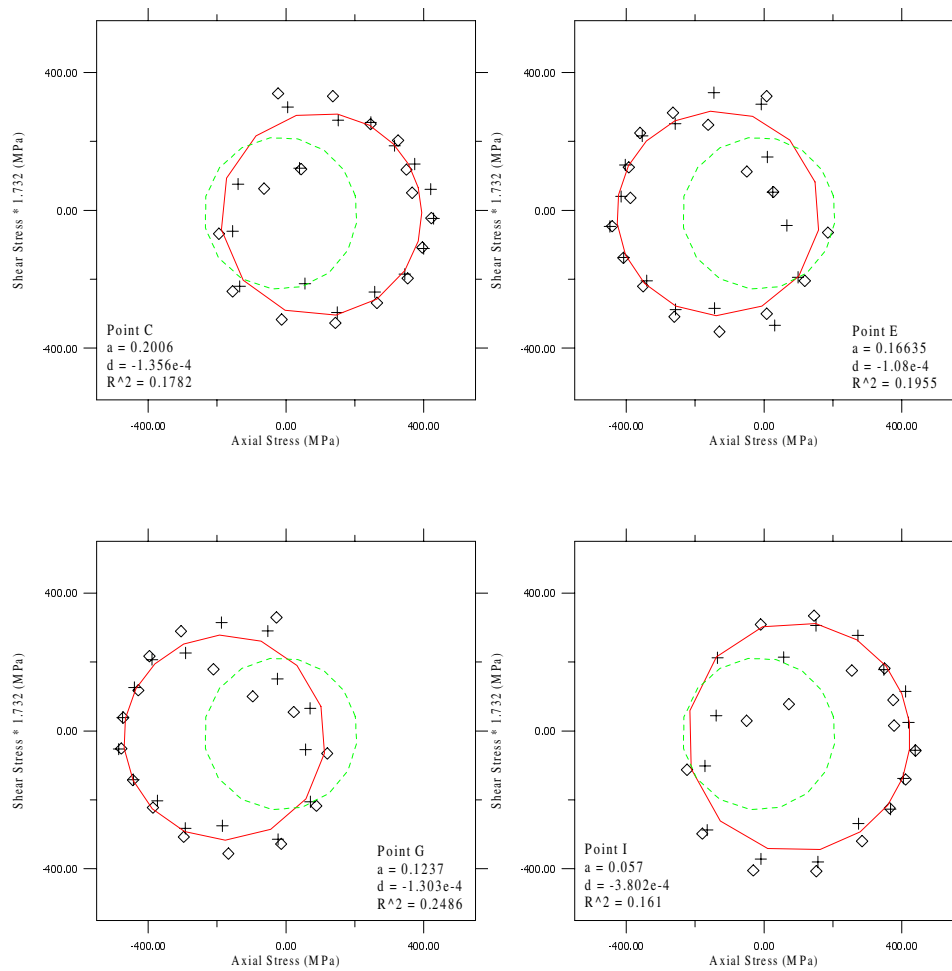**Figure A.1:** Haynes 188, Path I, Points A–I, Cycle 1, HYII-89.

Figure A.2: Haynes 188, Path I, Point C-I, Cycle 2, HYII-89.
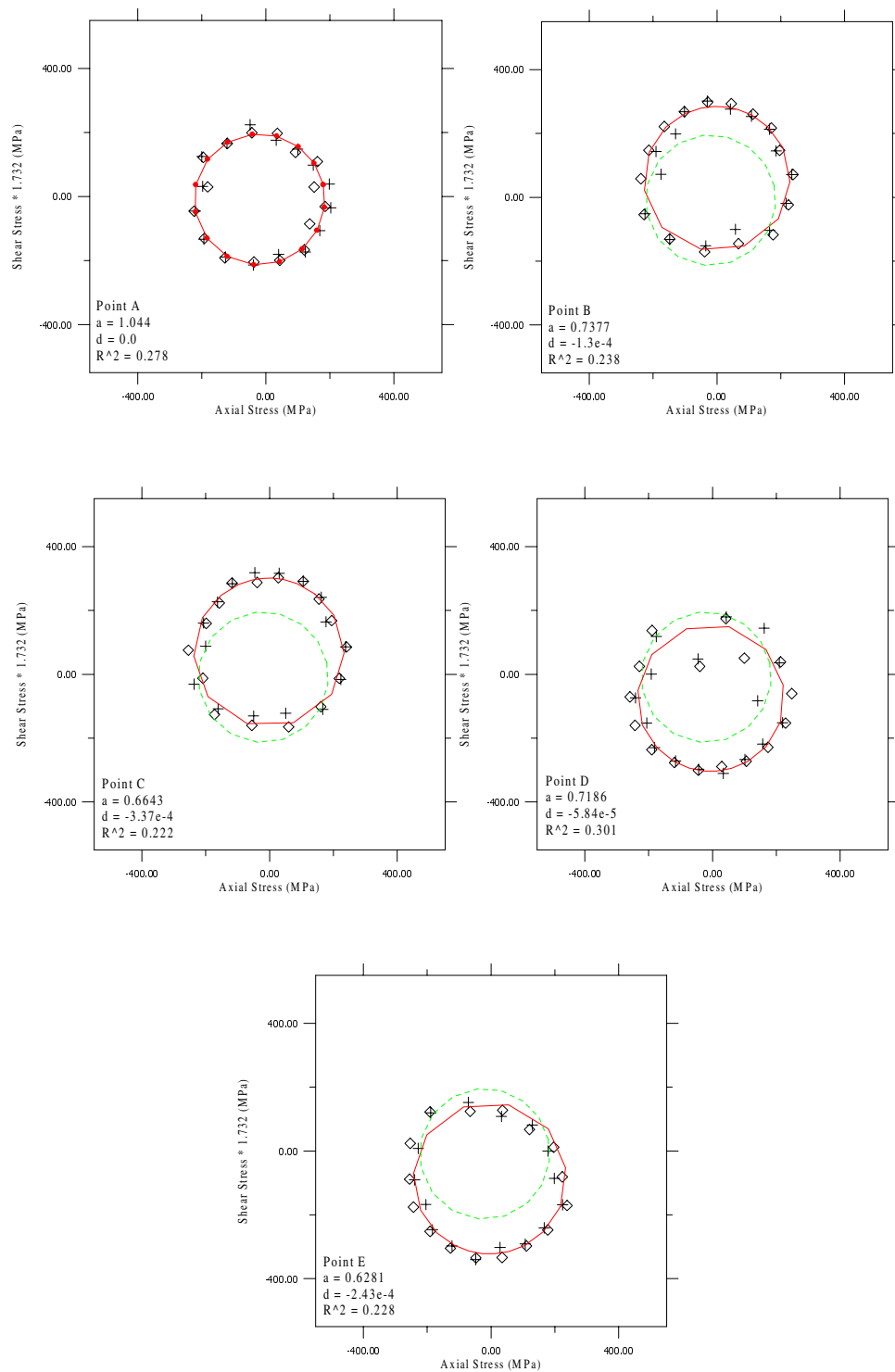
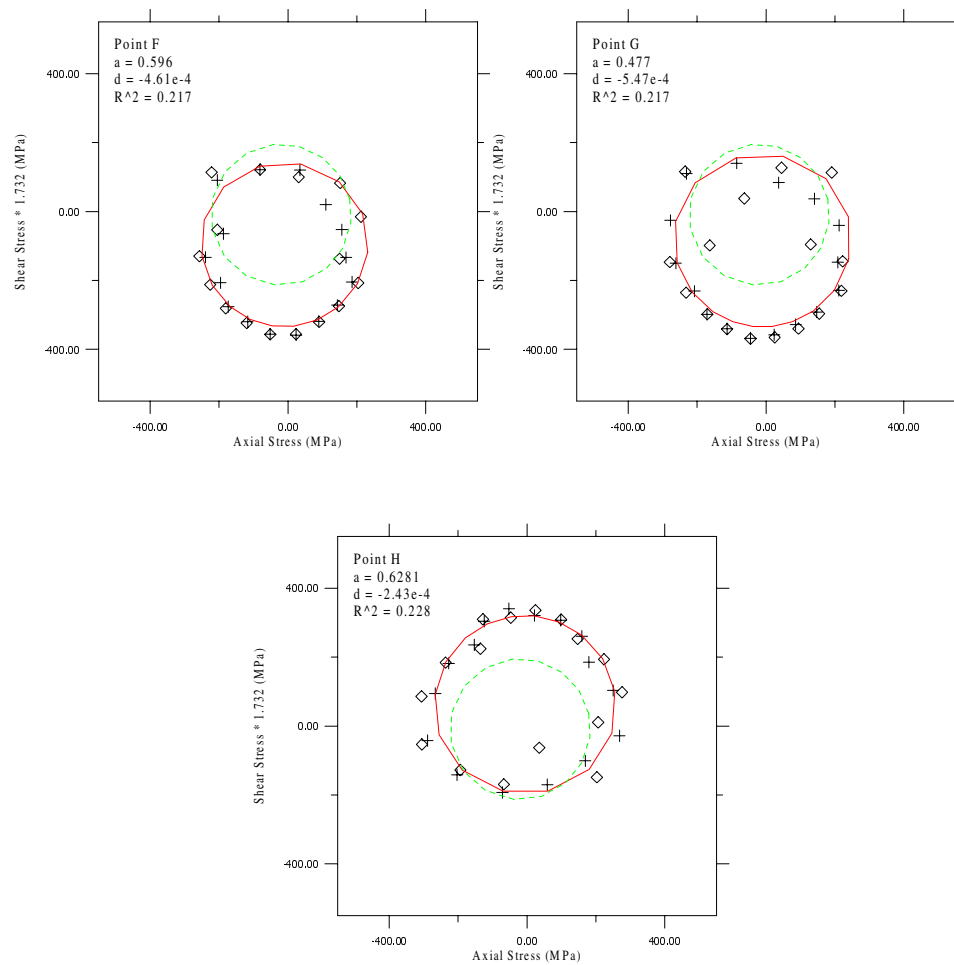**Figure A.3:** Haynes 188, Path II, Points A-E, Cycle 1, HYII-86.

Figure A.4: Haynes 188, Path II, Points F-H, Cycle 1, HYII-86.
(The data for point I was bad therefore not fit was performed.)

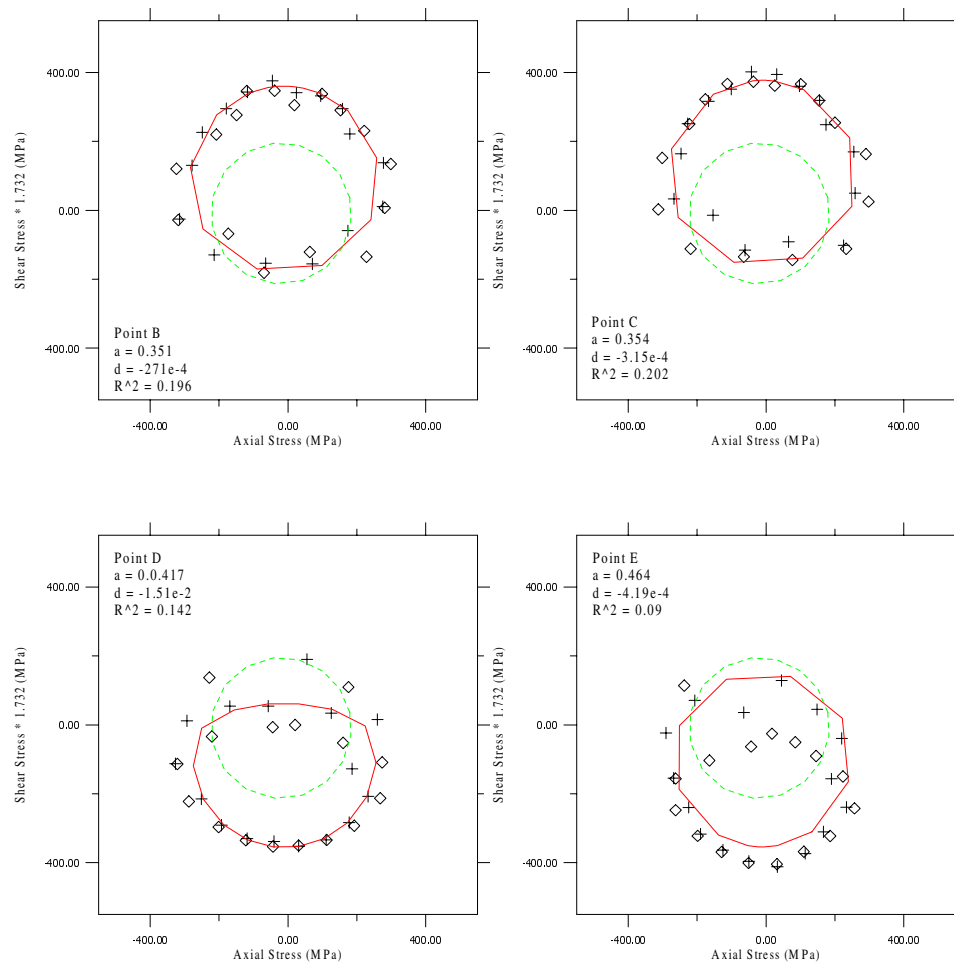**Figure A.5:** Haynes 188, Path II, Points B-E, Cycle 2, HYII-86.

Figure A.6: Haynes 188, Path II, Points F-I, Cycle 2, HYII-86.
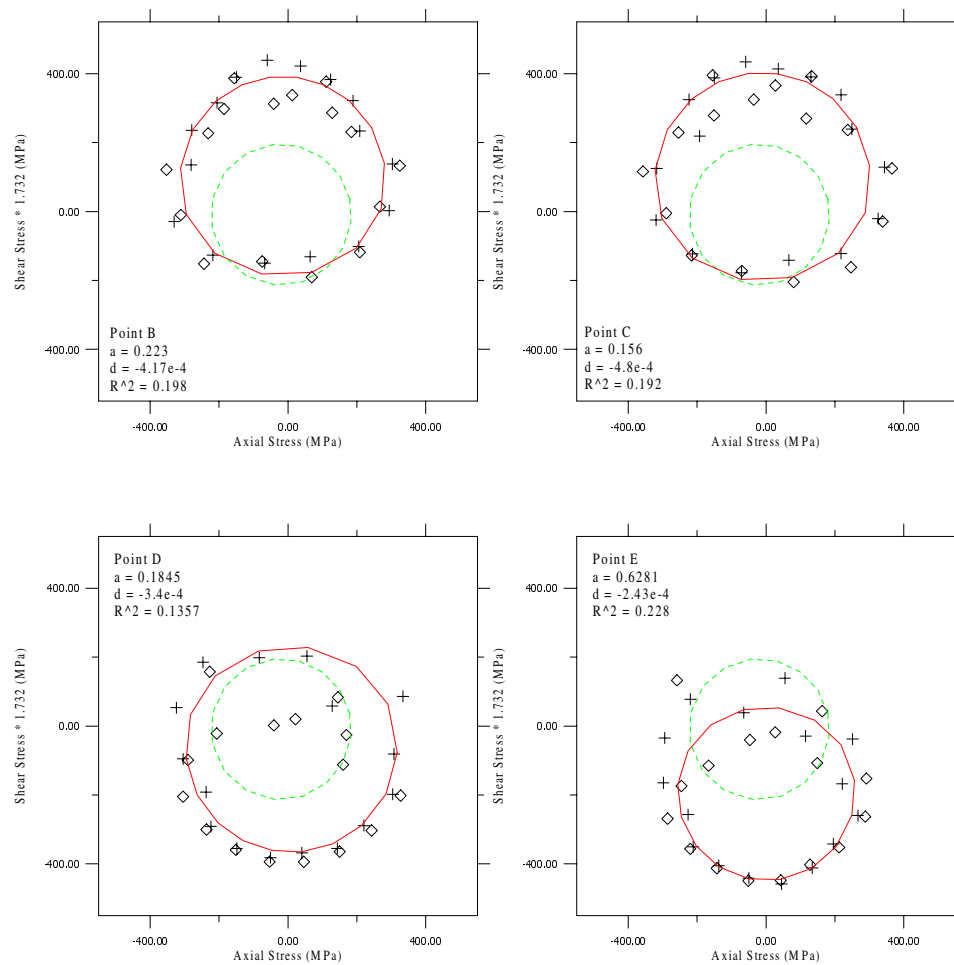
Figure A.7: Haynes 188, Path II, Points B-E, Cycle 3, HYII-86.
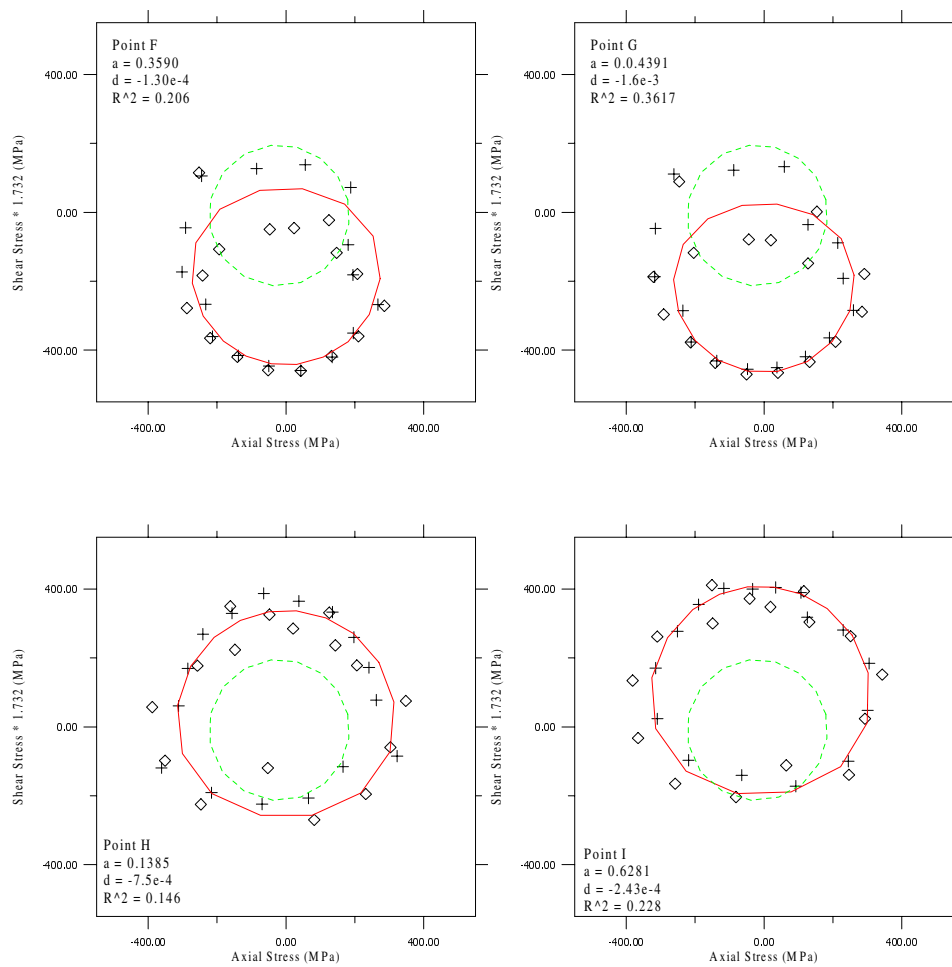
Figure A.8: Haynes 188, Path II, Points F-I, Cycle 3, HYII-86.
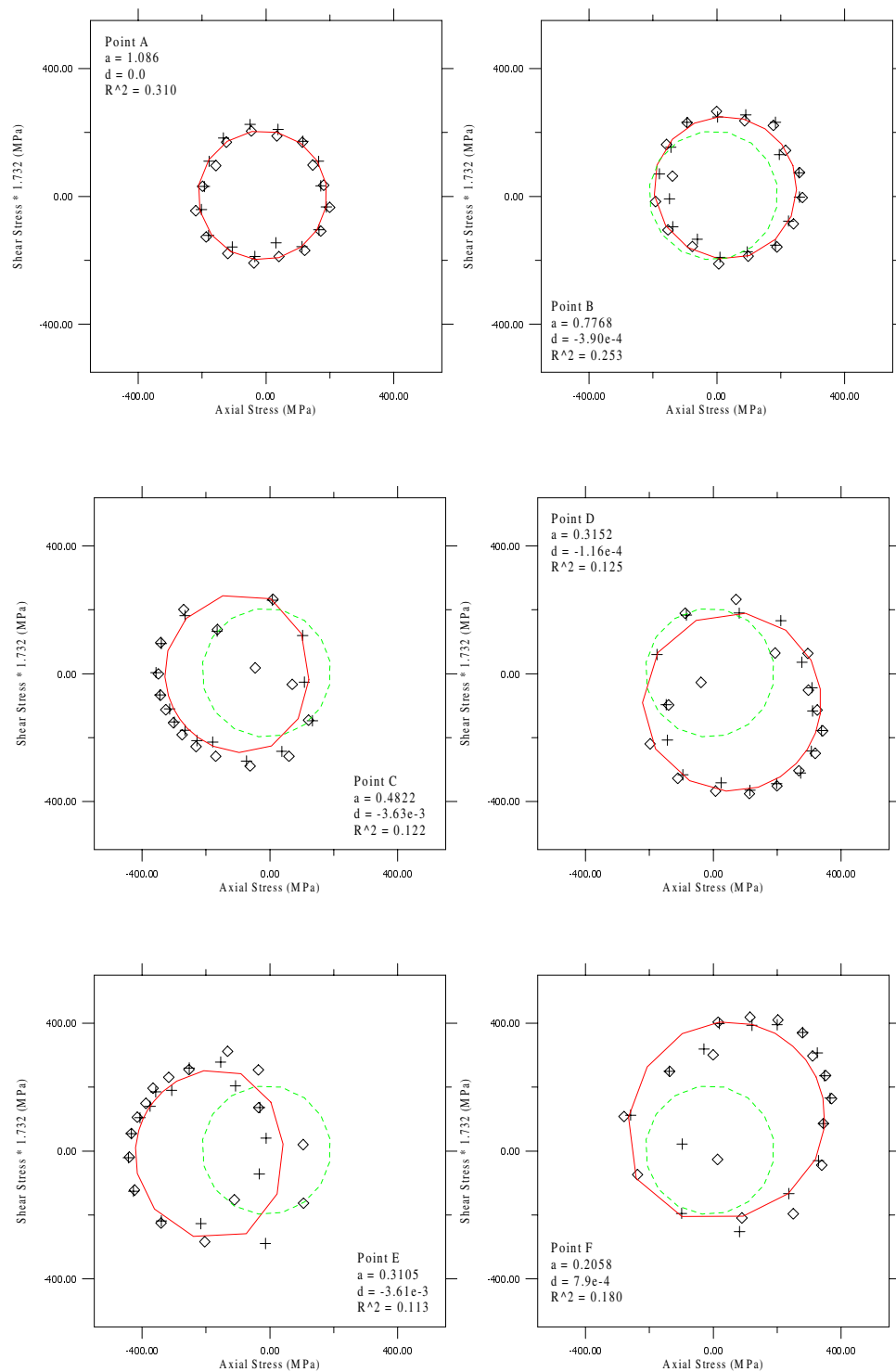
Figure A.9: Haynes 188, Path III, Points A-F, Cycle 1, HYII-90.
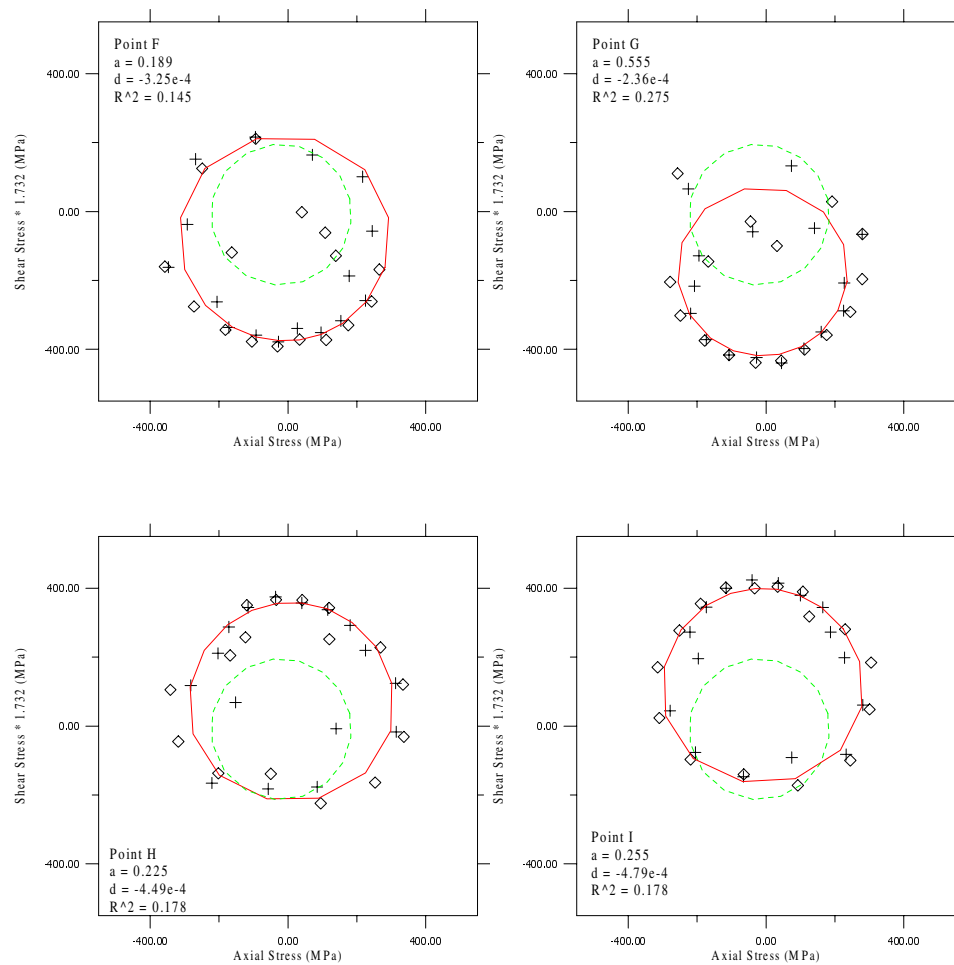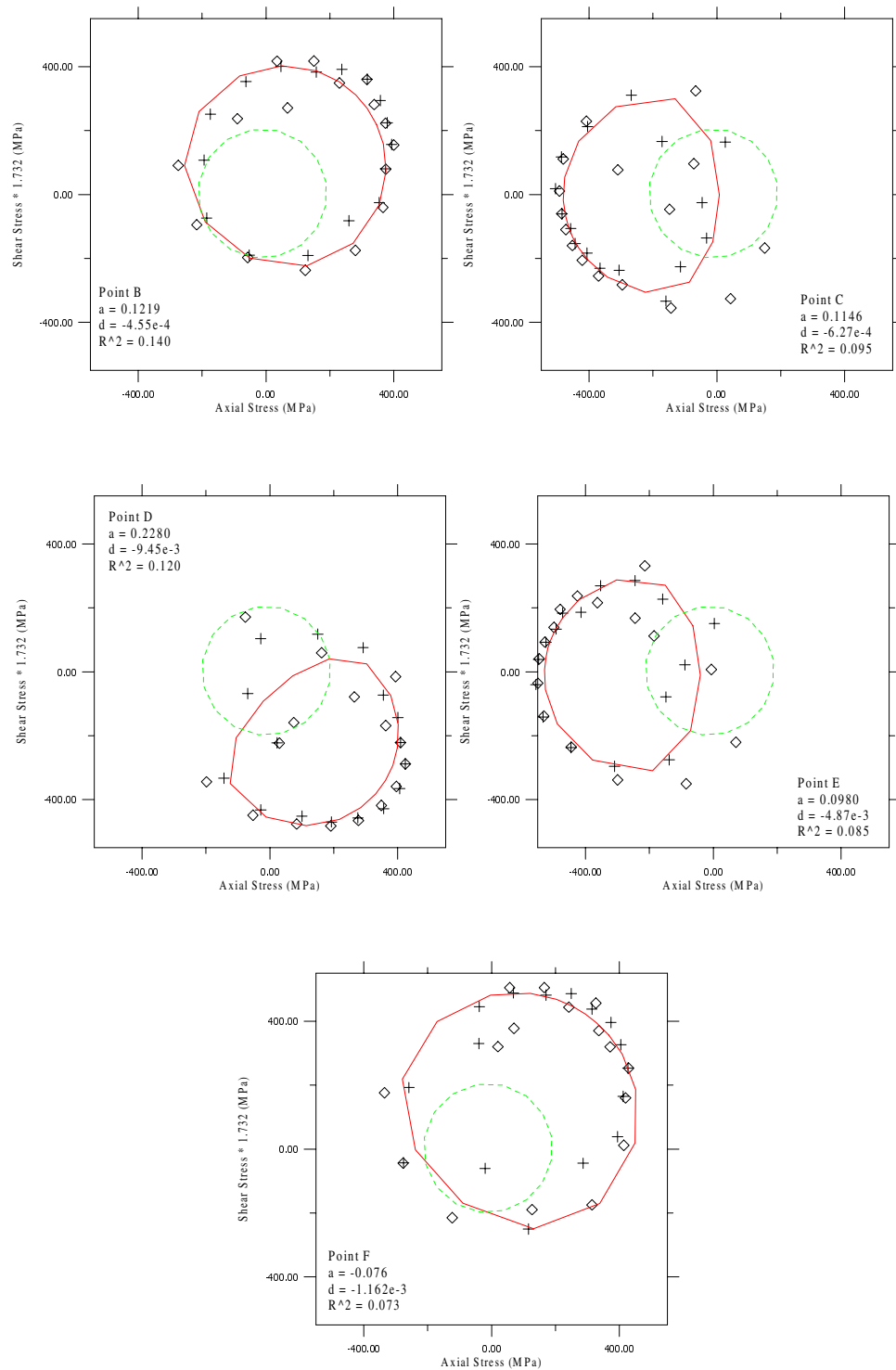
Figure A.10: Haynes 188, Path III, Points B-F, Cycle 2, HYII-90.
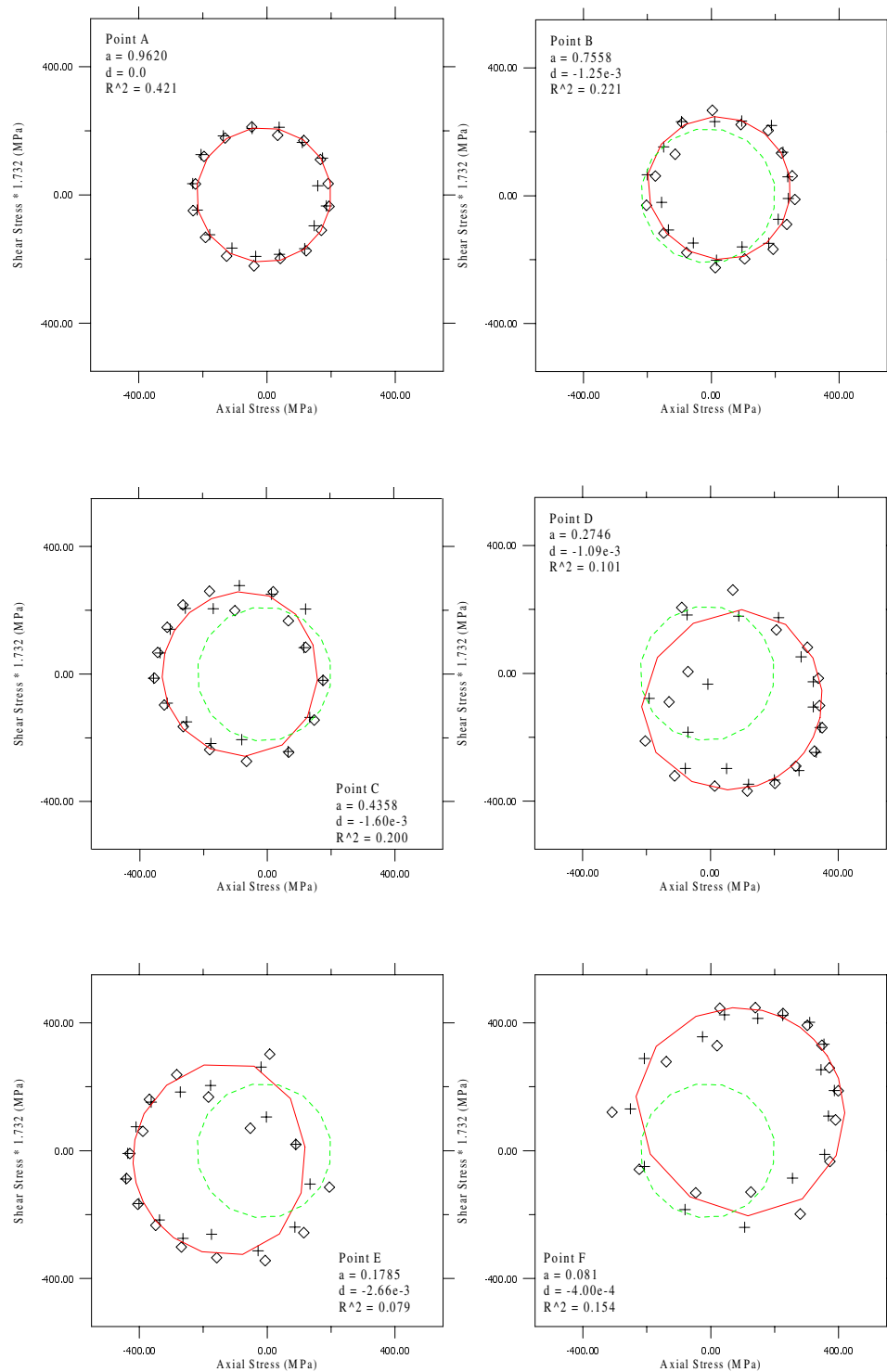
Figure A.11: Haynes 188, Path III, Points A-F, Cycle 1, HYII-82.
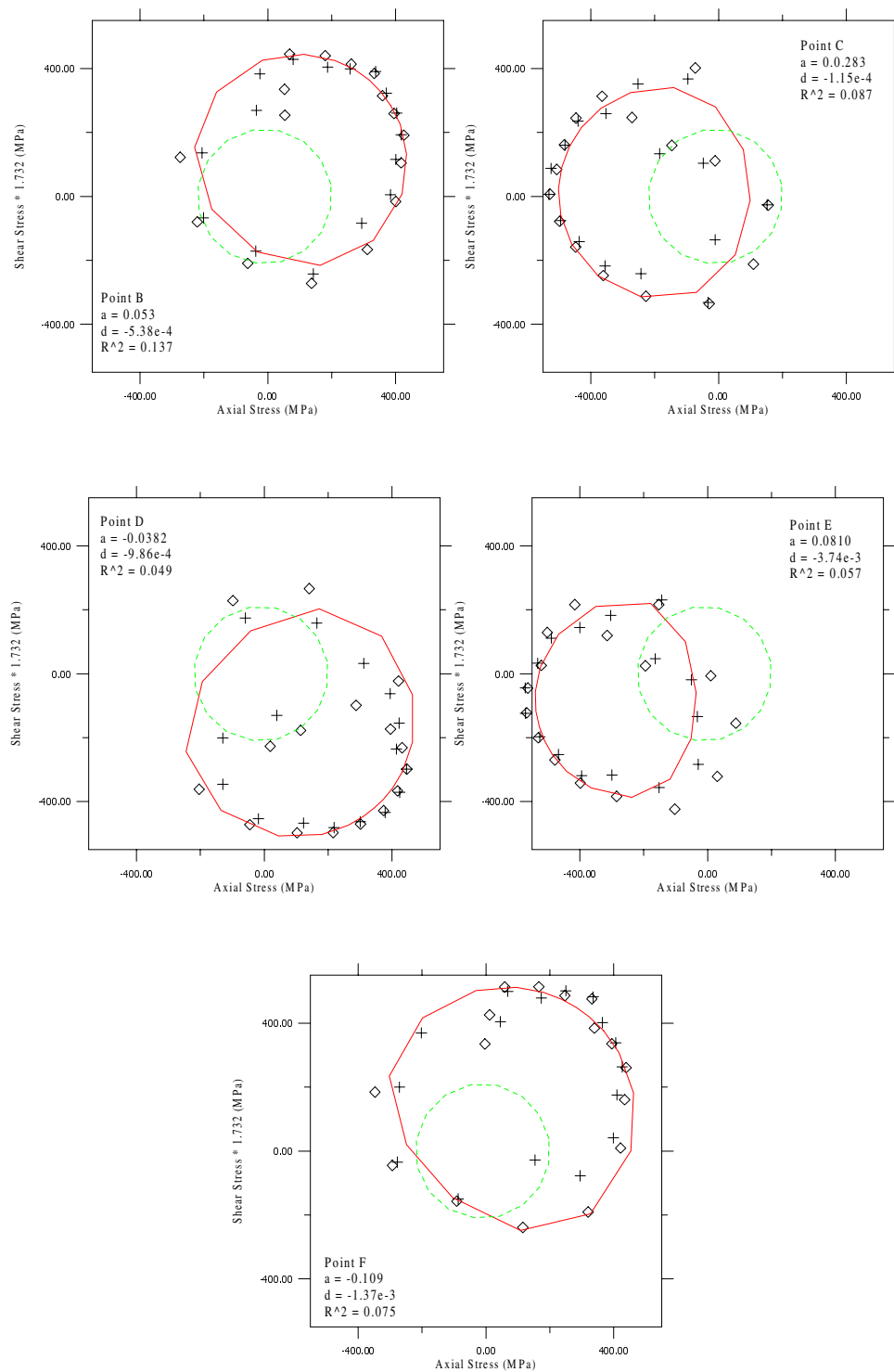
Figure A.12: Haynes 188, Path III, Points B-F, Cycle 2, HYII-82.
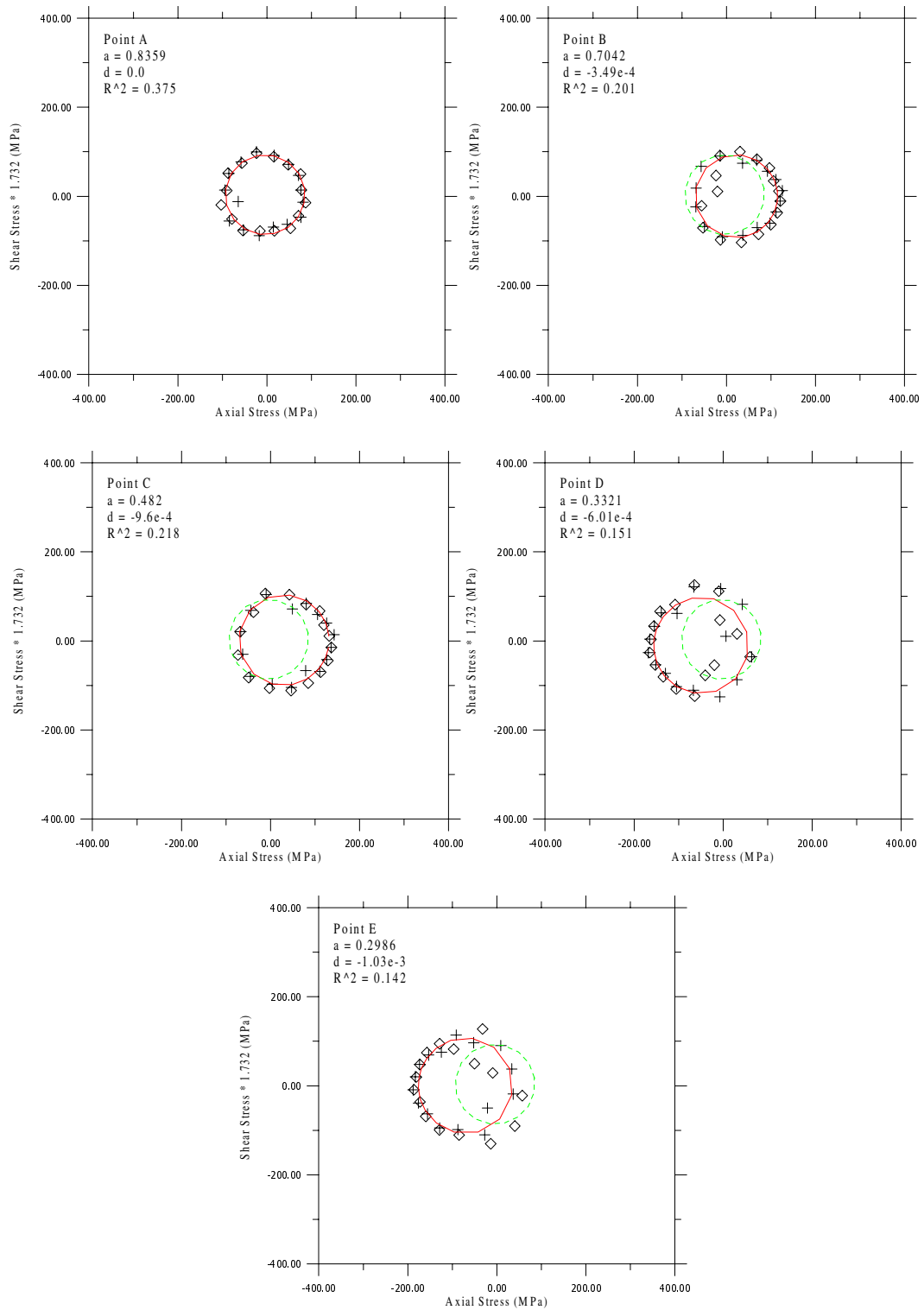
Figure A.13: 316 Stainless Steel, Path I, Points A-E, Cycle 1, 610-01.
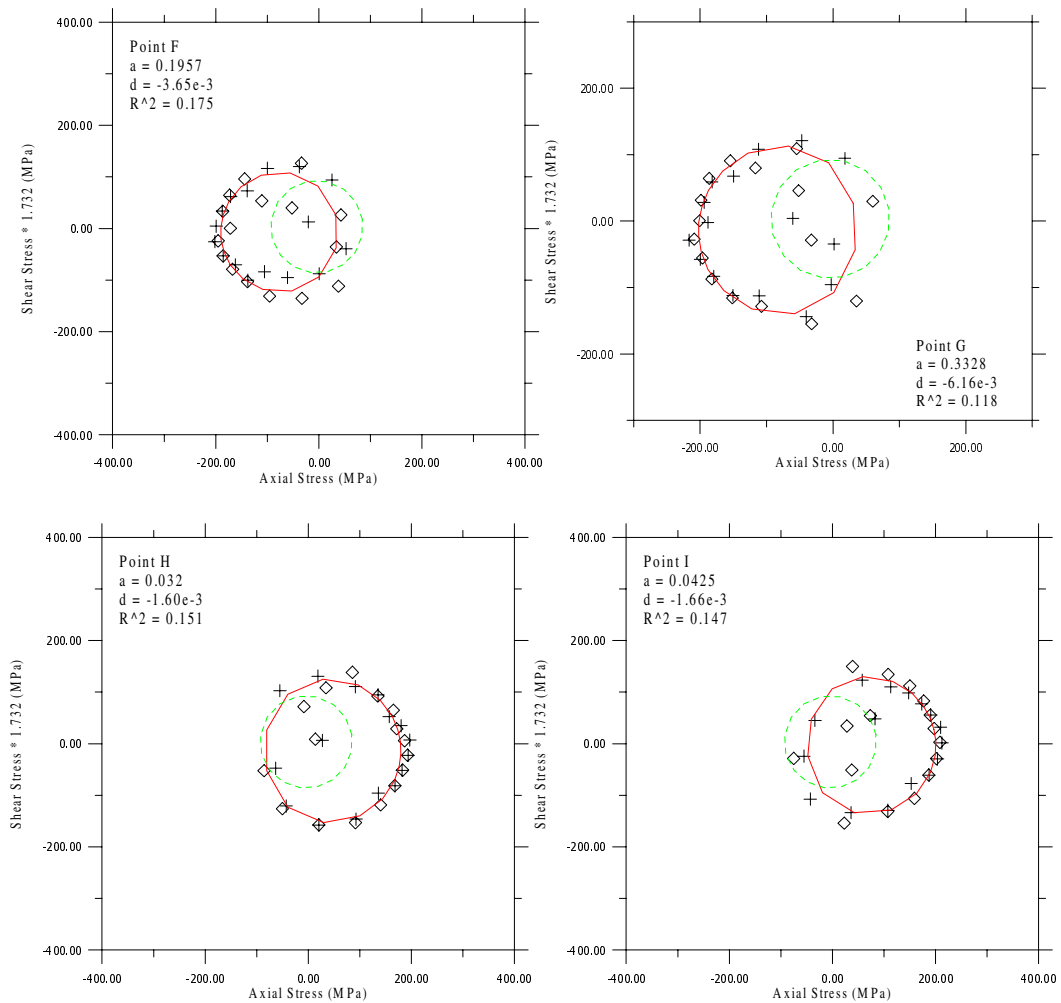
Figure A.14: 316 Stainless Steel, Path I, Points F-I, Cycle 1, 610-01.
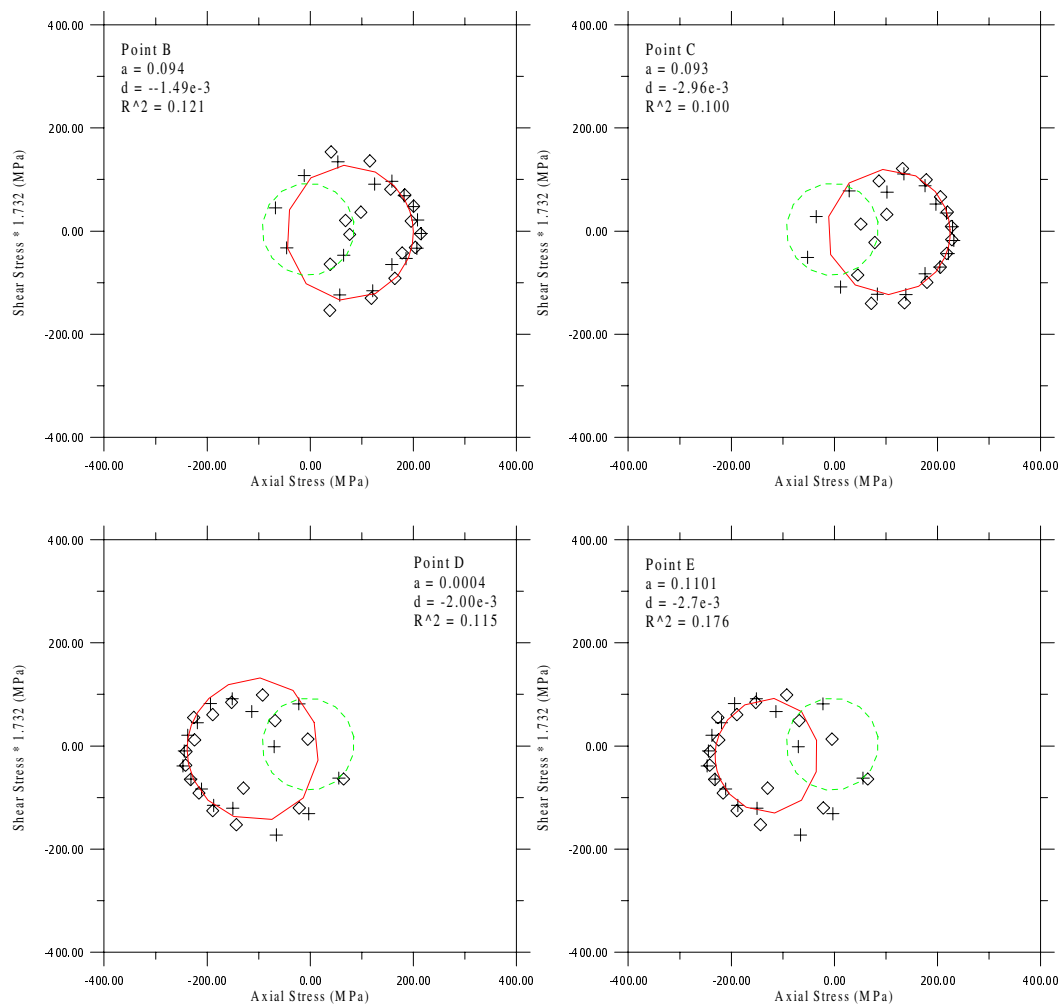
Figure A.15: 316 Stainless Steel, Path I, Points B-E, Cycle 2, 610-01.
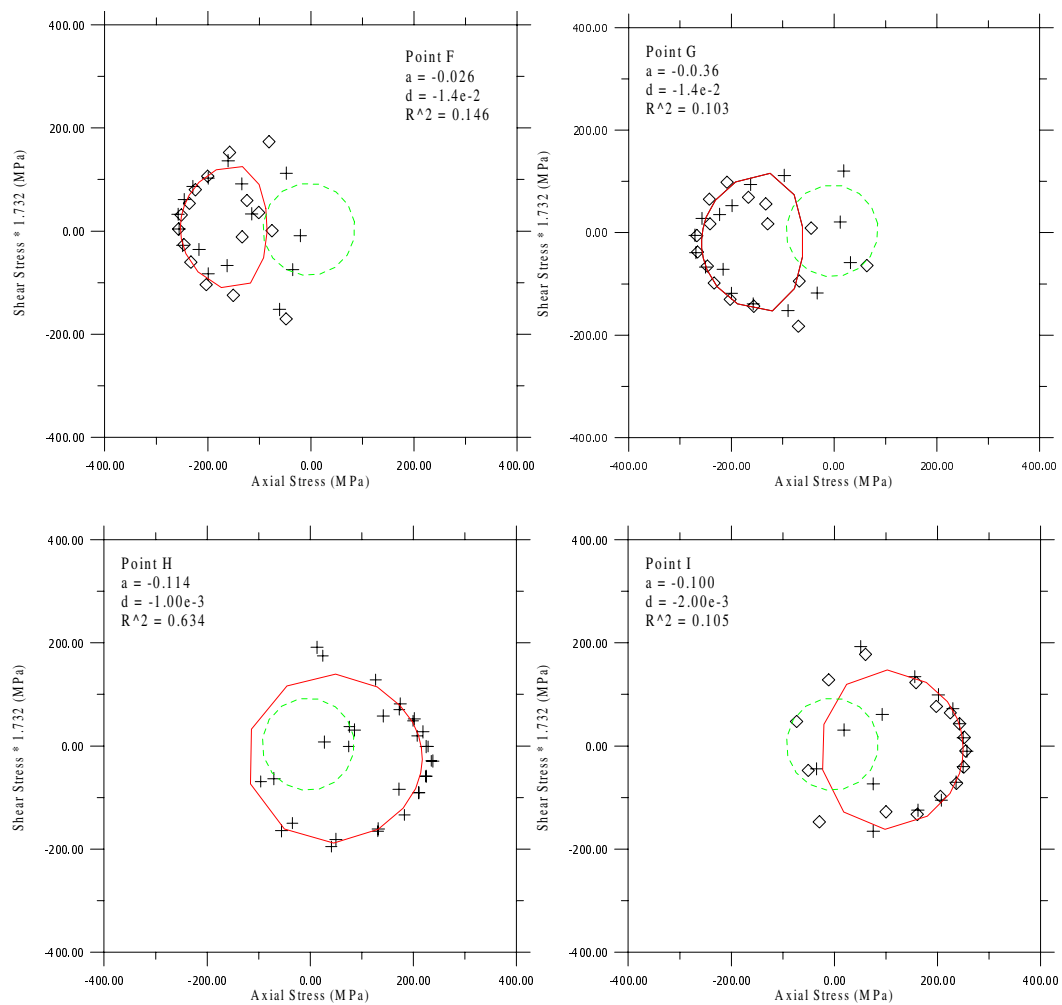
Figure A.16: 316 Stainless Steel, Path I, Points F-I, Cycle 2, 610-01.
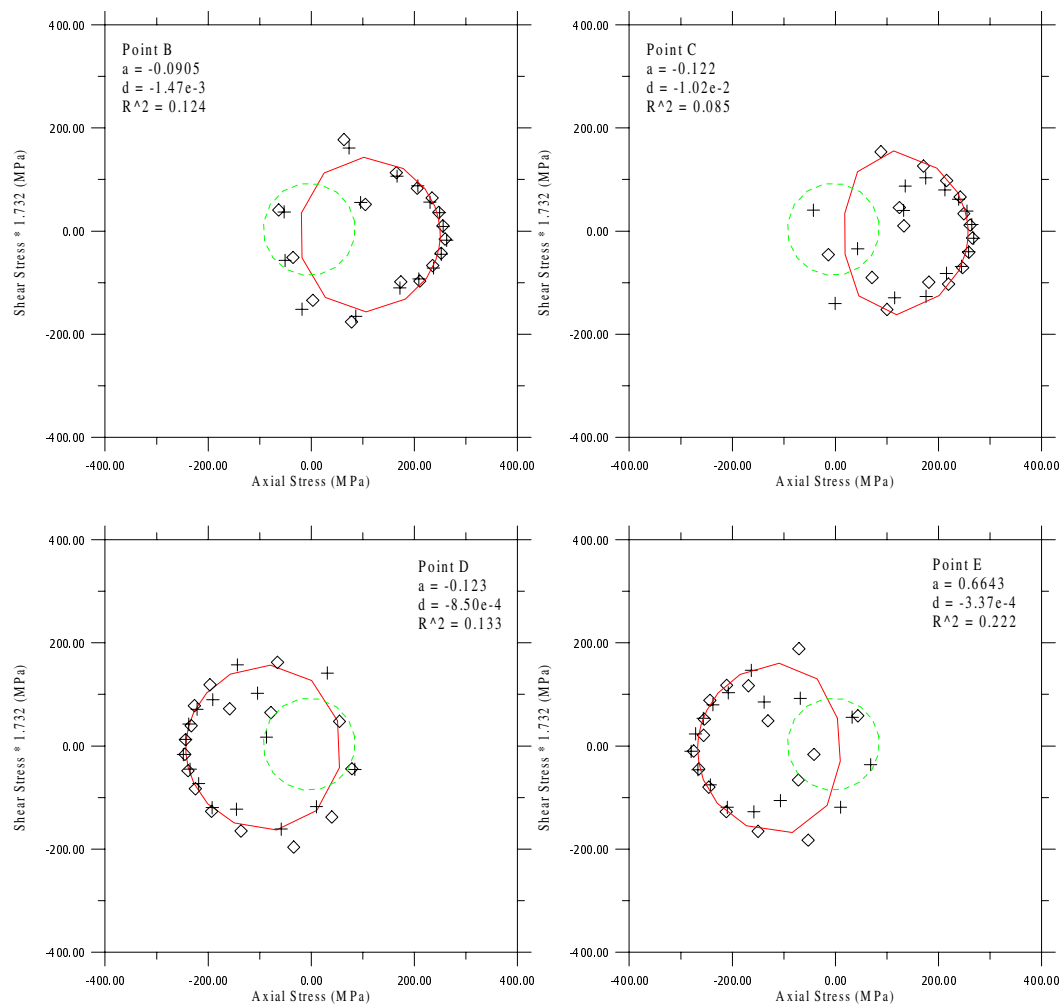
Figure A.17: 316 Stainless Steel, Path I, Points B-E, Cycle 3, 610-01.
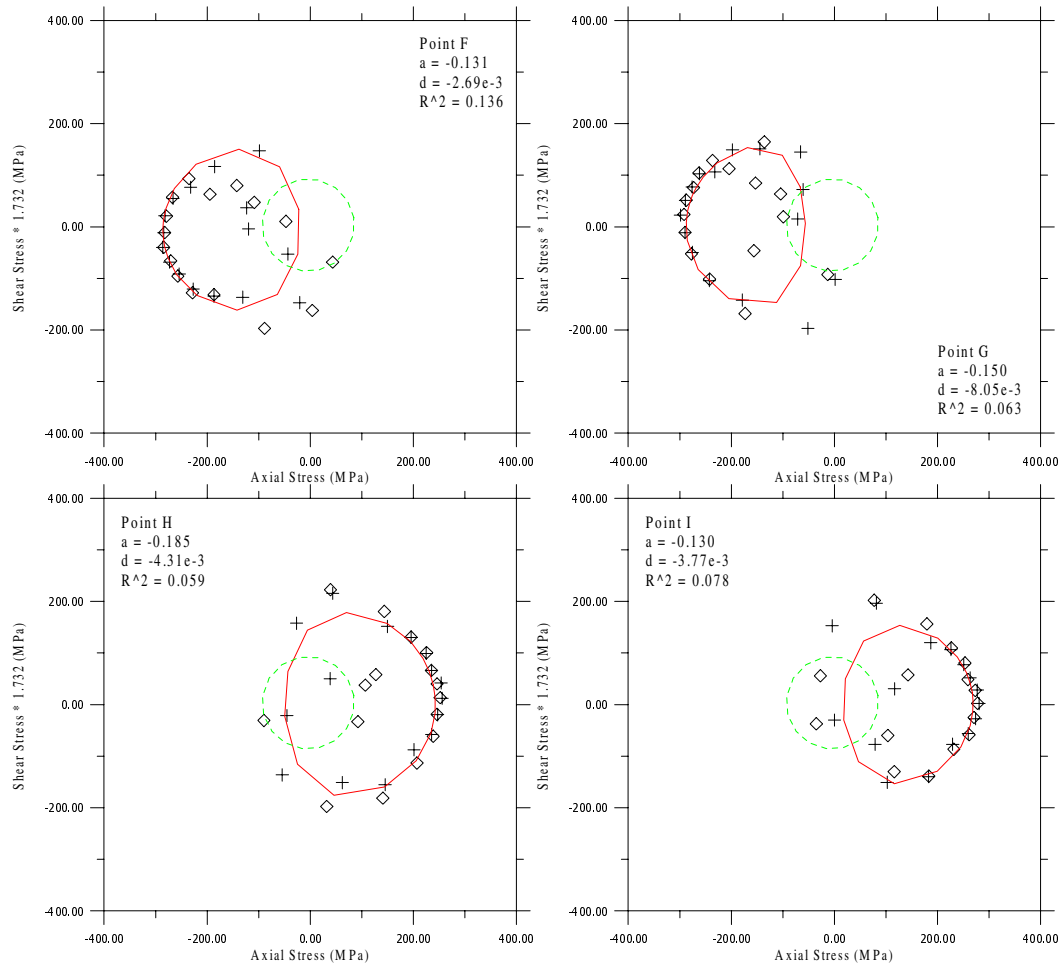
Figure A.18: 316 Stainless Steel, Path I, Points F-I, Cycle 3, 610-01.
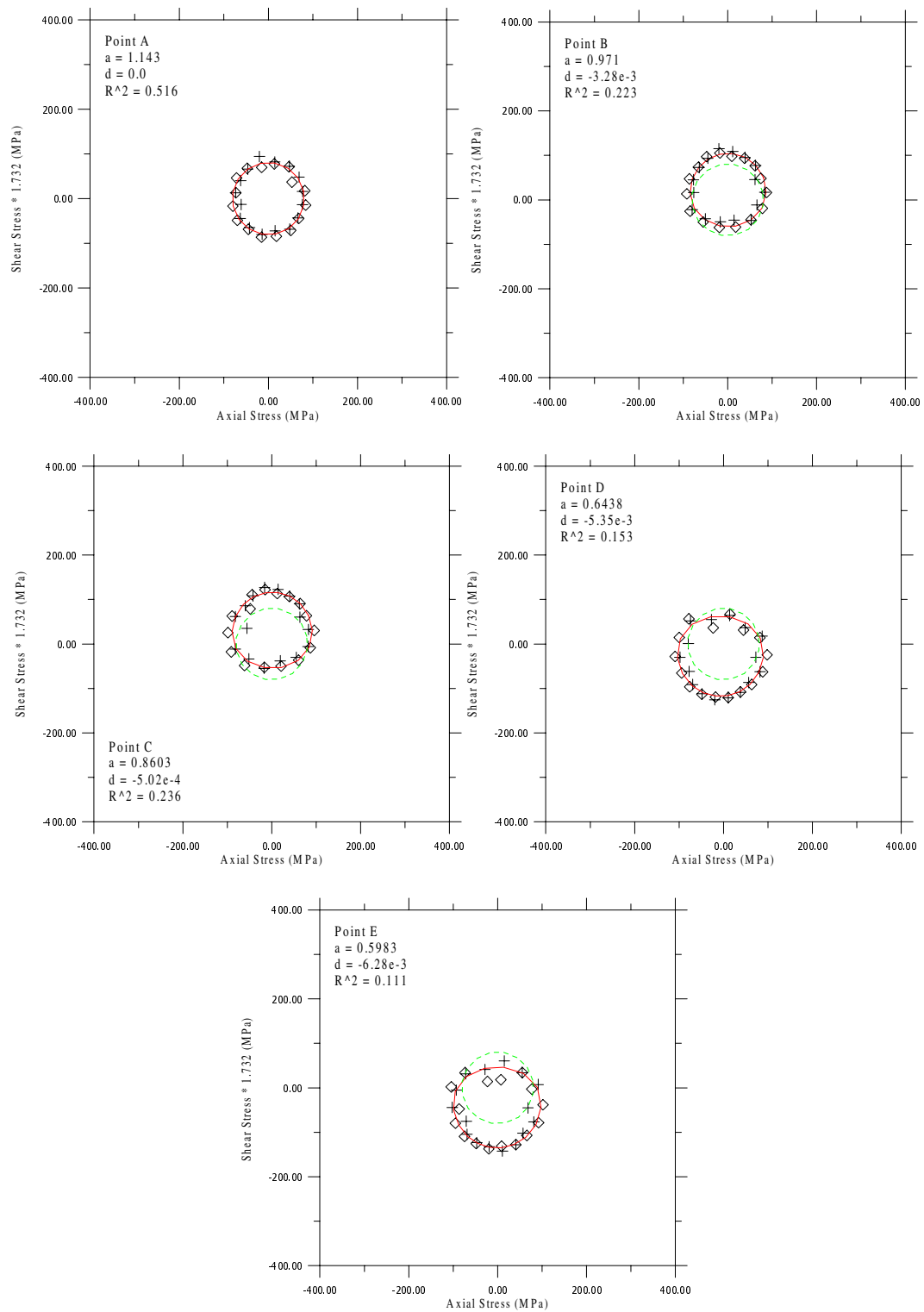
Figure A.19: 316 Stainless Steel, Path II, Points A-E, Cycle 1, 610-04.
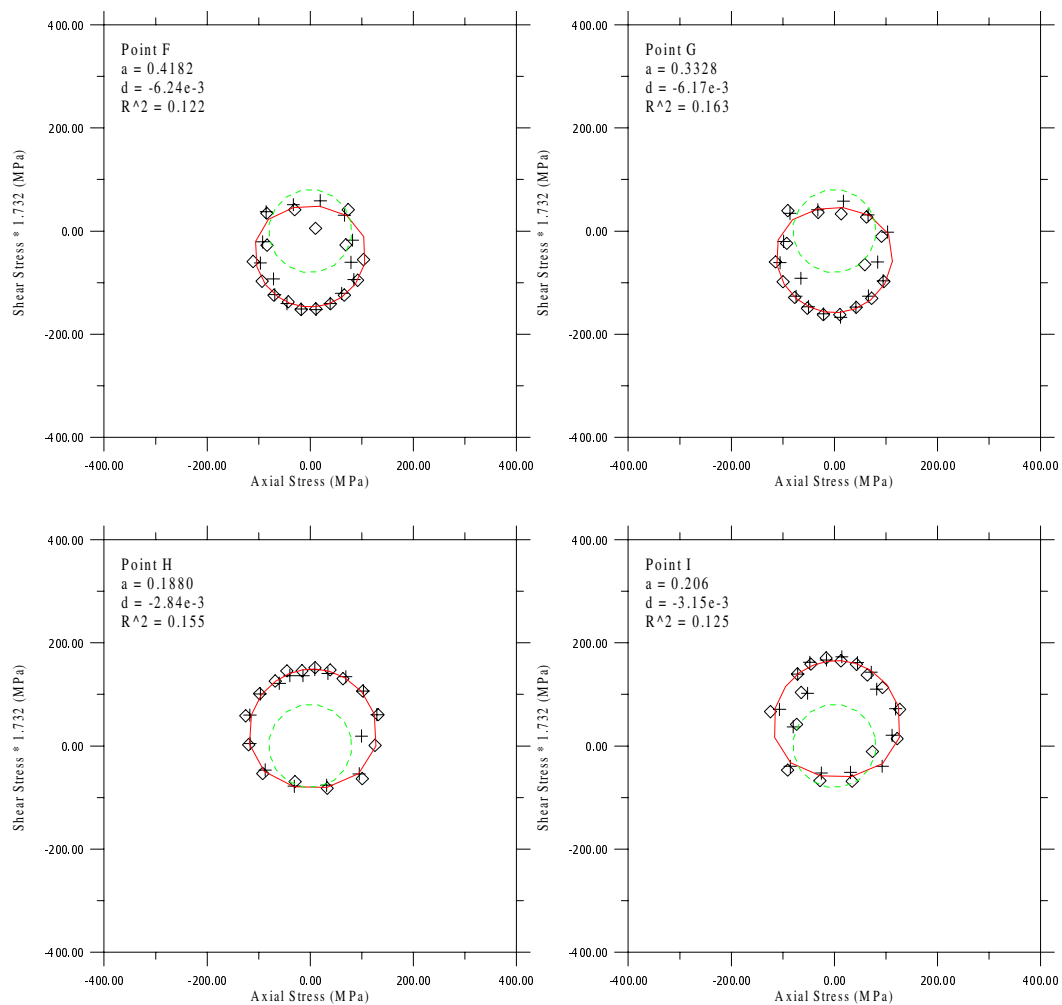
Figure A.20: 316 Stainless Steel, Path II, Points F-I, Cycle 1, 610-04.
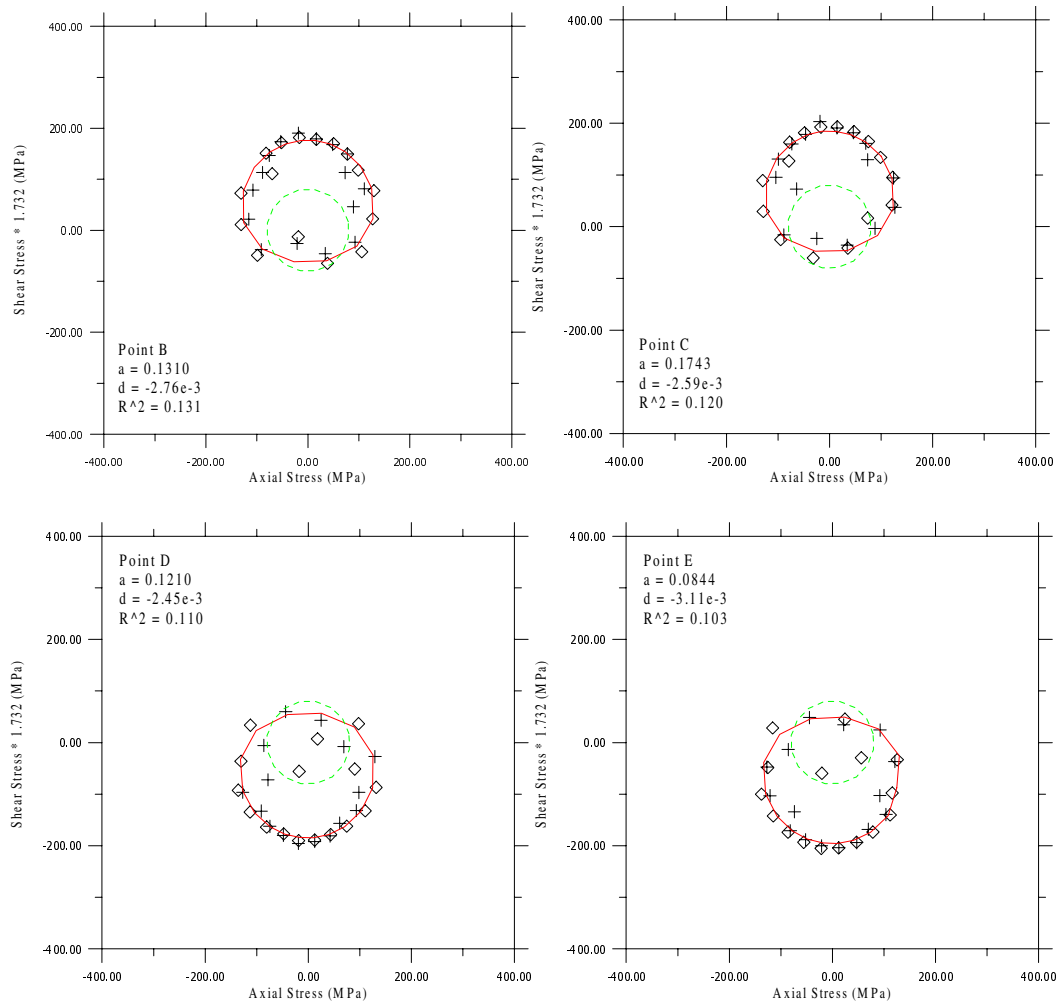
Figure A.21: 316 Stainless Steel, Path II, Points B-E, Cycle 2, 610-04.
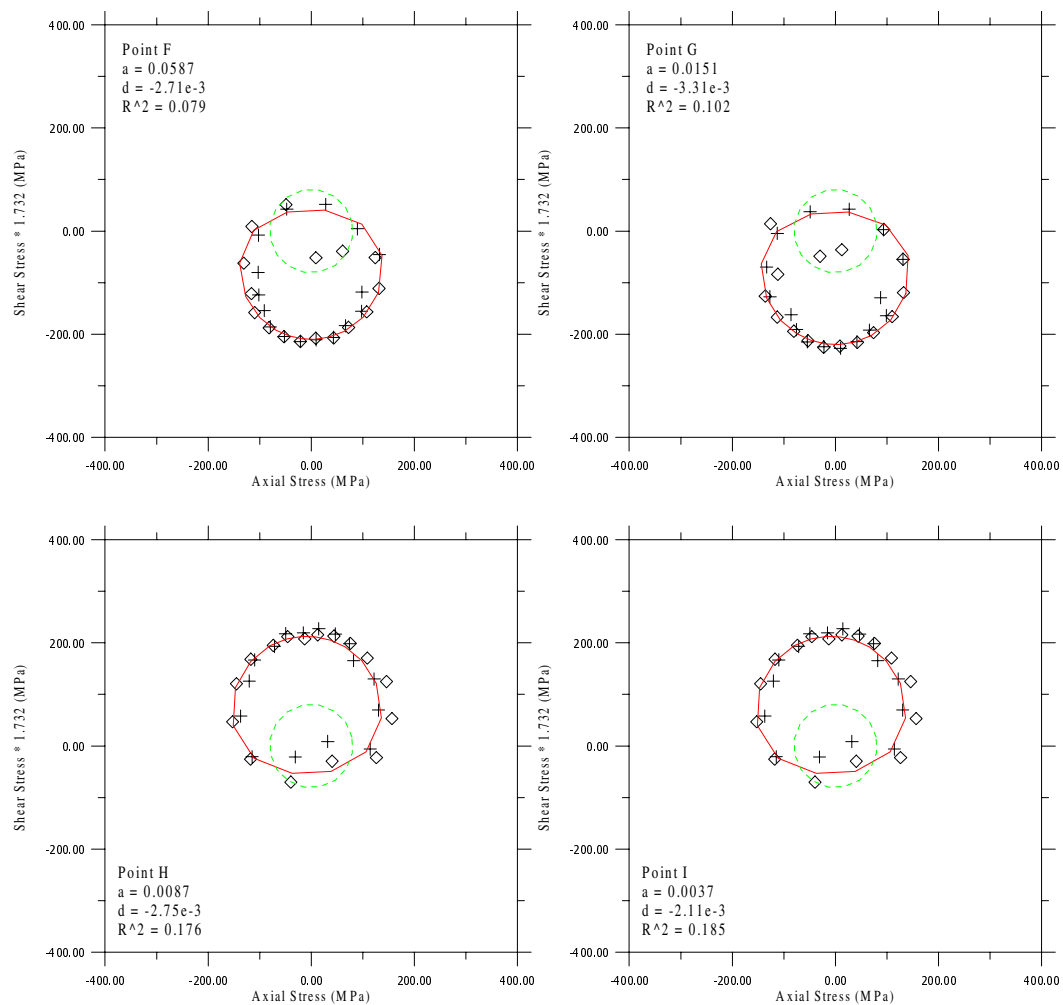
Figure A.22: 316 Stainless Steel, Path II, Points F-I, Cycle 2, 610-04.
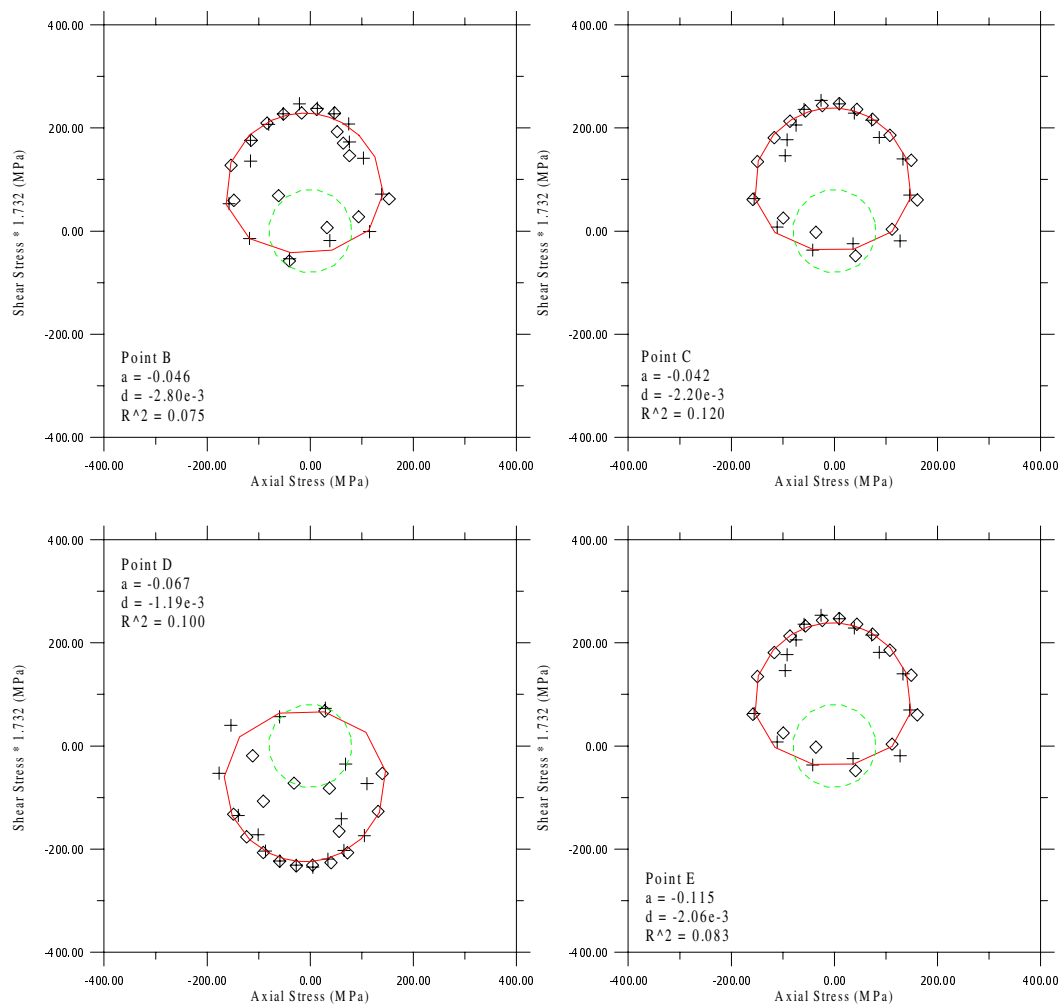
Figure A.23: 316 Stainless Steel, Path II, Points B-E, Cycle 3, 610-04.
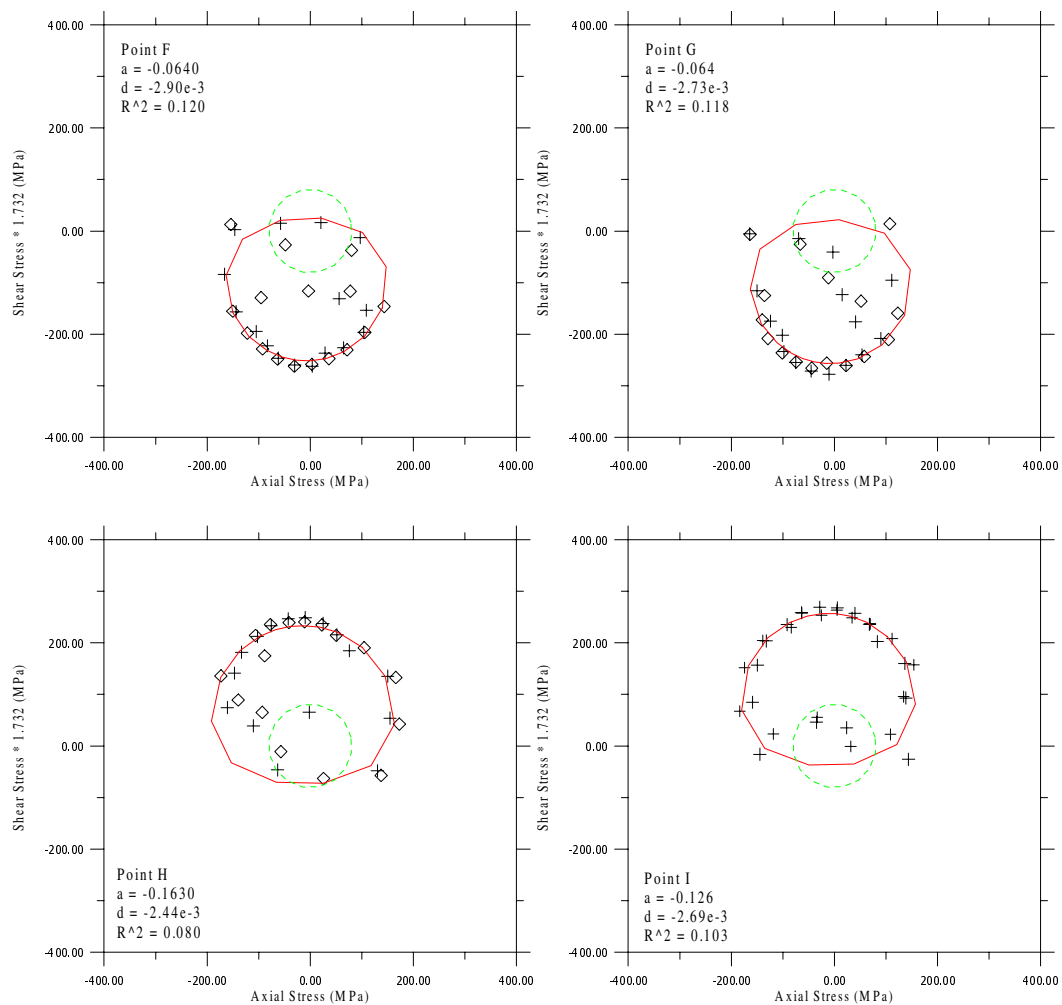
Figure A.24: 316 Stainless Steel, Path II, Points F-I, Cycle 3, 610-04.
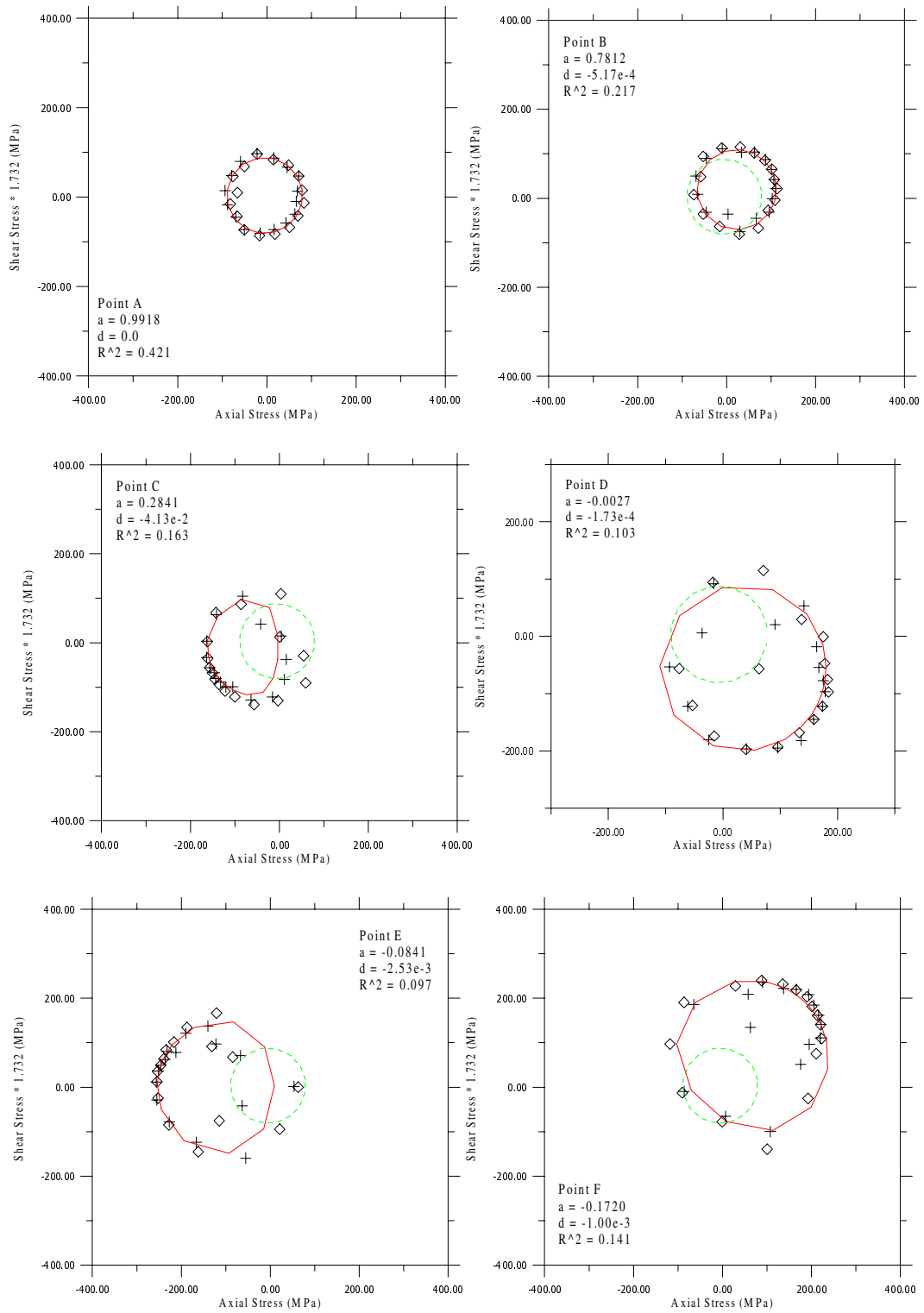
Figure A.25: 316 Stainless Steel, Path III, Points A-F, Cycle 1, 610-05.
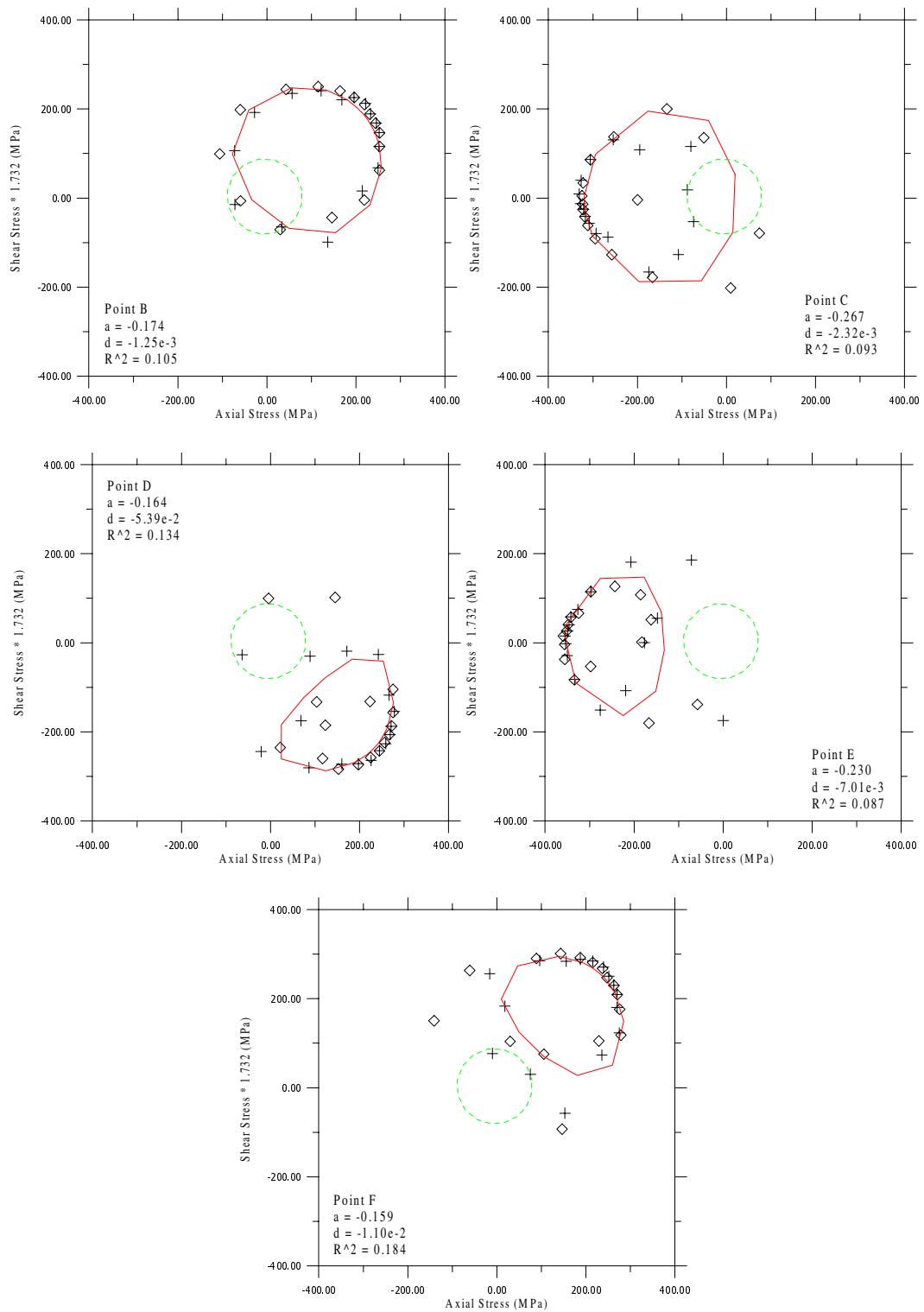
Figure A.26: 316 Stainless Steel, Path III, Points B-F, Cycle 2, 610-05.
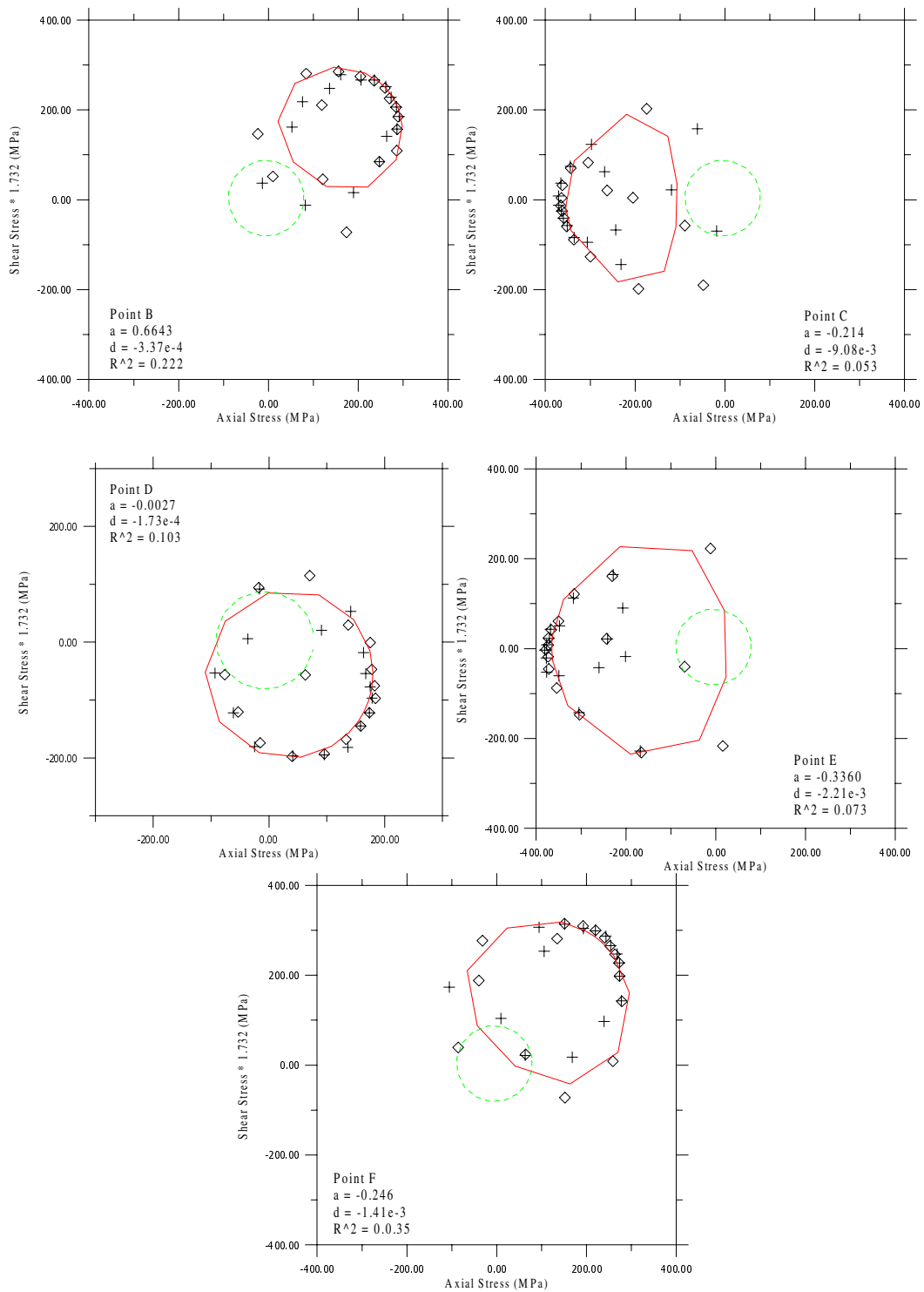
Figure A.27: 316 Stainless Steel, Path III, Points B-F, Cycle 3, 610-05.
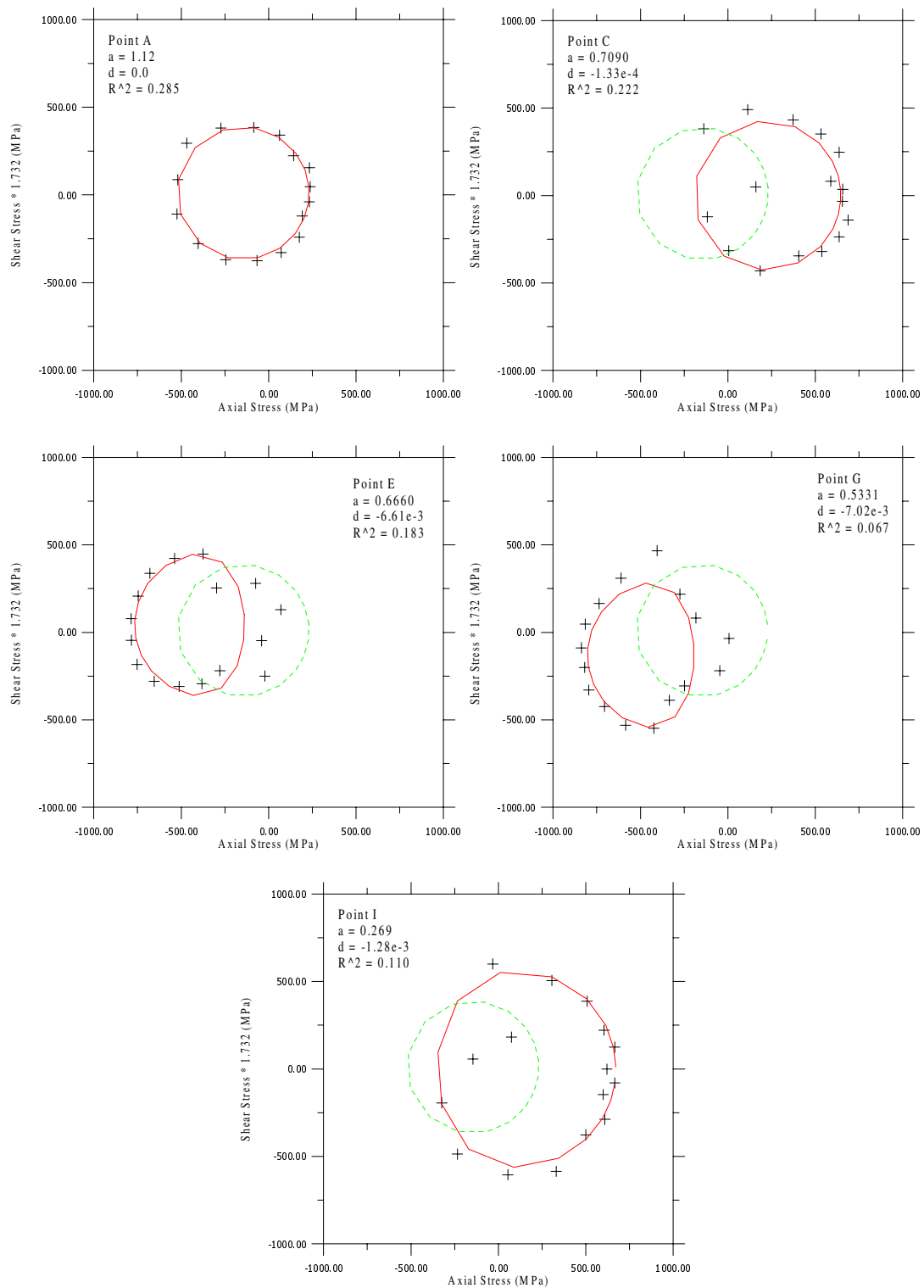
Figure A.28: Inconel 718, Path I, Points A-I, Cycle 1, IN-16.
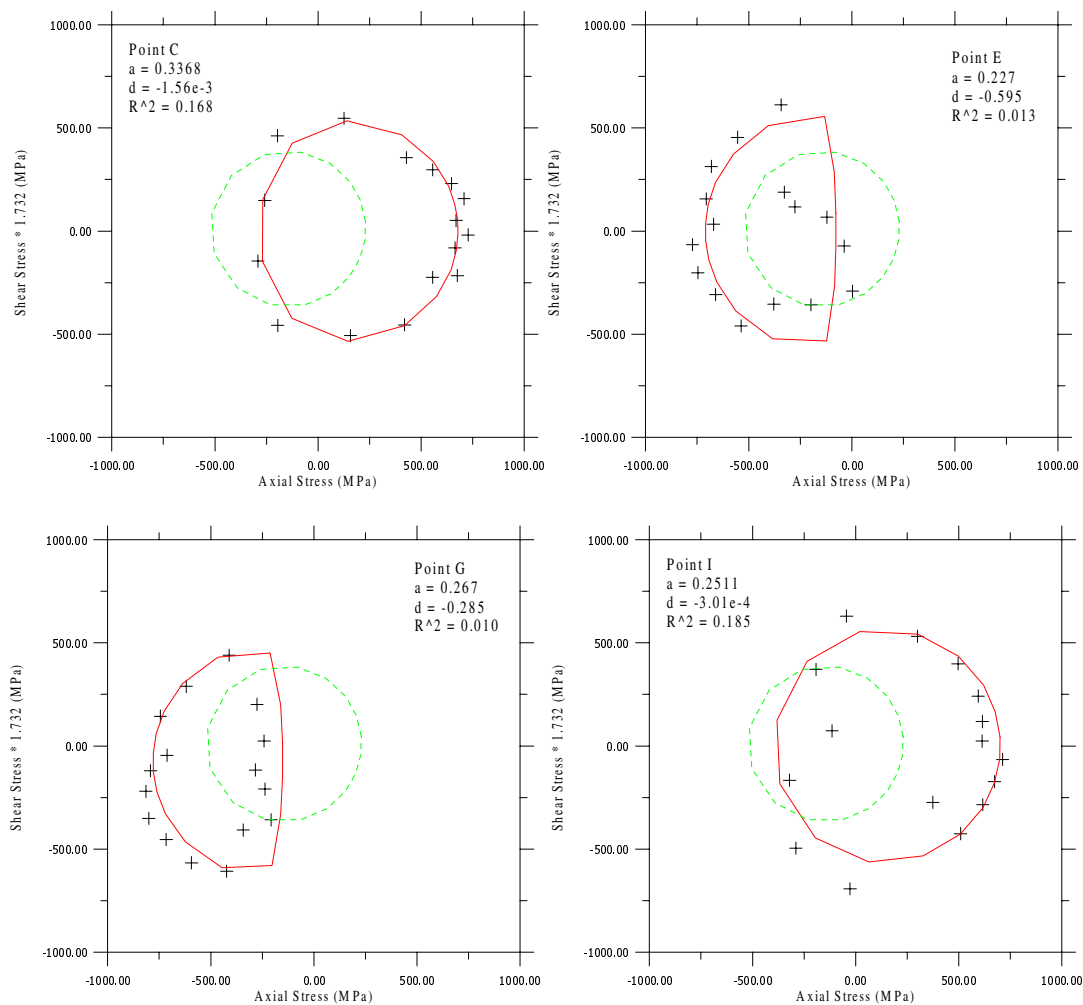
Figure A.29: Inconel 718, Path I, Points C-I, Cycle 2, IN-16.
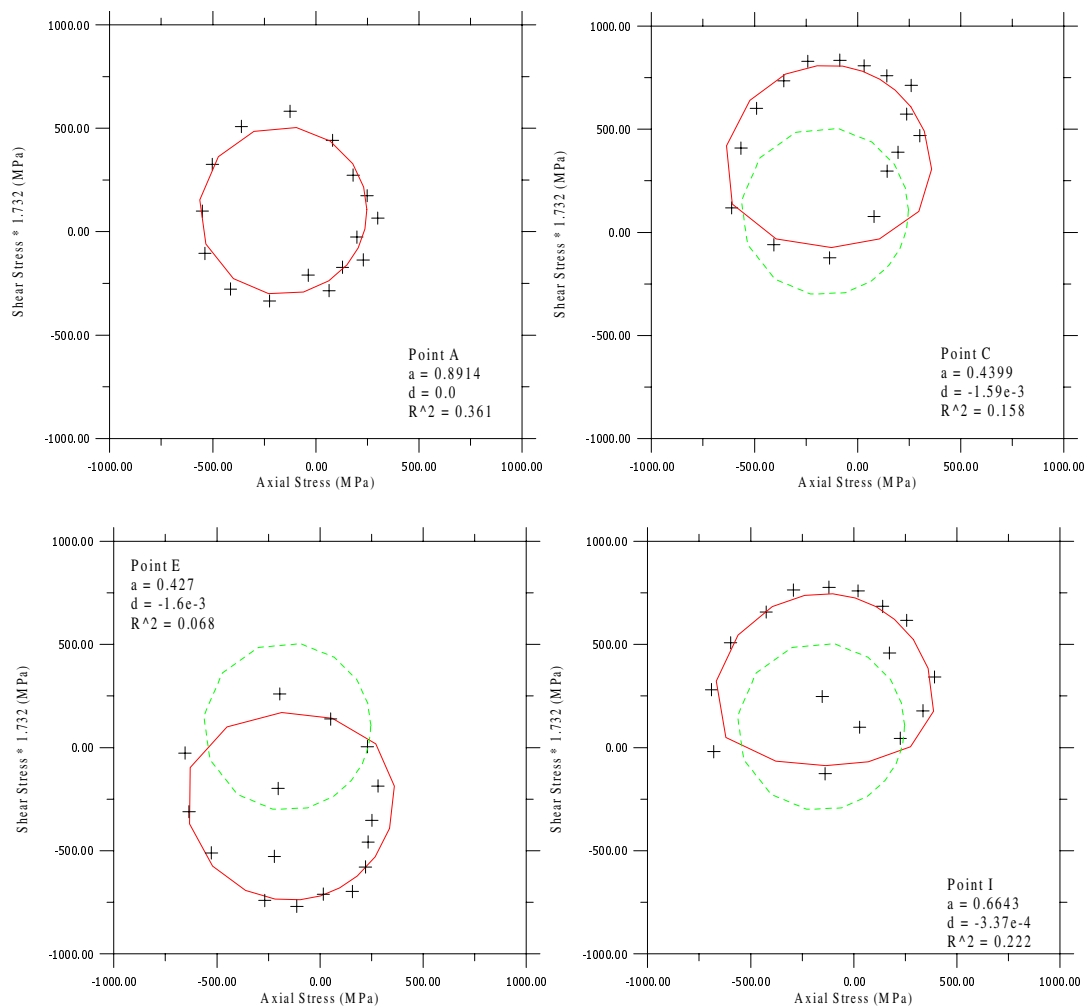
Figure A.30: Inconel 718, Path II, Points A-I, Cycle 1, IN-23.
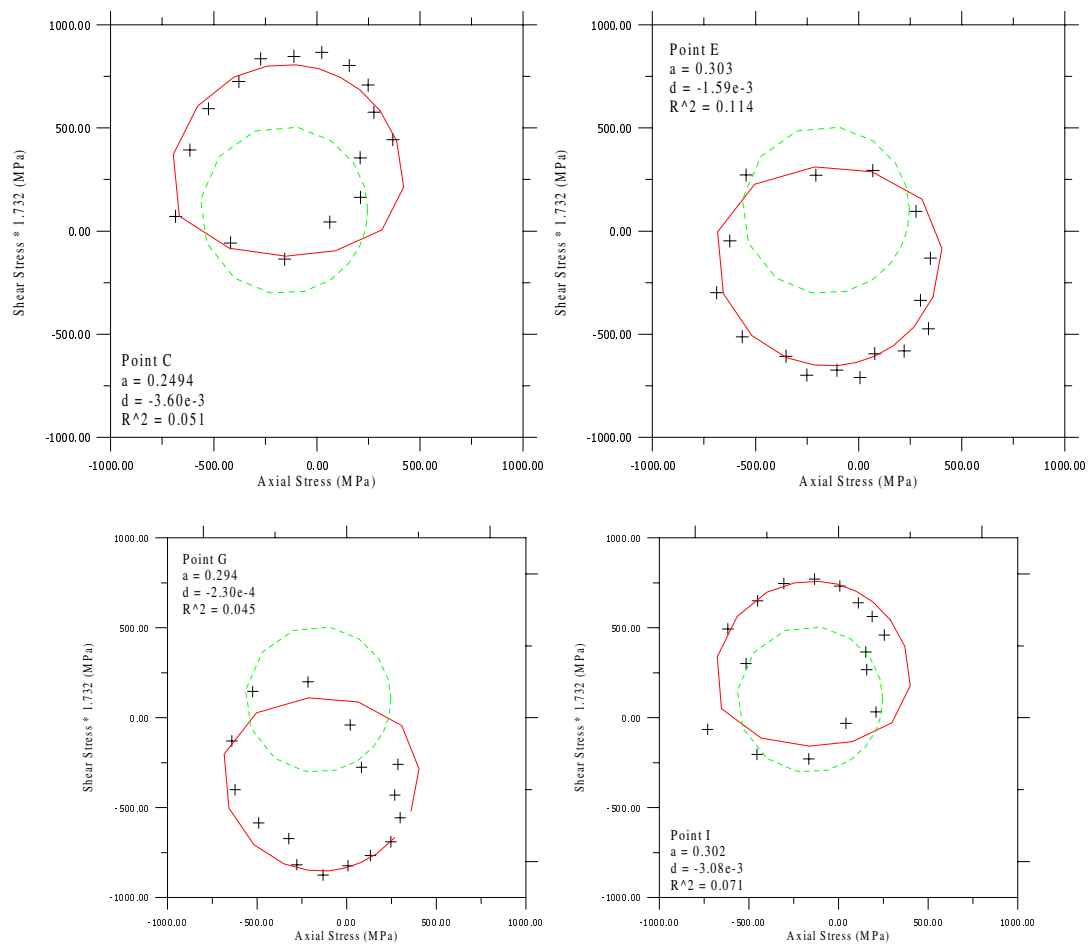
Figure A.31: Inconel 718, Path II, Points A-I, Cycle 2, IN-23.
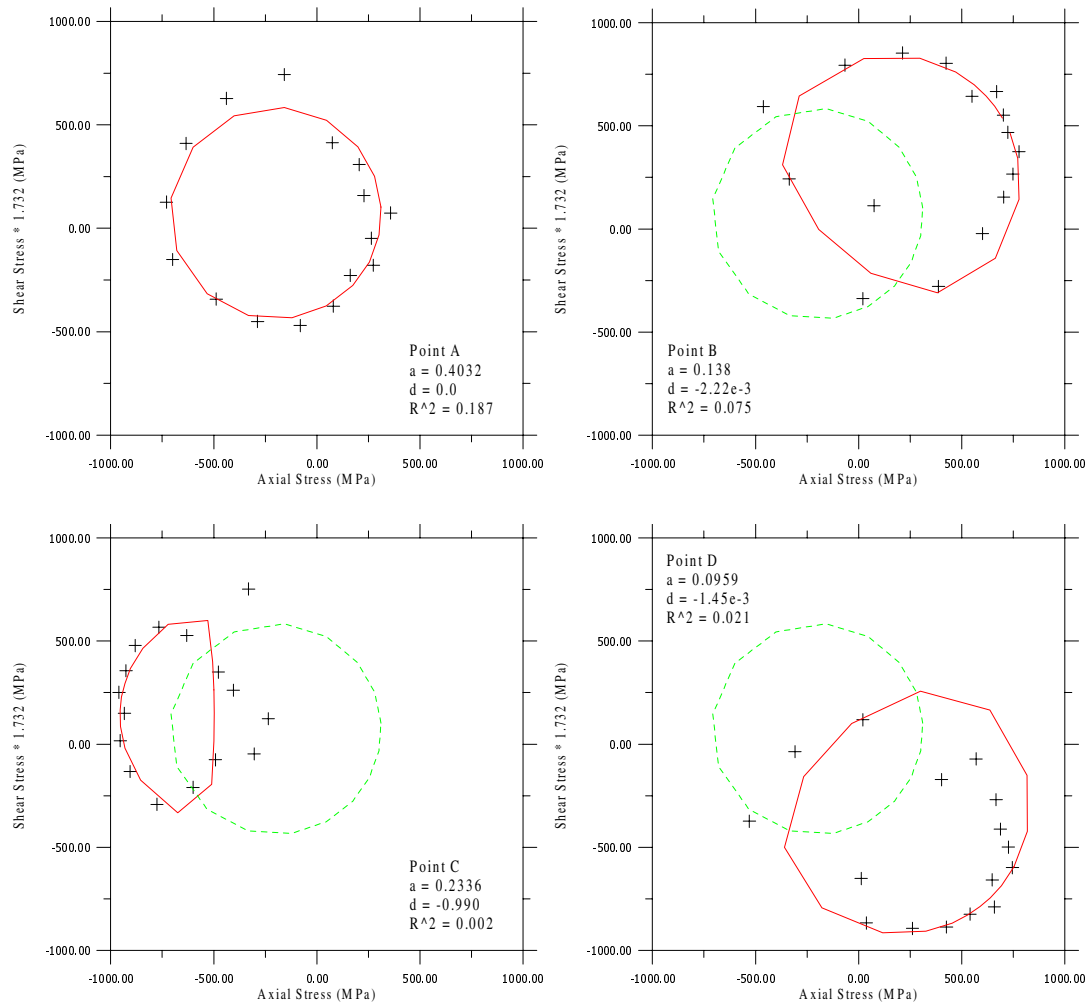
Figure A.32: Inconel 718, Path III, Points A-D, Cycle 1.
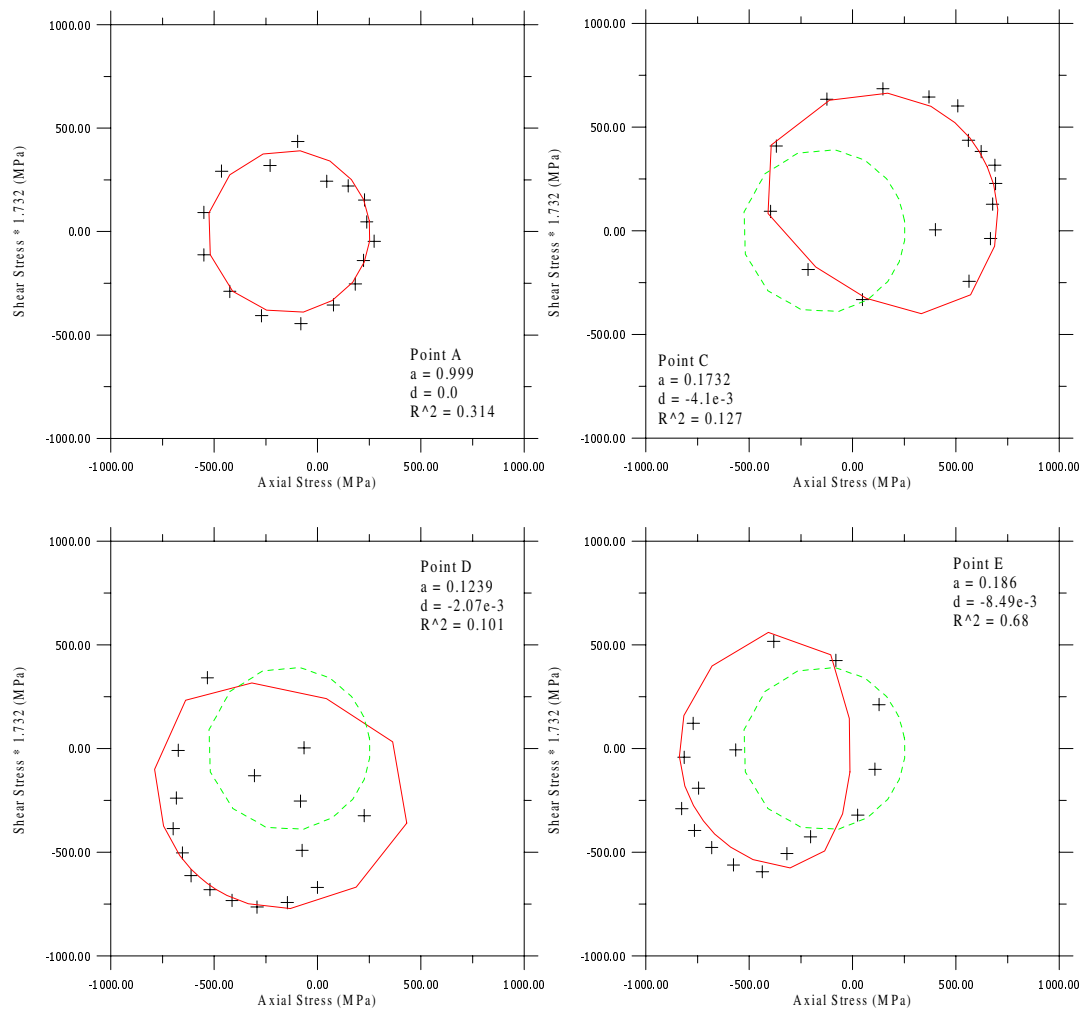
Figure A.33: Inconel 718, Path IV, Points A-E, Cycle 1.

Appendix B

Yield Surface Fit Data

Cycle	Point	σ (MPa)	ε (m/m)	a	d	α11	α12
1	A	0	0	0.8077	0	0	0
1	C	314	0.015	0.6428	-6.30E-05	49	-8
1	E	-348	-0.0013	0.4289	-1.60E-04	-94	-10
1	G	-422	-0.015	0.2691	-4.10E-05	-120	-8
1	I	406	0.0013	0.2308	-8.90E-05	73	-14
2	C	424	0.015	0.202	-9.04E-05	101	-7
2	E	-445	-0.0013	0.1663	-1.00E-04	-131	-5
2	G	-489	-0.015	0.1238	-9.80E-05	-176	-11
2	I	458	0.0012	0.058	-3.21E-04	90	-10

Table B.1: Haynes 188, Path I, HYII-89.

Cycle	Point	τ (MPa)	γ (m/m)	a	d	$\alpha11$	$\alpha12$
1	A	0	0	1.044	0	-20	-5
1	B	169.8	5.41E-03	0.737	-1.30E-04	0	33
1	C	186	1.09E-02	0.664	-3.37E-04	-2	38
1	D	-175	5.42E-03	0.719	-5.85E-04	-5	-43
1	E	-185	-7.65E-04	0.628	-2.43E-04	-4	-49
1	F	-205	-5.45E-03	0.596	-4.36E-04	-10	-53
1	G	-217	-1.09E-02	0.477	-5.48E-04	-10	-45
1	H	190.6	-5.47E-03	0.429	-3.68E-04	-5	34
1	I	220.8	6.91E-04				
2	B	215	5.41E-03	0.351	-2.71E-04	-10	49
2	C	231	1.09E-02	0.354	-3.15E-04	-10	59
2	D	-206	5.42E-03	0.417	-1.51E-02	-10	-52
2	E	-218	-7.51E-04	0.464	-4.19E-04	-10	-55
2	F	-229	-5.24E-03	0.189	-3.25E-04	-10	-40
2	G	-258	-1.09E-02	0.555	-2.36E-04	-10	-99
2	H	210	-5.47E-03	0.225	-4.49E-04	10	35
2	I	246	-7.05E-04	0.255	-4.79E-04	-10	62
3	B	255	5.40E-03	0.223	-4.17E-04	-15	54
3	C	256	1.19E-02	0.1556	-4.80E-04	-10	51
3	D	-230	6.35E-03	0.1845	-3.40E-04	10	-34
3	E	-254	7.00E-06	0.4737	-4.80E-04	1	-110
3	F	-268	-4.50E-03				
3	G	-279	-9.96E-03	0.4391	-1.60E-03	0	-117
3	H	219	-4.55E-03	0.1385	-7.50E-04	0	10
3	I	267	1.88E-03	0.1318	-6.30E-04	-10	51

Table B.2: Haynes 188, Path II, HYII-86.

Cycle	Point	σ (MPa)	ε (m/m)	τ (MPa)	γ (m/m)	a	d	α11	α12
1	A	0	0	0	0	1.086	0	0	0
1	B	225	0.0106	105	0.0077	0.7768	-3.90E-04	25.5	14.7
1	C	-364	-0.0106	37	0.0077	0.4822	-3.63E-03	-78	2
1	D	305	0.0106	-174	-0.0076	0.3152	-1.16E-04	57.5	-56
1	E	-454	-0.0106	-32	-0.0076	0.3105	-3.60E-03	-123	-7
1	F	322	0.0008	202	0.0006				
2	B	358	0.0106	196	0.0077	0.1219	-4.55E-04	56	48
2	C	-507	-0.0106	35	0.0077	0.1146	-6.27E-04	-170	0
2	D	389	0.0106	-240	-0.0076	0.228	-9.46E-05	112	-115
2	E	-572	-0.0106	-40	-0.0076	0.098	-4.87E-03	-210	-20
2	F	376	0.0008	254	0.0006	-0.076	-1.16E-03	70	75

Table B.3: Haynes 188, Path III (First Run), HYII-90.

Cycle	Point	σ (MPa)	ε (m/m)	τ (MPa)	γ (m/m)	a	d	α11	α12
1	A	0	0	0	0	0.962	0	-10	0
1	B	227	0.0106	106	0.0077	0.7558	-1.25E-03	22	12
1	C	-367	-0.0106	21	0.0077	0.4358	-1.06E-03	-72	0
1	D	314	0.0106	-168	-0.0076	0.2746	-1.09E-03	62	-59
1	E	-446	-0.0106	-23	-0.0076	0.1785	-2.66E-03	-111	-10
1	F	320	0.0008	209	0.0006	0.081	-4.00E-04	86	73
2	B	384	0.0106	208	0.0077	0.053	-5.38E-04	97	77
2	C	-546	-0.0106	33	0.0077	0.0283	-1.15E-03	-168	10
2	D	416	0.0106	-246	-0.0076	-0.038	-9.86E-04	100	-110
2	E	-589	-0.0106	-45	-0.0076	0.081	-3.74E-03	-228	-60
2	F	383	0.0008	270	0.0006	-0.109	-1.37E-03	84	87

Table B.4: Haynes 188, Path III (Second Run), HYII-82.

Cycle	Point	σ (MPa)	ε (m/m)	a	d	α11	α12
1	A	0	0	0.8359	0	-4	0
1	B	130	0.0075	0.7042	-3.49E-04	22	0
1	C	150	0.015	0.482	-9.60E-04	29	1
1	D	-175	0.0075	0.3321	-6.01E-04	-48	-6
1	E	-195	-0.0006	0.2986	-1.03E-03	-58	0
1	F	-209	-0.0075	0.1957	-3.65E-03	-64	-4
1	G	-221	-0.015	0.083	-1.40E-03	-62	-8
1	H	206	-0.0075	0.032	-1.60E-03	40	-8
1	I	216	0.0006	0.0425	-1.66E-03	65	-2
2	B	231	0.0075	0.094	-1.49E-03	71	-2
2	C	244	0.015	0.093	-2.96E-03	90	-1
2	D	-232	0.0075	0.004	-2.00E-03	-100	-4
2	E	-257	-0.0006	0.1101	-2.70E-03	-120	-11
2	F	-270	-0.0075	-0.0026	-1.69E-03	-118	4
2	G	-269	-0.015	-0.036	-1.40E-02	-120	-11
2	H	245	-0.0075	-0.114	-1.00E-03	40	0
2	I	269	0.0006	-0.1	-2.00E-03	95	-4
3	B	275	0.0075	-0.0905	-1.47E-03	100	-4
3	C	283	0.015	-0.122	-1.02E-02	102	-2
3	D	-260	0.0075	-0.123	-8.50E-04	-83	-2
3	E	-294	-0.0006	-0.141	-2.37E-03	-106	-3
3	F	-298	-0.0075	-0.131	-2.69E-03	-120	1
3	G	-308	-0.015	-0.15	-8.05E-03	-125	0
3	H	266	-0.0075	-0.185	-4.31E-03	64	0
3	I	296	0.0006	-0.13	-3.77E-03	114	0

Table B.5: 316 Stainless Steel, Path I, 610-01.

Cycle	Point	τ (MPa)	γ (m/m)	a	d	$\alpha 11$	$\alpha 12$
1	A	0	0	1.143	0	0	0
1	B	70	5.40E-03	0.971	-3.28E-03	1	11
1	C	75	1.08E-02	0.8603	-5.02E-03	0	17
1	D	-77	5.40E-03	0.6438	-5.35E-03	-7	-15
1	E	-87	-4.00E-03	0.5983	-6.82E-03	-1	-23
1	F	-96	-5.40E-03	0.4182	-6.24E-03	0	-26
1	G	-100	-1.08E-02	0.3328	-6.16E-03	-3	-28
1	H	98	-5.80E-03	0.188	-2.84E-03	5	14
1	I	101	3.00E-04	0.206	-3.15E-03	5	26
2	B	110	5.40E-03	0.131	-2.76E-03	0	28
2	C	120	1.08E-02	0.1743	-2.59E-03	0	34
2	D	-117	5.40E-03	0.121	-2.45E-03	-2	-31
2	E	-124	-4.00E-03	0.844	-3.11E-03	0	-35
2	F	-126	-5.40E-03	0.0587	-2.71E-03	0	-45
2	G	-135	-1.08E-02	0.151	-3.31E-03	0	-46
2	H	129	-5.80E-03	0.0087	-2.75E-03	0	30
2	I	131	3.00E-04	0.0037	-2.11E-03	-1	43
3	B	138	5.40E-03	-0.046	-2.80E-03	2	47
3	C	150	1.08E-02	-0.042	-2.20E-03	0	51
3	D	-140	5.40E-03	-0.067	-1.19E-03	-10	-42
3	E	-150	-4.00E-03	-0.115	-2.06E-03	-10	-39
3	F	-157	-5.40E-03	-0.064	-2.90E-03	-7	-57
3	G	-161	-1.08E-02	-0.064	-2.73E-03	-7	-62
3	H	149	-5.80E-03	-0.163	-2.44E-03	-14	32
3	I	164	3.00E-04	-0.126	-2.69E-03	-12	53

Table B.6: 316 Stainless Steel, Path II, 610-04.

Cycle	Point	σ (MPa)	ε (m/m)	τ (MPa)	γ (m/m)	a	d	α11	α12
1	A	0	0	0	0	0.9918	0	-5	2
1	B	101	0.0106	46	0.0076	0.7812	-5.17E-04	22	11
1	C	-175	-0.0106	-9	0.0076	0.2841	-4.31E-02	-51	-5
1	D	175	0.0106	-85	-0.0076	-0.0027	-1.73E-04	35	-34
1	E	-271	-0.0106	-3	-0.0076	-0.0841	-2.53E-03	-104	0
1	F	212	0.0003	118	0.0002	-0.172	-1.00E-03	63	39
2	B	237	0.0106	121	0.0076	-0.174	-1.25E-03	77	47
2	C	-350	-0.0106	17	0.0076	-0.267	-2.32E-03	-113	0
2	D	270	0.0106	-147	-0.0076	-0.164	-5.39E-02	114	-81
2	E	-370	-0.0106	-11	-0.0076	-0.23	-7.01E-03	-168	0
2	F	262	0.0003	158	0.0002	-0.159	-1.10E-02	127	90
3	B	284	0.0106	146	0.0076	-0.12	-1.04E-03	114	100
3	C	-396	-0.0106	17	0.0076	-0.214	-9.08E-03	-160	0
3	D	290	0.0106	-160	-0.0076	-0.256	-2.20E-03	111	-73
3	E	-407	-0.0106	-25	-0.0076	-0.336	-1.83E-03	-120	0
3	F	264	0.0003	169	0.0002	-0.246	-1.41E-03	104	89

Table B.7: 316 Stainless Steel, Path III, 610-05.

Cycle	Point	σ (MPa)	ε (m/m)	a	d	α11	α12
1	A	0	0	1.12	0	-146	6
1	C	796	0.015	0.709	-1.33E-04	221	0
1	E	-795	-0.0002	0.666	-6.60E-03	-255	25
1	G	-871	-0.015	0.533	-7.00E-03	-380	-25
1	I	760	0.002	0.269	-1.28E-03	110	0
2	C	833	0.015	0.3368	-1.56E-03	144	0
2	E	-800	-0.0002	0.152	-2.70E-01	-350	0
2	G	-880	-0.015	0.176	-1.56E-01	-376	15
2	I	756	0.002	0.25	-3.12E-04	135	0

Table B.8: Inconel 718, Path I, IN-16.

Cycle	Point	τ (MPa)	γ (m/m)	a	d	α11	α12
1	A	0	0	0.8914	0	-145	0
1	C	535	1.06E-02	0.4399	-1.59E-03	-145	160
1	E	-470	-1.70E-03	0.427	-1.60E-03	-145	-100
1	G	-529	-1.06E-02				
1	I	474	1.70E-03	0.369	-5.55E-03	-145	110
2	C	535	1.06E-02	0.2494	-3.60E-03	-145	140
2	E	-455	-1.70E-03	0.303	-1.59E-03	-145	-63
2	G	-527	-1.06E-02	0.249	-2.30E-03	-145	-110
2	I	466	1.70E-03	0.302	-3.08E-03	-145	80

Table B.9: Inconel 718, Path II, IN-23.

Cycle	Point	σ (MPa)	ε (m/m)	τ (MPa)	γ (m/m)	a	d	α11	α12
1	A	0	0	0	0	0.4032	0	-160	0
1	B	760	0.0106	385	0.0077	0.138	-2.22E-03	144	85
1	C	-1050	-0.0106	127	0.0077	0.2326	-0.99	-418	80
1	D	736	0.0106	-470	-0.0077	0.0959	-1.45E-03	-165	-180

Table B.10: Inconel 718, Path III, IN-27.

Cycle	Point	σ (MPa)	ε (m/m)	τ (MPa)	γ (m/m)	a	d	α11	α12
1	A	0	0	0	0	0.999	0	-160	0
1	C	740	0.02	245	0.015	0.1732	-4.19E-03	100	38
1	D	-585	0.0058	-400	0	0.1239	-2.07E-03	-160	-129
1	E	-857	-0.002	-128	0	0.186	-8.49E-03	-260	10

Table B.11: Inconel 718, Path IV, IN-11.

1. AGENCY USE ONLY (*Leave blank*)	2. REPORT DATE October 2001	3. REPORT TYPE AND DATES COVERED Final Contractor Report

4. TITLE AND SUBTITLE

Behavior of Three Metallic Alloys Under Combined Axial-Shear Stress at 650 °C

5. FUNDING NUMBERS

WU–708–31–13–00
NCC3–597

6. AUTHOR(S)

Jason F. Colaiuta

7. PERFORMING ORGANIZATION NAME(S) AND ADDRESS(ES)

Pennsylvania State University
University Park, Pennsylvania 16802–1009

8. PERFORMING ORGANIZATION REPORT NUMBER

E–13020

9. SPONSORING/MONITORING AGENCY NAME(S) AND ADDRESS(ES)

National Aeronautics and Space Administration
Washington, DC 20546–0001

10. SPONSORING/MONITORING AGENCY REPORT NUMBER

NASA CR—2001-211162

11. SUPPLEMENTARY NOTES

This report was submitted as a dissertation in partial fulfillment of the requirements for the degree of Master of Science to the Pennsylvania State University, University Park, Pennsylvania, August 2001. Project Manager, Bradley Lerch, Structures and Acoustics Division, NASA Glenn Research Center, organization code 5920, 216–433–5522.

12a. DISTRIBUTION/AVAILABILITY STATEMENT

Unclassified - Unlimited
Subject Categories: 26 and 39   Distribution: Nonstandard

Available electronically at http://gltrs.grc.nasa.gov/GLTRS

This publication is available from the NASA Center for AeroSpace Information, 301–621–0390.

12b. DISTRIBUTION CODE

13. ABSTRACT *(Maximum 200 words)*

Three materials, Inconel 718, Haynes 188, and 316 stainless steel, were tested under an axial-torsional stress state at 650 °C. The objective of this study was to quantify the evolution of the material while in the viscoplastic domain. Initial and subsequent yield surfaces were experimentally determined to quantify hardening. Subsequent yield surfaces (yield surfaces taken after a preload) had a well-defined front side, in the prestrain direction, but a poorly defined back side, opposite the prestrain direction. Subsequent yield surfaces exhibited isotropic hardening by expansion of the yield surface, kinematic hardening by translation of the yield surface, and distortional hardening by flattening of the yield surface in the direction opposite to the last prestrain. An existing yield function capable of representing isotropic, kinematic, and distortional hardening was used to fit each yield surface. Four variables are used to describe each surface. These variables evolve as the material state changes and have been regressed to the yield surface data.

14. SUBJECT TERMS

Inconel 718; Haynes 188; Stainless steel; Yield surfaces;
Multiaxial stress; Inelasticity; Viscoplasticity; Strength differential

15. NUMBER OF PAGES
161

16. PRICE CODE

17. SECURITY CLASSIFICATION OF REPORT Unclassified	18. SECURITY CLASSIFICATION OF THIS PAGE Unclassified	19. SECURITY CLASSIFICATION OF ABSTRACT Unclassified	20. LIMITATION OF ABSTRACT